Dissertation

zur Erlangung des Grades

Doctor rerum naturalium

(Dr. rer. nat.)

Vorgelegt dem Bereich Mathematik und Naturwissenschaften der
Technischen Universität Dresden

Spectroscopic Properties of Self-Assembled Plasmonic and Semiconductive Nanocrystals for Nanophotonic Applications

Fabian Rainer Goßler

geboren am 11. August 1990 in Münchberg

Eingereicht am 9. Juni 2020

Verteidigt am 21. September 2020

betreut von

Dr. Tobias König

DON’T PANIC

Chapter 1

Abstract

The next generation of optoelectronic applications like stimuli-responsive sensors, functional displays or nanophotonic circuits demands a basic understanding of light-matter interactions on the nanoscale. Top-down fabrication has been employed in the past to demonstrate coherent energy transfer in functional nanostructures, yet these fabrication methods are problematic due to their limited scalability and high costs as well as the high optical losses. This work adapted physical principles like radiation properties of metallic nanoantennas and Bragg diffraction in periodic nanostructures and realized these concepts using bottom-up self-assembly methods based on colloidal chemistry. With this approach, single plasmonic nanoparticles and semiconductor quantum emitters were co-assembled into complex structures. This work took the colloidal concept from plasmonics and introduced quantum dots in order to characterize the radiative and non-radiative decay processes as well as the arising light-matter interactions. Due to electromagnetic coupling between the components, hybridized modes were detected instead of the single particle resonances observed in the isolated case. It was furthermore shown that these colloidal building blocks can be assembled into functional optical grids on a large scale using template-assisted self-assembly. Thus, this work established spectroscopic principles for self-assembled colloidal building blocks that can be integrated in parallelized processes in the future.

Kurzfassung

Die nächste Generation von optoelektronischen Anwendungen wie stimuli-responsive Sensoren, funktionelle Displays oder nanophotonische Schaltkreise erfordert grundlegendes Verständnis von Licht-Materie Wechselwirkungen auf der Nanometerskala. Top-down Herstellungsmethoden wurden bisher für konzeptionelle Nachweise von kohärentem Energietransfer in funktionellen Nanostrukturen eingesetzt, wobei diese Herstellungsverfahren wegen ihrer limitierten Herstellungsfläche, hohen Kosten und hohen Verlusten an ihre Grenzen stoßen. Diese Arbeit greift physikalische Prinzipien wie die Abstrahlungseigenschaften von metallischen Nanoantennen und Bragg Beugung an periodischen Nanostrukturen auf und setzt diese Prinzipien mit Bottom-up Selbstanordungsmethoden aus der Kolloidchemie neu um. Hierfür wurden einzelne plasmonische Nanopartikel sowie halbleitende Quantenpunktemitter gezielt in komplexe Strukturen angeordnet. Diese Arbeit knüpfte an dem kolloidalen Konzept aus der Plasmonik an und fügte zusätzlich Quantenpunktemitter in ein plasmonisches System ein um die strahlenden und nicht-strahlenden Zerfälle sowie die auftretenden Licht-Materie Wechselwirkungen zu charakterisieren. Durch elektromagnetisches Koppeln zwischen den einzelnen Komponenten konnten, anders als Einzelpartikelresonanzen im isolierten Fall, hybridisierte Moden beobachtet werden. Weiterhin wurde gezeigt, dass diese kolloidalen Bausteine mittels Templat-gestützter Selbstanordnung großflächig in funktionale Gitterstrukturen angeordnet werden können. Somit wurden in dieser Arbeit spektroskopische Grundlagen für selbstangeordnete kolloidale Bausteine erarbeitet, die in zukünftigen parallelisierten Prozessabläufen integriert werden können.

Contents

List of Abbreviations

AFM	atomic force microscopy
AuNS	gold nanosphere
CTAC	cetyltrimethylammonium chloride
EELS	electron energy loss spectroscopy
EF	enhancement factor
FDTD	finite difference time domain
FLIM	fluorescence lifetime imaging
FWHM	full width half maximum
LIL	laser interference lithography
LSPR	localized surface plasmon resonance
MUTAB	(11-mercaptoundecyl)-N,N,N-trimethylammonium bromide
NPoD	nanoparticle-on-dielectric
NPoM	nanoparticle-on-mirror
PAH	poly(allylamine hydrochloride)
PL	photoluminescence
PSS	poly(styrene sulfonate)
QD	quantum dot
QE	quantum efficiency
RMS	rout mean square
SAM	self-assembled monolayer
SEM	scanning electron microscopy
SPR	surface plasmon resonance
TASA	template assisted self assembly
TCSPC	time-correlated single photon counting
TEM	transmission electron microscopy

Chapter 2

Introduction

Acoustic waves can propagate along curved surfaces in form of whispering gallery modes (WGMs), in which the energy inherent to the waves is sustained much longer as compared to propagation in free space. For example, this can be observed in an ancient Chinese temple near Peking, where an uttered whisper returns to the respective person after some time due to the propagation of sound along the curved temple walls.[1] The same effect is also present for light waves that can propagate along the curved surface of sufficiently small spheres.[2] Although this mode propagation features low energetic losses and is successfully employed for optical devices like lasing or biosensing[3], it is limited by the diffraction limit of optical waves and usually demand low temperatures. In analogy to WGMs, plasmon resonances of noble metal nanostructures can confine electromagnetic modes into volumes much smaller than the wavelength of the incident light and therefore surpass the diffraction limit at room temperature.[4]

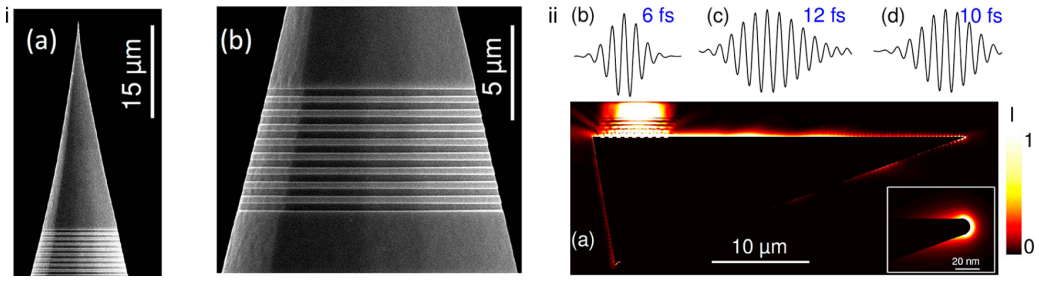

Figure 2.1: (i) Scanning electron microscopy images of a single crystalline gold tip with focused ion beam milled grating coupler. (ii) Electromagnetic simulation of the laser pulse coupled into a propagating plasmon resonance along the gold surface with resulting field enhancement at the tip (a) and time structures of the electric fields of the initial pulse (b), the field induced by the plasmon resonance (c) and the confined field at the tip (d). Reprinted (adapted) with permission from Schmidt et al.[5]. Copyright 2020 American Chemical Society.

Specific design criteria on nano scale regarding material and spatial properties must be met by these structures, which makes their fabrication a demanding task. A common way to manufacture plasmonic systems are top-down methods, where high-energy sources are used to cut the respective structures from the bulk material. As an example, Schmidt et. al employed focused ion beam milling to create a periodic grid on a gold tip in order to couple incident light pulses into a plasmon resonance, which is then guided along the gold surface in analogy to a WGM. This leads to nonlinear optics like second harmonic generation that can be applied for scanning near-field optical microscopy.[5] Figure 2.1i depicts the obtained grating with 800 nm periodicity on a single crystalline gold tip. When a laser pulse (λ_I=870 nm) hits the grating, a plasmon resonance is excited and propagates along the metal surface until the evanescent field gets confined at the tip shown in the electromagnetic simulations in figure 2.1ii.

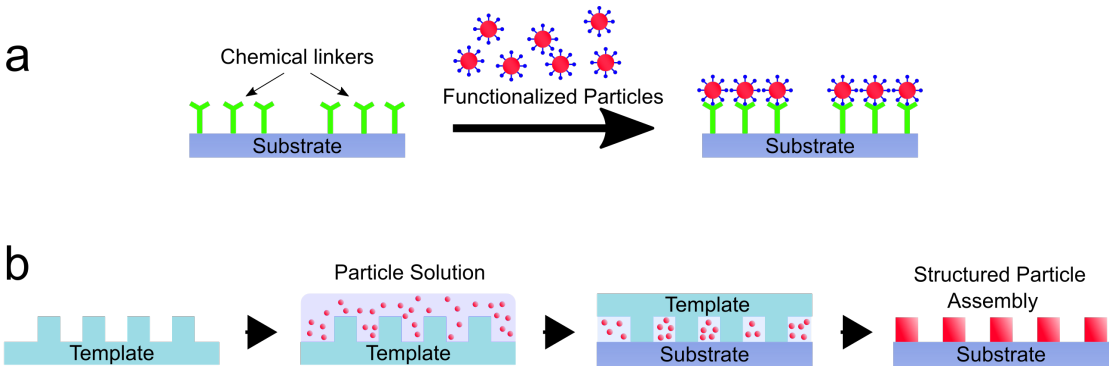

Figure 2.2: Schematic illustration of the two approaches on bottom-up self-assembled colloids. (a) Chemical linkers like thiols or DNA strands on the desired substrate can actively control the adsorption of colloidal particles with suitable ligands through covalent bonds or electrostatic interactions. (b) Template-assisted self-assembly guides a solution of colloidal particles into the respective pattern due to capillary flow of the particle solution in the template. The obtained pattern can be directly transferred to a substrate.

Although the above-mentioned top-down methods offer numerous possibilities towards the fabrication of functional nanostructures, they can be a bottleneck for macroscopic application due to the limitations of lithographic methods like the limited scalability and less control on the chemical composition of the structures .[6] It can therefore be desirable to use bottom-up techniques, where building blocks like single crystalline metal nanoparticles or colloidal quantum dots with high optical quality are arranged to form functional structures in a scalable, cost- and time-efficient way.[7] This is achieved by spontaneous organization of the respective building blocks into

complex structures, which is controlled by the physical and chemical properties of the involved components as well as their environment.[8–10] The assembly of the colloids is usually governed by two different approaches: with surface-chemical functionalities like specifically designed DNA strands[11] or polymeric ligands[12,13] on the one hand and with pre-structured templates to guide the particles into the desired structures using convective assembly on the other hand.[14–16] Latter is of particular interest for scalable optoelectronic materials as is exploits capillary forces to steer the particles into versatile patterns (for example optical gratings) on large scale,[17] while chemically driven assemblies can achieve small feature sizes and low distances between the single building blocks that are not accessible with top-down methods.[6,18] These two basic concepts of bottom-up self-assembly are illustrated in figure 2.2. The present work will show how colloidal approaches can be used to realize functional nanophotonic structures with high optical quality and spatial control on large scale.

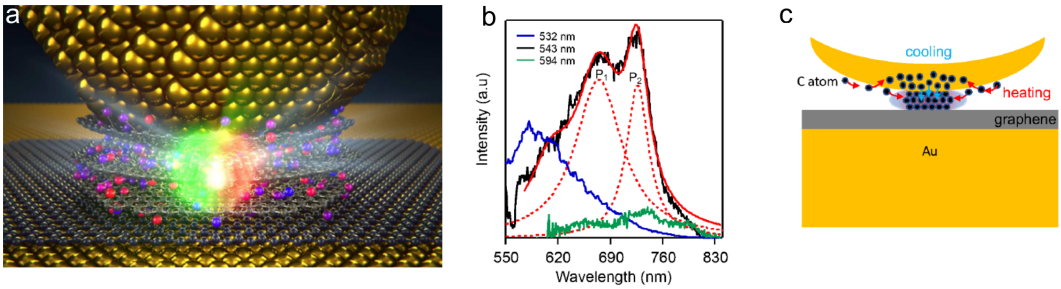

Figure 2.3: (a) Graphic illustration of carbon quantum dot formation in the enhanced field between a plasmonic gold particle and a gold mirror. (b) Emission spectra of the formed carbon quantum dots under different excitation wavelengths. (c) Schematic illustration of the creation of ordered carbon atoms inside the confined electromagnetic field of the plasmonic cavity. Reprinted (adapted) with permission from Katzen et al.[19]. Copyright 2020 American Chemical Society.

One of the methods to assemble functional plasmonic systems using the colloidal approach was recently shown by Katzen et al.. They sandwiched a sub-1 nm graphene layer in between a plasmonic gold sphere and a gold mirror to create a low particle-to-film distance, which leads to strongly enhanced electromagnetic fields that are confined into a very small volume as depicted in figure 2.3. Organic molecules present on the gold surface are carbonized once they are exposed to this induced field and ordered carbon quantum dots are formed by having the graphene layer acting as a template grid. This demonstrates how bottom-up methods for plasmonic structures can give rise to novel materials and applications in optoelectronics and nano technology that are not accessible with top-down fabrication.[19]

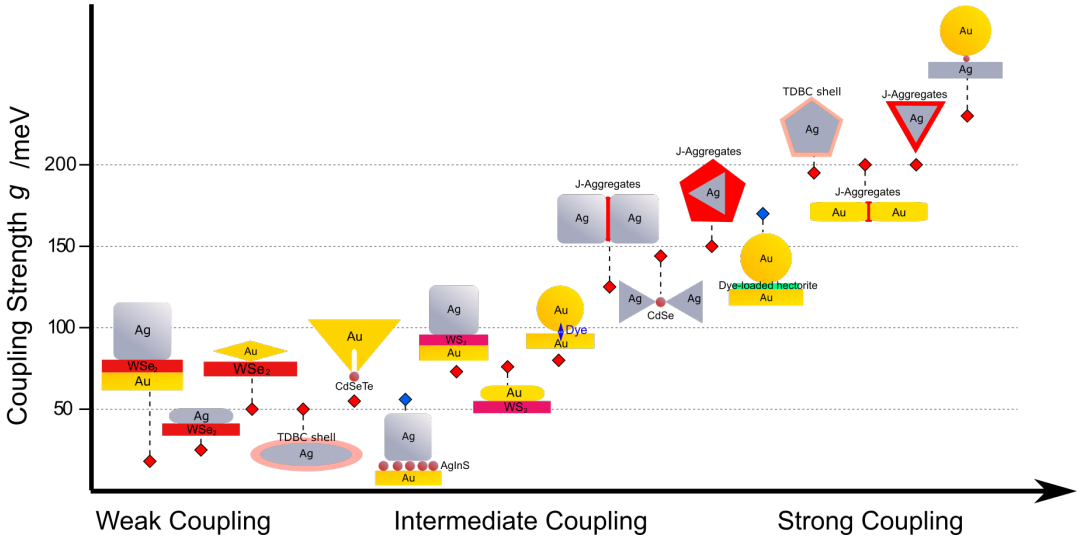

Figure 2.4: Schematic overview of selected plasmon-exciton coupled systems in recent literature regarding the reported coupling strength g from weak to strong coupling interactions (red boxes): A colloidal silver cube-to-gold film cavity with embedded WSe_2 emitter[20], WSe_2 coupled silver rods and gold bi-pyramids, a silver cube-to-gold film cavity[21] and a gold rod coupled to WS_2 emitters[22] show how plasmonic system interact with 2D transition metal dichalcogenides and lead to weak to intermediate coupling. Organic dyes and J-aggregates coupled to a silver rod[23], silver cube and gold disc dimers[23,24], silver nanowires[25], silver prisms[26,27] and gold sphere-to-gold film cavities[28] show a variety of coupling interactions from weak to strong coupling. Semiconductor nanocrysals incorporated in a single crystalline goldflake gap[29], silver bow ties[30] and a gold sphere-to-silver film cavity[31] cover a broad range of coupling strengths. The blue squares correspond to the plasmonic systems studied in this work.

The field enhancement induced by plasmonic nanostructures can strongly interact with photoluminescent materials due to the coupling between the emitter and the electromagnetic field.[32] These coupling interactions can result in a coherent energy transfer between emitter and the plasmonic structure and be employed in applications like optical computing.[33] The coupling between plasmon resonances and emitted photons can furthermore compensate the losses that are inherent to metallic materials.[34] These losses occur as the optical energy of incident photons dissipates in the metal and is furthermore taken out of the coupled system.[35] The coupling strength g is a measure for the level of light-matter interactions in energy units and is a crucial property of functional plasmonic systems. Low coupling strengths are present in the so called weak coupling regime, where energy can be transferred from the emitter to the plasmonic structure in a nonreversible and incoherent way. This is caused

by the losses of the metallic components, which lead to a one-directional flow of energy. Strong coupling is present when the coupling strength exceeds the losses and reversible, coherent energy transfer between the coupled components is possible.[36] The transition from weak to strong coupling is fluent and therefore the term of intermediate coupling was introduced, where optical effects attributed to strong coupling can be detected while the losses still surpass the coupling strength.[31] An overview on a selection of recent plasmonic systems for generation of coupling interactions between emitters and plasmon resonances is displayed in figure 2.4. Controlling optical properties of plasmonic cavities and emitters on nanoscale is challenging regarding the experimental realization and characterization and is crucial for devices like optical computers, displays, bioimaging and sensing.[26,37–39]

The scope of this thesis is to show how metallic and semiconductor colloidal building blocks can be employed to fabricate nanostructures with tailored optical properties on macroscopic scale. The single crystalline composition of the colloids and their availability in aqueous solution make them ideal candidates for scalable, bottom-up self-assembled systems that give rise to strong light-matter interactions between the used components. It is of interest for basic research as well as for applications like coherent energy transfer and photon emission to further understand and quantify these light-matter interactions and to generate them on cm^2 scale. The assembly methods require high control of physical-chemical processes and the quantification of the emerging phenomena demands complementary optical and surface characterization methods combined with electromagnetic simulations to access all the relevant parameters. The first topic that is studied regarding its potential for coherent energy transfer between metallic nanostructures and emitters are plasmonic colloid-to-film coupled cavities with embedded emitters due to their cost-efficient manufacturing on large scale and their tunable optical properties. In chapter 4.1, electromagnetic simulations are employed to comprehend how the properties of the colloid and the particle-to-film distance can result in different cavity resonances in the optical wavelength region. The light-matter interactions in this system are simulated by applying a resonant dipole source in the enhanced electromagnetic field of the particle-to-film coupled cavity, which leads to large changes in the radiative decay rates and the quantum efficiency of the emitter. It is further shown how crucial the position of the emitter

in relation to the electromagnetic field is by simulating different dipole positions and orientations.[FG1] Chapter 4.2 and 4.3 put these theoretical findings into practice by assembling different types of particle-to-film coupled cavities made from a variety of colloidal building blocks. Complementary characterization methods like atomic force microscopy (AFM), scanning electron microscopy (SEM), dark-field spectroscopy and time resolved fluorescence measurements are employed to thoroughly investigate the fingerprints of electromagnetic coupling between the metallic cavities and photoluminescence (PL) of emitters. Mixed light-matter states and enhanced fluorescence with decreased lifetimes are detected quantitatively on large scale and allow statistical evaluations of the coupling processes.[FG3]

The second way to exploit the scalable assembly of colloids is to assemble them in tunable, periodic macrostructures. To achieve this, a laser interference lithography (LIL) setup is built to fabricate optical nano gratings, which are then molded into elastic polymers.[FG4] In analogy to the assembly of plasmonic particles, the resulting templates are used to confine a solution of colloidal semiconductor emitters by controlling its capillary flow with the elastic stamp. This assembly strategy leads to uniform gratings composed entirely by colloidal emitters. The integrity of the structures is confirmed using AFM, SEM and dark-field imaging. Angle dependent UV-vis measurements reveal a macroscopic Rayleigh anomaly due to intense diffraction in the grating and the photoluminescence properties are characterized with time-resolved fluorescence microscopy.[FG5]

This work lead to new strategies to realize functional, colloidal nanostructures on large scale and furthermore correlated complementary spectroscopic and microscopic characterization methods together with electromagnetic simulations for systematic studies on the resulting systems. This can improve the generation of tailored light-matter interactions in terms of coherent energy transfer and future developments in nanophotonic devices.

Chapter

3 Theory and Methods

3.1 Localized Surface Plasmon Resonances

The scientific origin of research on plasmonics dates back to 1856, when Michael Faraday accidentally created a solution of colloidal gold and was intrigued by its intense, red color that can be seen in figure 3.1. While similar optical phenomena in gold containing solutions had previously been linked with chemical compounds formed by the gold ions[40], Faraday found that the color was created by light that's scattered on colloidal metal particles.[41]

Figure 3.1: Faraday's original colloidal gold solution from the 1850s kept its characteristic color to this day. Photo taken with friendly permission from Paul Wilkinson Photography.

Half a century later, a theoretical framework on the mathematical description of interactions between light and spherical particles was introduced by Gustav Mie which is valid to this very day.[42] Although scientists like Richard Adolf Zsigmondy were able to investigate colloidal metal particles on the nano scope in the early 20th century using the ultramicroscope (a type of Dark-field microscope)[43], it needed further

progress in the field of colloidal chemistry to make plasmonic colloids appealing for optoelectronic devices and basic research ranging from potential cancer treatments[44] to optical computing.[33]

The intense optical response of plasmonic colloids under incident light is caused by Localized Surface Plasmon Resonances (LSPRs), which are oscillations of the particle surface electrons in presence of an external electro-magnetic field, i.e. light.[45] This process is depicted in figure 3.2.

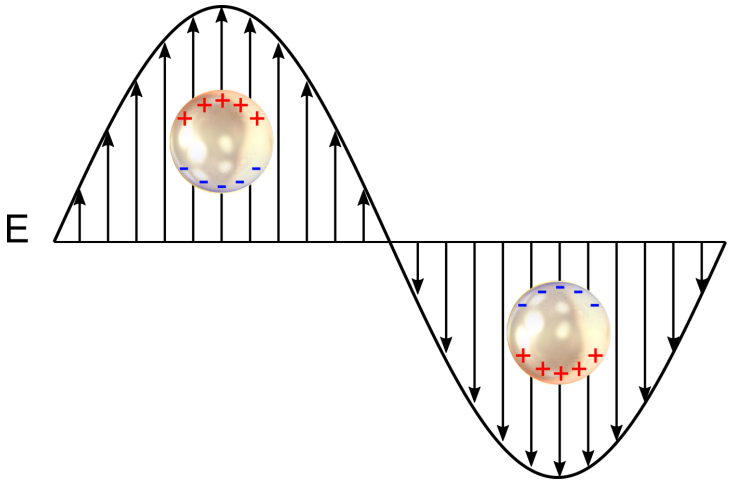

Figure 3.2: Illustration of a gold nanosphere in an external field, which causes a collective oscillation of the surface electrons.

It is a suitable approximation to understand the LSPR as an induced dipole moment since charge carriers (i.e. electrons) are set into motion and therefore lead to unbalances in the charge distribution. The dipole moment p is defined as

$$p = Qd \tag{3.1}$$

where Q is the absolute value of the charge and d the distance between the separated charge carriers.[46] The polarizability α is a measure for the agility of the charge carriers in the nanoparticle and strongly depends on the dielectric function of the metal. The simplest geometry for such a particle is a sphere, which is why the polarization of a plasmonic colloid is shown for that example:

$$\alpha = 3V\epsilon\frac{l(\epsilon - \epsilon_0)}{l\epsilon + (l+1)\epsilon_0} \tag{3.2}$$

where V is the volume of the sphere, ϵ the dielectric function of the metal, ϵ_0 the dielectric function of the surrounding medium and l the orbital momentum number. It is important to take the polarizability into account since its dipolar ($l = 1$) contribution is directly affecting the far-field cross section of a plasmonic nanoparticle.[47] The far-field cross section is basically the optical response that can be experimentally obtained in form of optical extinction σ_{ext}

$$\sigma_{ext} = \frac{2\pi}{\lambda\sqrt{\epsilon_d}}\Im\{\alpha\} \tag{3.3}$$

and also the scattering cross section σ_{sct}, which can be derived from the wavelength-dependent Rayleigh scattering:[48]

$$\sigma_{sct} = \frac{8\pi^3}{3\lambda^4}|\alpha|^2 \tag{3.4}$$

It can further be derived from equation 3.2 that the polarizability reaches its maximum if the term $\epsilon + 2\epsilon_0$ (for a dipolar mode $l = 1$) approaches 0 and therefore fulfills the resonance condition. If this is the case, the excited LSPR leads to intense scattering of incident light that can be detected using dark-field microscopy and singe particle scattering spectroscopy.

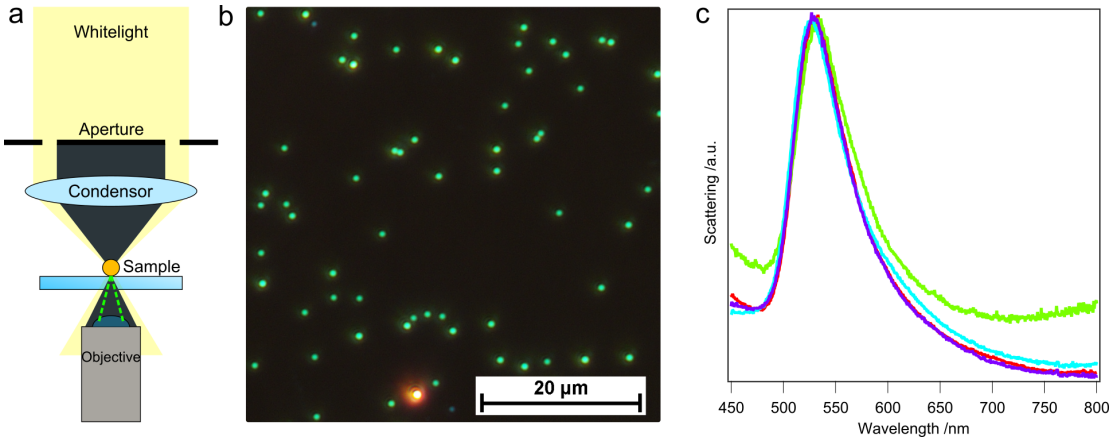

Figure 3.3: Dark-field detection of plasmonic particles. (a) Schematic illustration of an inverse dark-field microscope. (b) Dark-field image of spherical gold colloids. (c) Dark-field scattering spectra of spherical gold colloids.

A schematic dark-field setup is illustrated in figure 3.3: Light shines through an aperture that creates a cone of light, which is focused onto the sample. The light cone

hits the specimen and gets scattered into the dark-field inside the light cone (dashed green lines) and can be detected by an objective. Due to the strong scattering induced by LSPRs, dark-field microscopy and spectroscopy are crucial for characterizing plasmonic phenomena.

To theoretically approach the resonance condition of plasmonic particles, one can either calculate the dielectric constant for the respective material from theoretical models[49,50] or use measured dielectric functions.[51] Together with the theoretical description of LSPRs, the frequency dependent optical response of a gold nanosphere (AuNS) can be calculated using a commercially available finite difference time domain (FDTD) 3D electromagnetic simulator.[52] An exemplary simulation is depicted in figure 3.5a. A pronounced peak around 520 nm is present for the scattering signal σ_{sct} and the absorption σ_{abs}, which result in σ_{ext}. The pronounced resonance peak around 520 nm compares very well to the experimental values obtained by dark-field spectroscopy.

Another phenomena that arises from LSPRs besides strong scattering and absorption of incident light are enhanced electromagnetic fields that are induced by the oscillating electrons in the plasmonic colloid.[54] If a plasmonic particle is brought in close vicinity to another object, electromagnetic coupling of the LSPR with the respective system occurs.[55,56] This can be illustrated exemplary by placing a cubic silver particle onto a dielectric substrate.[53] The coupling between LSPR and the dielectric material leads to a hybridization of the excitable electronic states into a dipolar and a quadrupolar mode that interfere with each other and lead to so-called fano resonances in the scattering spectrum (figure 3.4i). If a plasmonic gold surface instead of a dielectric material is coupled to the particle, additional mirror charges can be induced due to coupling between the LSPR of the particle and the surface plasmon resonance (SPR) of the gold layer. This coupling leads to a field confinement in the region between particle and surface (figure 3.4ii).

Additional plasmonic coupling takes place if two metal nanoparticles are brought into close distance, which results in their LSPRs interacting with each other. The dipolar modes in the single particles experience a hybridization in which the directional independence of the plasmonic modes is repealed and more complex modal structures at different energy levels emerge.[47] Figure 3.5 depicts the additional hybridized mode

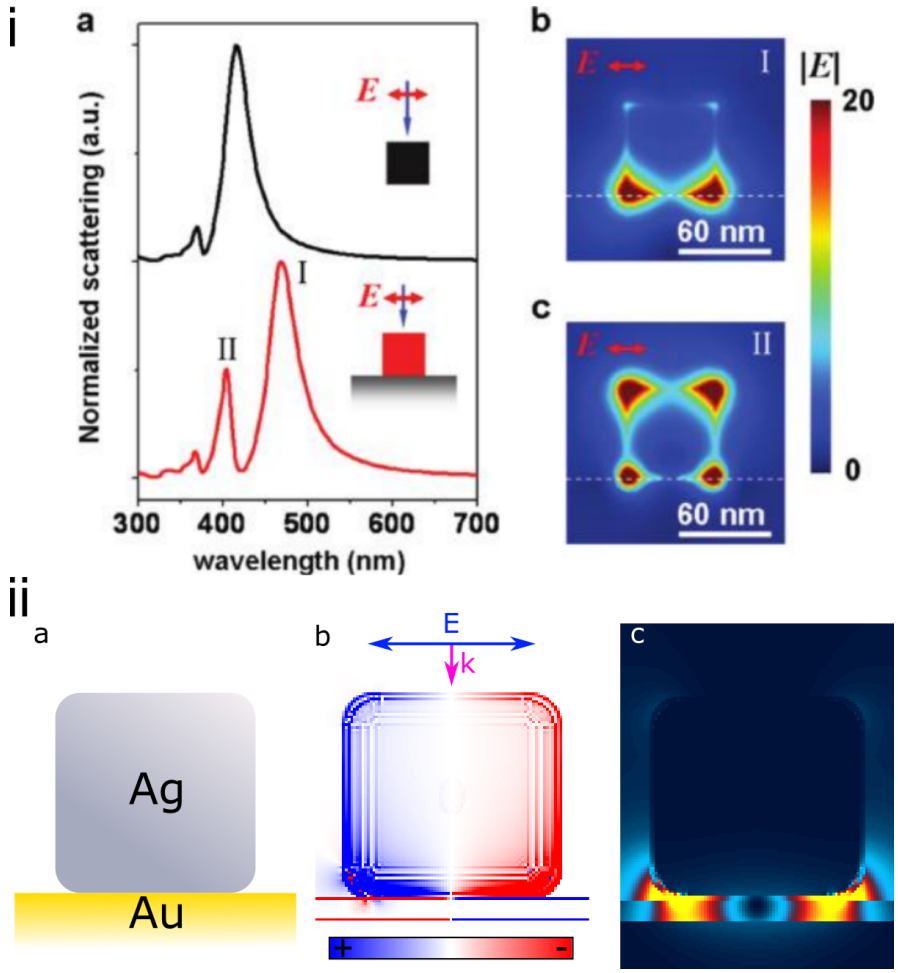

Figure 3.4: Plasmonic hybridization of a cubic silver colloid. (i) Illustration of the mode hybridization of a silver cube on a dielectric substrate which leads to a dipolar bonding (b) and a quadrupolar antibonding (c) mode. Reprinted (adapted) with permission from Zhang et al.[53]. Copyright 2020 American Chemical Society. (ii) Schematic illustration of a silver cube on a plasmonic gold surface (a) with its corresponding simulated surface charge (b) and electric field enhancement (c).

resonances, mode structures and the enhanced electric fields that are formed when the LSPRs of two gold spheres interact with each other.

The tunable optoelectronic properties of coupled plasmonic systems as well as their enhanced electromagnetic fields in small modal volumes are appealing features for investigating fundamental light-matter interactions and applications like plasmonic rulers, where the coupling-induced changes in the optical responses of plasmonic particles can be used to monitor changes in distance on nanoscale.[57] The present thesis will mainly focus on the creation and quantification of the light-matter interactions arising induced by plasmon resonances.

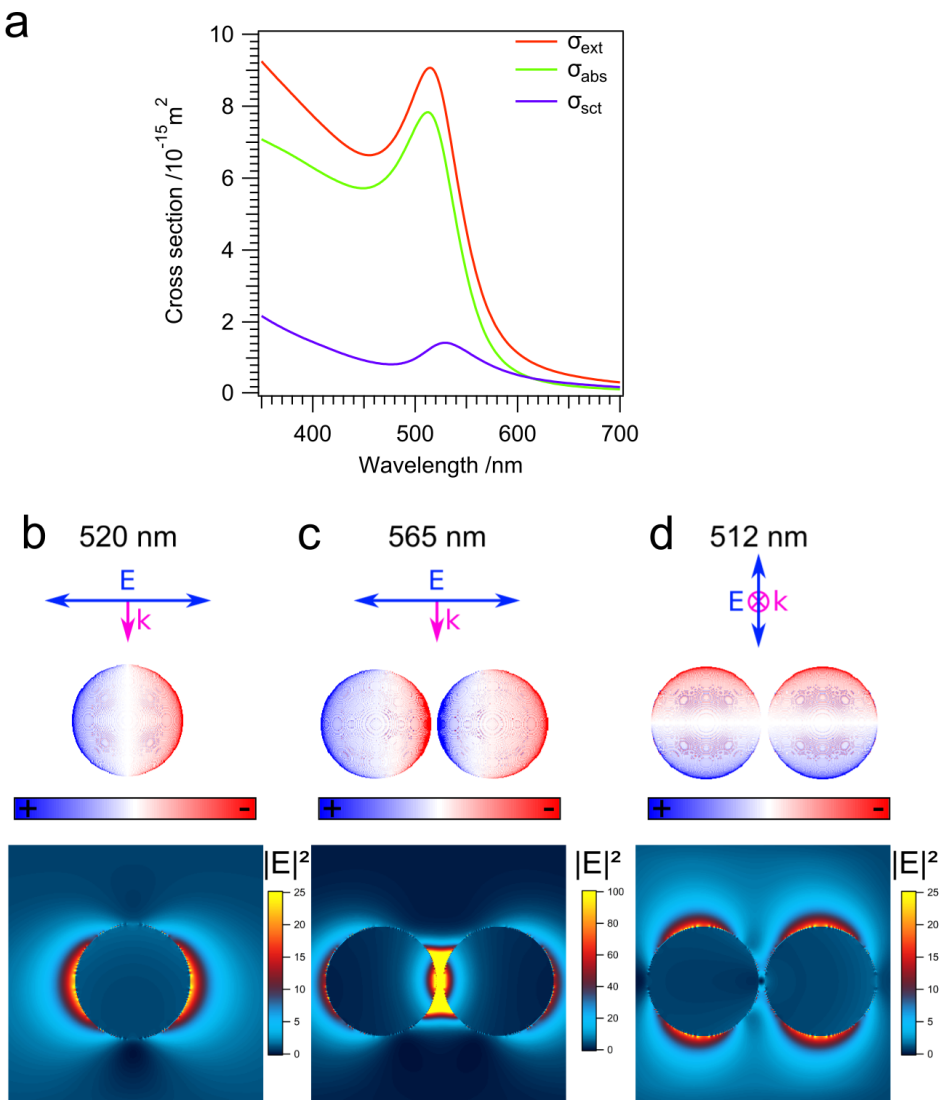

Figure 3.5: FDTD simulations of electromagnetic mode structures for a single gold sphere. (a) Simulated optical properties of a colloidal gold sphere. Simulated surface charges and field enhancements show a degenerated dipolar mode which is independent of the spatial axis at 520 nm for a single sphere (b) and hybridized modes of a dimer (c+d).

3.2 Photoluminescent Semiconductor Nanocrystals

The emission of light from any substance, being it a solution, a solid or a gas, is referred to as photoluminescence (PL) and was first discovered in 1845 when Sir John F.W. Herschel noted a vivid blue shine originating from a otherwise colourless solution of tonic water.[58,59] The intense colours inhibited by such fluorescent specimens were soon employed as a tool for various research tasks, for example to retrace an subterranean connection between the Rhine and the Danube in 1877.[60] It yet took until the mid of the 20th century to move studies on fluorescence into a more quantitative and popular dimension when the first spectrofluorometers were developed.[61] The basic principle behind fluorescence, being it emission from organic dye molecules or solid state emitters, is an electronic excitation from the ground state into higher states following an energetic stimulus, which usually is the absorption of an incident photon. While several excited states (S_1 and S_2) with additional vibrational states can be occupied by an excited electron, so called internal conversion causes the state to relax towards the lowest vibrational state of S_1. This process, known as Kasha's rule[62], takes place in the order of 10^{-12} s and is therefore already concluded before the excited state can decay back to the ground state S_0.[63] The rate, in which these excited states can relax back to the ground states, depends on the spin of the electron. When latter is a spin paired singlet electron, it can quickly decay back to the lowest vibrational state, which is called fluorescence. When the electron occupies a triplet state, the relaxation to S_0 is spin forbidden and takes place with a decreased rate in form of phosphorescence. In both cases, the energy difference between the excited and the relaxed electronic state is released upon de-excitation of the electron either through radiative decay by emitting a photon of the respective energy or nonradiative decay in form of vibration with the respective radiative decay rate k_r and nonradiative decay rate k_{nr}. These decay processes can be illustrated in a so-called Jablonski diagram, which is shown in figure 3.6.

To quantify PL, the fluorescence lifetime τ is taken into account. It is given by

$$\tau = \frac{1}{k_r + k_{nr}} \tag{3.5}$$

and can be experimentally detected with time-correlated single photon counting (TC-

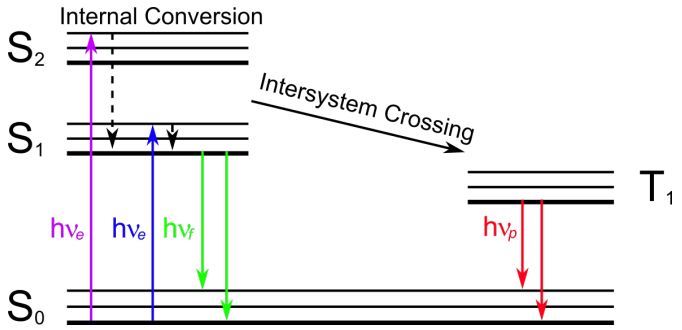

Figure 3.6: Illustration of electronic processes taking place during PL in form of a Jablonski diagram: $h\nu_e$ shows the excitation caused by an incident photon which causes a transition from the electronic groundstate S_0 to the excited states S_1 and S_2 or their respective higher vibrational levels. Internal conversion causes the excited states to relax into the lowest vibrational level of S_1. $h\nu_f$ illustrates the de-excitation back to the ground level under fluorescence emission. Alternatively, phosphorescent emission $h\nu_p$ can occur after intersystem crossing of the excited state to the triplet state T_1.

SPC). This method allows statistical evaluation of the PL lifetimes by exciting the respective specimen with a periodic laser pulse sequence with sufficiently low energies that ensures that only one photon can be emitted after a pulse. Single photon detectors then measure the time between each laser pulse and single photon detection and the resulting histogram of pulse-photon detection time can be fitted with exponential functions, which give the fluorescence lifetime (figure 3.7).[58]

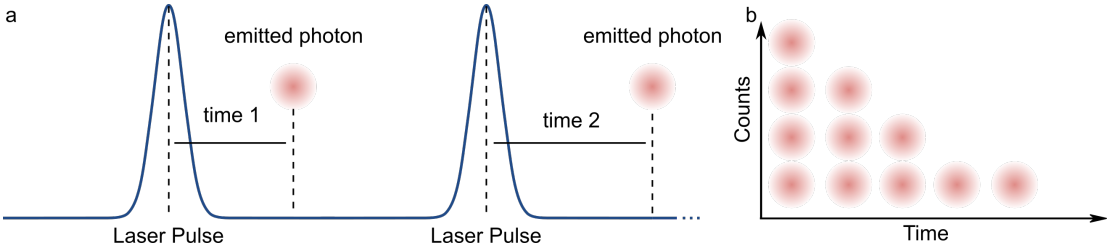

Figure 3.7: Time-correlated single photon counting (TCSPC). (a) Schematic illustration of the laser pulse excitation and single photon detection sequence. (b) Histogram of lifetimes for each detected photon.

The quality of a photoluminescent material is furthermore given by the quantum efficiency QE, which expresses the ratio between absorbed and emitted energy.

$$QE = \frac{k_r}{k_r + k_{nr}} \tag{3.6}$$

While fluorescence in organic molecules has been known for almost 2 centuries now, a rather young class of emitters are colloidal crystalline semiconductor nanoparticles (also called quantum dots) that were first reported in 1982 by Arnim Henglein[64]

and quickly gained great interest due to further pioneering research of Louis Brus[65], Alexei Ekimov[66] and the Efros brothers[67]. Since the particles inhibit the crystal unit cell of the bulk semiconductor while featuring diameters below 10 nm, the electronic and optic properties deviate fundamentally from those of the macroscopic material.[68] Due to quantum confinement of the electronic states that takes place if the size of a particle approaches the atomic scale, the size and shape of semiconductor nanocrystals directly affect their respective fluorescence and thus are highly tunable over the optical spectrum.[69] To understand this in detail, one has to consider that each object, no matter if microscopic or macroscopic, has a certain wave character which can be expressed through the De-Broglie wavelength λ:[70,71]

$$\lambda = \frac{h}{p} \tag{3.7}$$

where h is the Planck constant and p the impulse of the particle. Latter can be described using

$$p = \sqrt{2m\,E} \tag{3.8}$$

where m is the mass and E the energy of the object. Since fluorescence is caused by electronic processes, the De-Broglie wavelength for a single electron at 300 K is calculated:

$$\lambda = \frac{h}{\sqrt{2m_e * k_B T}} \tag{3.9}$$

where m_e is the electron mass and k_B is the Boltzmann constant. This gives

$$\lambda = \frac{6.63 \cdot 10^{-34}\,\mathrm{J\,s}}{\sqrt{2 \cdot 9.11{\times}10^{-25}\,\mathrm{kg} \cdot 1.381{\times}10^{-23}\,\mathrm{J\,K^{-1}} \cdot 300\,\mathrm{K}}} = 7.63 \cdot 10^{-9}\,\mathrm{m} \equiv 7.6\,\mathrm{nm} \tag{3.10}$$

as wavelength of a single electron. Considering that the mentioned quantum dot particles obtain dimensions in the same order of magnitude as λ, latter is limited since it can only propagate inside the particle. To further show how this affects the electronic states (i.e. the bandgap between valence band and conductive band energy levels) and therefore the emission energy, the excited electron in a QD can be interpreted with the established particle in a box model from quantum mechanics. Here the wave function

is trapped inside a confined space with infinite high potential walls at the edges:[72]

$$E_n = \frac{h^2\, n^2}{8 m_e\, L^2} \tag{3.11}$$

where E_n are the quantized energy levels, n is the quantum number and L is the length of the potential box. This model is the foundation on which Louis E. Brus based his now established model to calculate the concrete energy for the lowest excited state energies of semiconductor quantum dot particles in terms of the particle radius:[73]

$$E^* = E_{gap} + E_{kin} - E_c \tag{3.12}$$

This general form gives the transition energy E^* as the sum of the band gap energy E_{gap}, the electric kinetic energy E_{kin} and the electric potential energy E_c. This can now be analytically solved by introducing the material constants of the respective semiconductor to the term:

$$E^* = E_{gap} + \frac{h^2}{8\, R^2}\left(\frac{1}{m_e^*} + \frac{1}{m_h^*}\right) - \frac{1.8e^2}{4\pi\, \epsilon_{CdTe}\epsilon_0 R} \tag{3.13}$$

where m_e^* is the excited electron mass and m_h^* the excited hole mass while ϵ_{CdTe} and ϵ_0 are the dielectric constants of the quantum dot material and the surrounding medium (here vacuum).

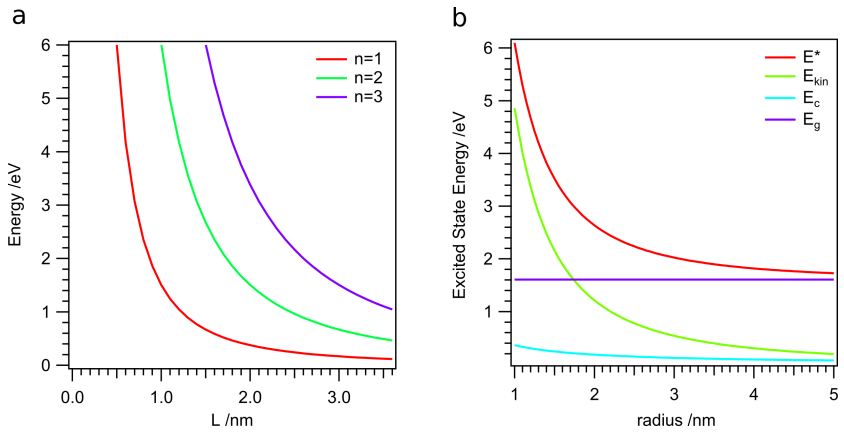

Figure 3.8: Theoretical approximation on electron quantum confinement using the particle in a box model (a) and the analytical Brus model for CdTe QDs (b) which shows the transition energy E* (red line), the kinetic energy E_{kin} (green line), the potential energy E_c (teal line) and the band gap energy E_g (violet line).

These parameters are material constants for the respective semiconductor crystal, so the only variable contributor to changes in the emission energy is the particle radius R. Figure 3.8 shows the size-dependent exciton energies for an exemplary CdTe quantum dot as this material is commonly used in emitters with tunable optical properties.[74] The material parameters are taken from literature.[75] Despite the calculated energies differing from experimental values seen in literature, they present a convenient way to approach the optical properties of quantum dots with basic quantum mechanical models.[76]. Although the photoluminescence properties of semiconductor nanocrystals show great potential for various applications in medical or optoelectronic devices, they suffer from features like incoherent emission and photonic losses in macroscopic QD assemblies. This thesis will introduce ways to enhance the radiative properties of semiconductor nanocrystals with spectroscopic and microscopic methods combined with electromagnetic simulations.

3.3 Coherent Energy Transfer through Plasmon-Exciton Coupling

If a photoluminescent specimen is placed in the enhanced electromagnetic fields induced by plasmon resonances, strong light-matter interactions are induced if the resonance of the emitted photons and the field overlap energetically. This coupling between a plasmonic nanostructure and emitters can enhance the luminescence properties of the latter. Plasmon-enhanced luminescence has already been achieved with a variety of systems, for example anisotropic gold particles in close vicinity to luminescent upconversion particles[77], semiconductor nanocrystals placed on a rough gold surface[78] or quantum dots coupled to a periodic plasmonic array[79]. Furthermore, plasmon resonances can improve the energy transfer between different emitters, for example by enhancing Förster Resonance Energy Transfer (FRET) of different CdTe quantum dots.[80] In the case of plasmon-exciton coupling, both components can be interpreted as dipoles in a coupled oscillator model, where energy can be coherently transferred between the emitter and the plasmonic particle. These plasmon-exciton interactions are usually referred to as weak, intermediate and strong coupling depending on the amount of energetic losses compared to energy transfer.[81] If the latter exceeds the damping of the metal as well the emitting material, one can also observe hybridized modes in the system which is expressed through the so called Rabi splitting.[25] Figure 3.9 shows an energy diagram to illustrate the coherent energy transfer taking place in sufficiently coupled plasmon-exciton systems.[82] The mode hybridiza-

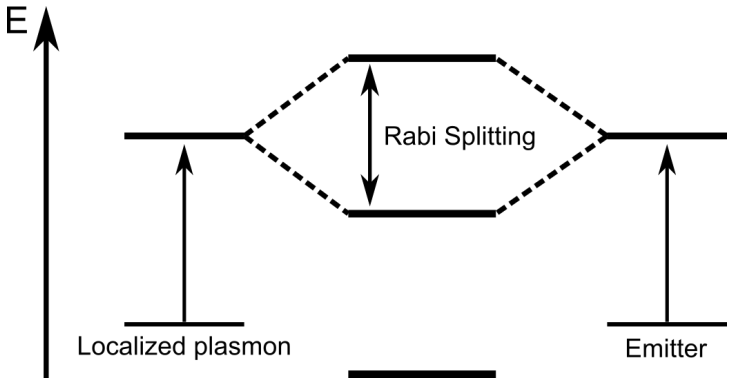

Figure 3.9: Energy scheme of a plasmon resonance coupling with an exciton which results in a hybridization of the excited resonance.

tion directly corresponds to the light-matter interactions taking place in such coupled systems, which is intriguing for in-depth investigations on these processes as the hybridized modes can be measured using scattering spectrocopy (i.e. detection of σ_{sct}, see equation 3.4). The energetic difference between both modes gives the coupling strength g, which will be discussed in more details in the Results and Discussion part. In general, this coupling strength has to surpass the energetic losses to ensure coherent energy transfer and two fully distinguished polariton peaks in the scattering spectrum.[83,84] The modulation of the latter through coupling interactions can be approximated using an analytical coupled oscillator model:[31]

$$\sigma_{sct} \propto \omega^4 \left| \frac{(\omega_{em}^2 - \omega^2 - i\omega\gamma_{em})}{\left(\omega^2 - \omega_{sp}^2 + i\gamma_{sp}\omega\right)(\omega^2 - \omega_{em}^2 + i\gamma_{em}\omega) - \omega^2 g^2} \right|^2 \tag{3.14}$$

where ω_{em} is the emitter resonance frequency, γ_{em} the damping introduced by the emitter, ω_{sp} the surface plasmon frequency and γ_{sp} the losses of the leaky plasmon mode. Equation 3.14 is used to demonstrate different stages of mode hybridization from weak to strong coupling as shown in figure 3.10 by applying different coupling strengths g to the model.

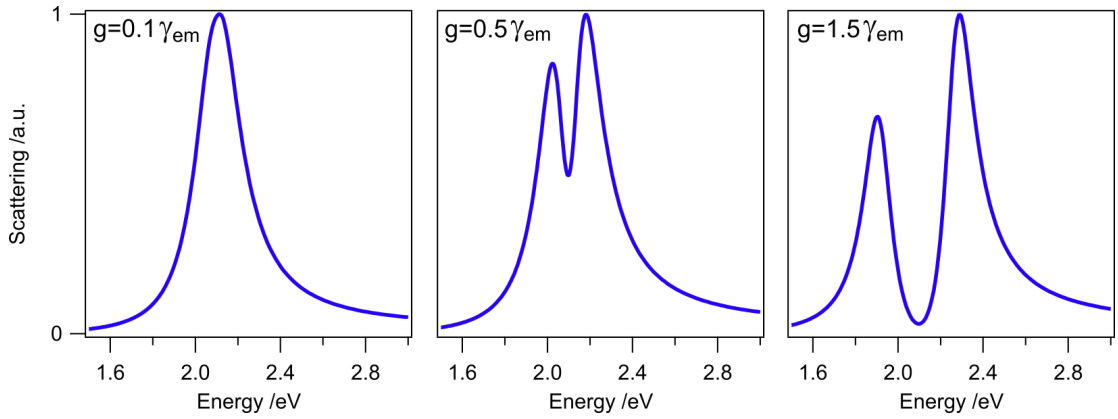

Figure 3.10: Calculated scattering cross sections for a coupled plasmon-exciton oscillator for different coupling strengths g.

The calculated scattering cross sections show typical plasmonic features for a low coupling strength with a single peak, which is to be expected for weak coupling or no coupling at all. A visible dip in the spectrum for a higher g indicates the transition into the intermediate coupling, where energy transfer between surface plasmon and the

exciton takes place but the losses can't be sufficiently compensated. If g starts to overcome the losses introduced by the damping of the coupled oscillators, two separated modes are present in the scattering spectrum, which is in return a strong indicator for coherent plasmon-exciton coupling.[31] The results in this thesis will demonstrate how these light-matter interactions can be generated, quantified and improved for coherent energy transfer and emission with scalable, colloidal approaches and and quantified by using complementary characterization methods.

3.4 Methods

Characterization Methods

Dark-field measurements. Single particle scattering spectroscopy was done with a Nikon Ti-U inverted microscope in transmission mode. The data were recorded using an IsoPlane-160 spectrometer and a PIXIS: 256 CCD camera (Princeton Instruments). Measurements were performed with a dark-field condenser (air, NA 0.8-0.95) and a 60x air objective (CFI S Plan Fluor ELWD, NA 0.7, Nikon, Japan) under illumination by an Energetiq EQ-99 laser driven light source. The measured spectra were corrected by subtracting the dark current at the detector and normalizing against the white light scattering spectrum of a polystyrene particle solution.

Time-resolved fluorescence measurements. Fluorescence lifetime images and time-correlated single photon counting (TCSPC) data were measured with an inverted confocal scanning microscope (MT200, PicoQuant) incorporating a 100x air objective (UPLFLN, NA 0.9, Olympus, Japan). Diode lasers with 405 nm and 506 nm central wavelengths (LDH-405; LDH-510) and 1-5 MHz repetition rates were used for excitation. The signal was guided through a long pass filter with a cut-off below 519 nm (FF01-519/LP, Semrock, USA) and detected with a SPCM-AQRH single photon counting module (Excelitas, USA).

Photoluminescence measurements. PL spectra were detected with an Andor SR 163 Spectrograph during continuous exposure with a 405 nm diode laser (LDH-405). The background correction was done by dark current measurement.

FDTD Simulations. A commercial-grade simulator based on the finitedifference

time-domain (FDTD) method was used to perform the calculations (Lumerical FDTD, version 8.16). To simulate the optical response, a total-field scattered-field source was used, and the frequency points were set to be half the wavelength span. I used perfectly matched layer boundary conditions (BC) in all principal directions with a linearly polarized plane wave source. Monitor boxes were used to obtain the optical responses of the system. For the dielectric properties of gold and silver, data from Johnson and Christy[51] and CRC[85] were fitted using six coefficients for gold and five for silver. Both fits had an RMS error of 0.2. For simulating the coupling interactions, we added a Lorentz Oscillator to resemble the optically active layer inside the cavity. All simulations reached an auto-shutoff of at least 10^{-5} before reaching 300 fs simulation time. For the best simulation stability, the mesh area was chosen to be at least 100 nm larger than the existing structure in all three principal directions. For the simulation of the coupling interactions, we employed a Lorentz model layer inside the cavity spacing.

Scanning electron microscopy and Focused Ion Beam cuts were done with a NEON 40 (Carl Zeiss AG) microscope with an Everhart-Thornley detector.

UV-Vis-NR spectroscopy. Extinction spectra were recorded with a Cary 5000 spectrometer (Agilent, USA).

Atomic Force Microscopy. AFM measurements for surface characterization were performed on a Dimension NanoScope 5 with tapping mode.

Spectroscopic Ellipsometry The thickness of thin layers was determined using a RC2 Ellipsometer from J.A. Woollam.

Fabrication Methods

Laser Interference Lithography. Optical grating masters were fabricated by LIL. The beam of a He-Cd Laser operating with 325/442 nm emission wavelength (Kimmon IK5351R-D) was spatially filtered to get a well-defined gaussian beam profile. The beam was then split into two separate beams with a non-polarizing UV fused silica plate beamsplitter (BSW20, Thorlabs Inc.) and recombined with a defined angle, which results in a line patterns with periodicities between 200 nm and 1 µm due to interference taking place between both beams. The gratings were then recorded on a

substrate carrying commercially available photoresists (microresist GmbH). Development of the periodic nano arrays was done with respective basic development solutions with development times generally varying between 20 s and 120 s. The gratings are then rinsed with ultrapure water (Merck Milipore) and dried using nitrogen.

Soft Lithographic manufacturing of elastic nanostructures. Soft Lithography was employed to fabricate elastic molds of the as prepared periodic nanostructures using an h-PDMS/Sylgard 184 composite stamp. 3.4 g of (7-8% vinylmethylsiloxane)-(dimethylsiloxane) copolymer (VDT-731, Gelest Inc.) were mixed with two drops of a Platinum-divinyltetramethyldisiloxane complex catalyst (SIP6831.2LC, Gelest Inc.) and one drop of 2,4,6,8Tetramethyl2,4,6,8-tetravinylcyclotetrasiloxane (396281, Sigma Aldrich) under steady stirring and then degassed until no further bubbles in the mixture were visible. 1 g of (25-35% Methylhydrosiloxane)(dimethylsiloxane) copolymer was added under stirring and a thin layer of the mixture was spincoated onto the LIL substrate (1000 rpm, 40 s). The substrate then was placed on a 60° hot heating plate for 30 min. Thereafter, the substrate was put into a small petri dish and covered with a 0.5 cm layer of Sylgard 184 (Dow Corning) and cured in an oven at 80 ° for one hour. The stamp was extracted by breaking the petri dish and carefully lifting the mold from the substrate. Possible remains of the Photoresist were removed by rinsing with ethanole and drying with nitrogen.

Substrate preparation for nanoparticle-on-mirror (NPoM) cavities. A gold film with a thickness of 50 nm was evaporated onto a clean glass slide (Menzel) using physical vapor deposition (HEX-L by Korvus Technology Ltd, Newington, UK). The substrate was then incubated in a 1 mM solution of (11-mercaptoundecyl)-N,N,N-trimethylammonium bromide (Sigma Aldrich) to form a positively-charged selfassembled monolayer. The thickness was determined to be 1.5 nm using spectroscopic ellipsometry. A monolayer of thioglycolic acid functionalized AgInS quantum dots (QDs) was assembled by placing the sample into an aqueous QD dispersion for 30 minutes at room temperature. The formation of a homogenous layer of AgInS QDs was verified using fluorescence lifetime imaging (FLIM) and AFM. An additional polymeric spacer was applied by (repeatedly) dip-coating the sample into (alternating) solutions of poly(allylamine hydrochloride) (PAH) (0.1 mg/mL; 0.5 mM NaCl) and polystyrene sulfonate (PSS) (0.1 mg/mL; 0.5 mM NaCl) each for 60 seconds. Between each layer-

by-layer assembly step, the sample was rinsed in ultrapure water (Merck Millipore) for 30 s. Each PAH/PSS monolayer is estimated to be 1-2 nm in thickness, as measured by ellipsometry. The metallic nanoparticles were applied by drop casting onto the substrate for 30 seconds, followed by rinsing with purified water and nitrogen drying.

Chapter

4 Results and Discussion

4.1 Plasmonic Colloid-to-Film-Coupled Cavities

An appealing way to exploit the optoelectronic properties of plasmon resonances is to assemble plasmonic colloids into structures that can modulate photons in analogy to electronic devices like transistors with emerging non-linear optical effects.[39] By choosing suitable design parameters and proper physical-chemical techniques, a plethora of systems is accessible with colloidal methods. A promising way to to build functional plasmonic nanostructures are noble metal nanoparticles that are assembled on thin metal layers. This particle-to-film geometry resembles classic optical resonators[56,86,87] and induces high electromagnetic fields in the gap between metal and surface.[88] Such plasmonic cavities show great potential for applications like sensing and optical modulation[89–92], biomedical applications[93,94] as well as information processing and transmission.[95] Plasmonic cavities can be furthermore employed for generation and detection of non-linear optics like strong coupling or single photon emission.[36,96,97] Plasmonic colloids coupled to metal mirrors are termed nanoparticle-on-mirror (NPoM)[98] and usually employ gold and silver as material for the particles and the metallic thin films.[28,98–101] By varying well adjustable parameters like the size, shape and composition of the nanoparticles or the particle-to-film distance, the optical properties of the cavities can be tuned precisely since plasmon resonaces are sensitive towards changes in their immediate dielectric environment.[102–104]

Due to the strong electromagnetic fields that are induced in NPoM-type cavities, they are able to interact with photoluminescent compounds like fluorophores, semiconductor quantum dots or 2D-crystals.[30,105,106] This happens due to electromagnetic

coupling between the plasmonic cavity and the transition dipole moment of the emitters. It is possible to quantify this interaction by estimating the coupling strength g, that depends on the energetic overlap of the plasmon and the PL as well as the relative position and orientation of the emitter.[20,107,108]

$$g(\hat{r}, \hat{e}, \omega) = \mu \cdot E(\hat{r}, \hat{e}, \omega) \tag{4.1}$$

Equation 4.1 describes the the coupling strength g in respect to the emitter position $\hat{r}$, the emitter orientation $\hat{e}$ and the resonance frequency ω. μ is the transition dipole moment of the emitter and E the amplitude of the electric field. Further important properties that affect the interactions between a plasmonic cavity and emitters are the quality factor Q and the modal volume V of the plasmonic cavity resonance. The Purcell factor P gives the radiative decay enhancement of emitters inside a cavity:[109,110]

$$P = \frac{3}{4\pi^2} \left(\frac{\lambda}{n}\right)^3 \frac{Q}{V} \tag{4.2}$$

In this section, FDTD simulations are employed to investigate how the parameters of colloidal-based metal nanostructures can be used to design a NPoM cavity with defined optical parameters and strong electromagnetic field enhancement. The resulting cavity design is then used to simulate the radiative processes of a resonant emitter in dependence of its spatial properties $\hat{r}$ and $\hat{e}$. The results show that colloidal fabrication methods can be used to tailor the optical properties of NPoM-type cavities that enhance radiative properties of emitters.[FG1]

Results and Discussion

A well-defined cavity resonance wavelength is required to energetically overlap with the photoluminescence of an emitter. This can be achieved in two ways for cavities that consist of colloidal metal nanoparticles: by changing the particle properties and by altering the gap size between the mirror and the plasmonic colloid. One of the most common NPoM geometries is a colloidal gold nanosphere assembled onto a thin film of gold. The resulting cavity feature strong field enhancements confined into low modal volumes due to the spherical particle shape. The cavity resonance of a sphere-

to-film coupled setup is tunable by the particle-to-film distance due to the coupling of the LSPR of the particle and SPR of the mirror.

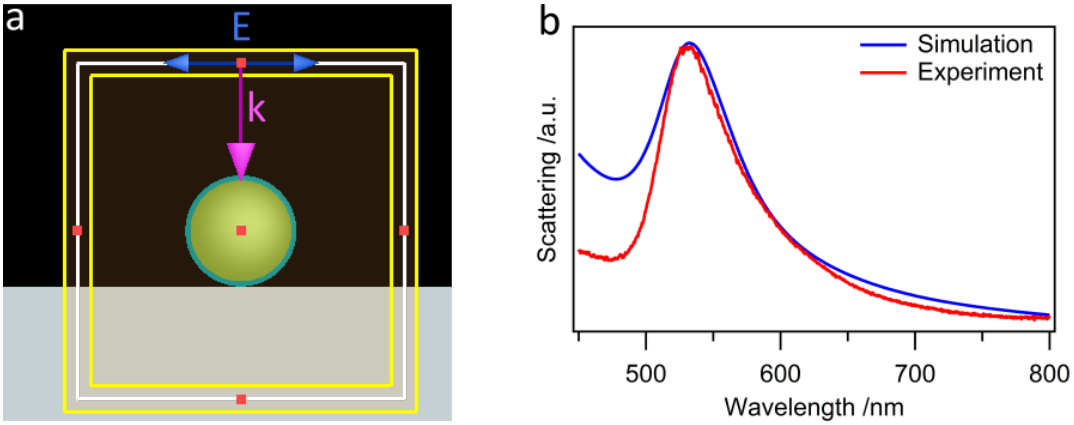

Figure 4.1: Basic plasmonic properties of a colloidal gold nanosphere (AuNS). (a) shows an exemplary picture from the simulation setup in the FDTD solver used to carry out the simulations. The gold sphere is covered by a dielectric shell that resembles surfactant coating and placed on a dielectric substrate (SiO_2). The vectors E and k show the incident electric field and wave vector and the yellow boxes show the volume, in which the elelctromagnetic signals are detected. (b) shows the results from such a FDTD simulation (blue line). An additional spectrum from experimental data (red line) is introduced to verify the simulation.

To approach simulations on the optical properties of such plasmonic NPoM cavities, a gold nanosphere with a diameter D of 79 nm and a particle-to-film distance d of 4 nm (given by the thickness of the dielectric shell) on a dielectric substrate is simulated. The results can be used to determine the initial plasmonic properties of the colloid used for this system (figure 4.1). The simulated scattering of the AuNS shows a characteristic resonance peak at 530 nm, which is in high agreement with an experimentally obtained scattering signal of the respective AuNS on a glass substrate. The simulated σ_{sct} resembles the experimental spectrum well regarding the peak position and the Full Width Half Maximum (FWHM). This nanoparticle-on-dielectric (NPoD) structure can be used as a reference system in order to prove how the LSPR of the particle interacting with the Surface Plasmon Resonance (SPR) of a metallic film can modulate the optical properties of the system. For the next step, the dielectric substrate is replaced by a 50 nm thick Au film to simulate the actual NPoM architecture. As shown in figure 4.2, the plasmon resonance undergoes a significant redshift of 35 nm when being coupled to a gold mirror. This arises as the induced electromagnetic fields, that are induced by the particle and the gold mirror, interfere with each other and lead

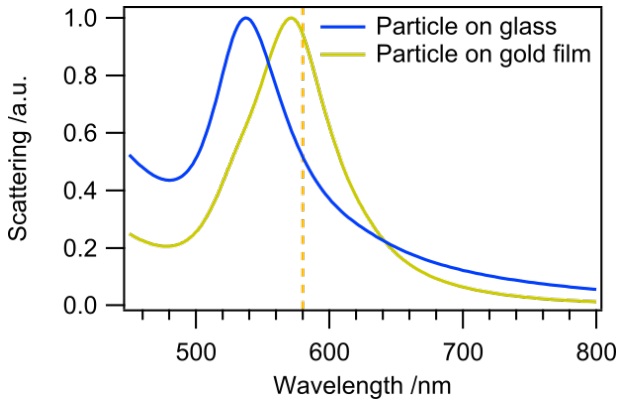

Figure 4.2: Simulated scattering spectra of a gold sphere on a dielectric substrate (blue) and a gold layer (gold). The dashed line marks the emission of the chosen dipole source.

to altered mode energies. This process is shown in detail by exciting the simulation setup with the resonance wavelength and simulating the resulting electric field, the magnetic field and the charge distribution of the defined NPoM system.

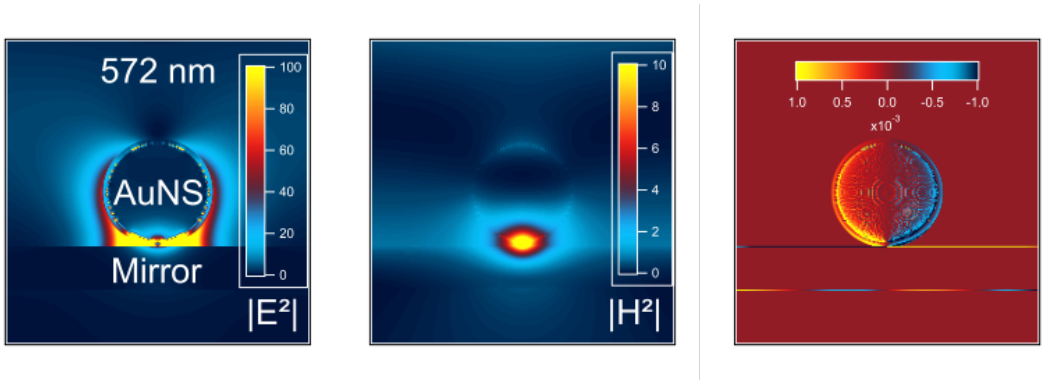

Figure 4.3: Simulation of the electromagnetic fields of a NPoM cavity. (a) is the electric field, (b) the magnetic field and (c) the surface charge induced by an excitation pulse at the resonance wavelength of 572 nm.

As Figure 4.3 shows, the induced electromagnetic field is enhanced and confined to a small modal volume inside the gap between the gold sphere and the mirror. The surface charge plot in figure 4.3c reveals a dipolar mode in the gold sphere, which induces mirror charges on the gold surface. The resulting coupling interactions between particle and mirror allow the modulation of the optical properties by changing the particle-to-film distance d as well as the size of the plasmonic colloid D. A set of different parameters for d and D are calculated to quantify the respective plasmonic properties for each system.

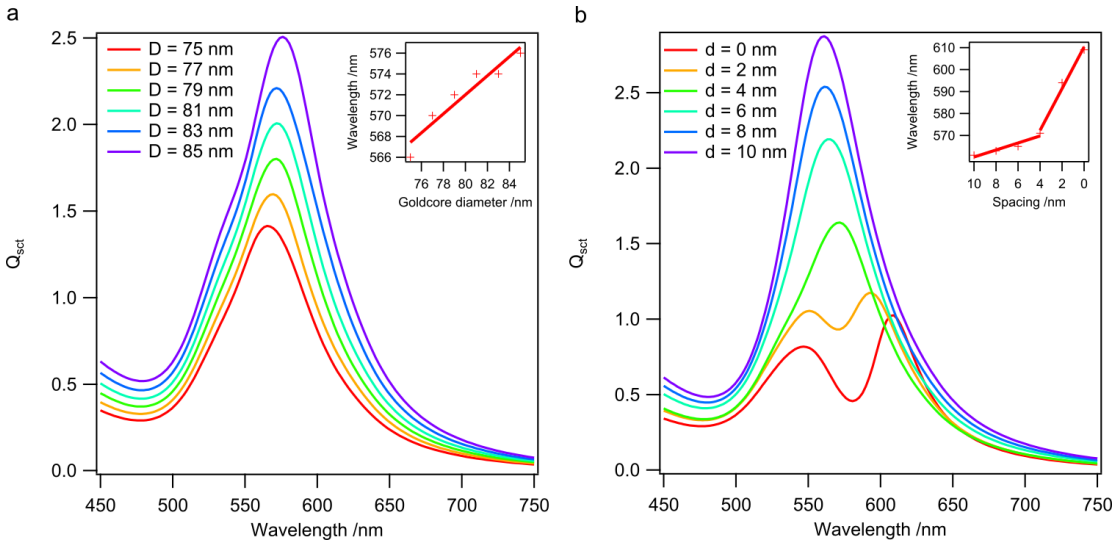

Figure 4.4: Sensitivity of cavity properties towards colloidal design parameters. (a) shows the scattering spectra of the NPoM cavity with nanoparticle diameter D changing from 74 nm to 86 nm with a fixed particle-to-film distance of 4 nm. (b) shows the scattering spectra for particle-to-film distances d from 0 nm to 10 nm.

The simulations in figure 4.4 show that both of the parameters are able to tune the optical response of the cavity. Increasing the particle diameter D from 74 nm to 86 nm while keeping d at 4 nm, the cavity resonance changes by 9 nm in an almost linear fashion. The rather low sensitivity $S = \frac{\Delta\lambda}{\Delta D}$ of 1.1 is relevant as the modal volume and the coupling interaction with the gold film are only slightly affected by the changes in AuNS size. More pronounced modulation of the optical properties are observed in figure 4.4b for varying the particle-to-film distance d with a fixed D of 79 nm. When the gap size is tuned from 10 nm to 4 nm, the cavity resonances are slighty redshifted with $S = \frac{\Delta\lambda}{\Delta d} = 1.6$. Further reduction of d below 4 nm leads to a jump in the sensitivity ($S = 9.5$) and the dipolar mode is redshifted way more pronounced. For a d of 2 nm and 0 nm, the dipolar resonance becomes a pronounced single peak while the energetically higher mode at 550 nm is not affected by the gold film coupling.

So far it was shown that the NPoM cavity induces strong electromagnetic fields in a small modal volume and has versatile cavity resonances with narrow FWHM. These properties are crucial for optical resonators[111] and can lead to strong light-matter interactions with an emitter inside the cavity. These interactions are now studied by introducing a dipole source with an emission wavelength of 580 nm within the gap between gold particle and mirror, which resembles an photoluminescent emitter.

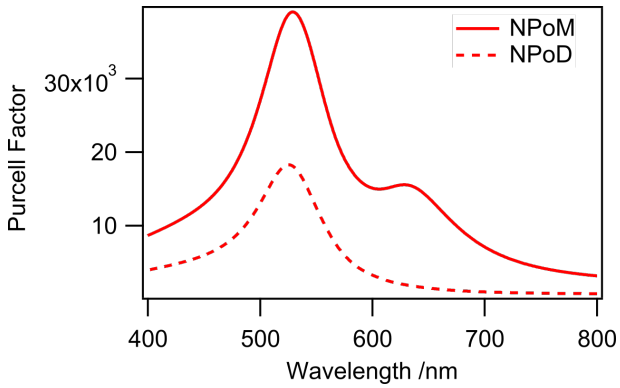

Figure 4.5: FDTD simulation of the Purcell factor for the NPoM cavity (solid line) as well as the NPoD cavity (dashed line) for reference.

By simulating the changes of the dipole power caused by the cavity, one can obtain the Purcell factor P of such systems. In figure 4.5, P is shown for the NPoM cavity and for the respective NPoD system for reference. The cavity has a high Purcell factor of 39000, which is more than twice the enhancement the emitters experience in the NPoD system. The high P states that the radiative properties of the dipole source are enhanced. Energy that is emitted by the dipole source can be radiative (i.e. a photon is emitted) or nonradiative. The rates for both of the processes are simulated to estimate how the emitter is affected by the electromagnetic field in the cavity.

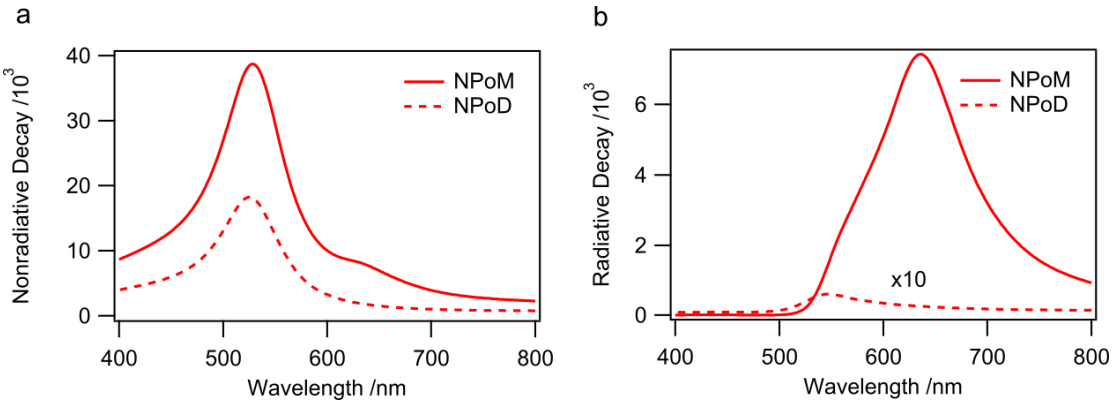

Figure 4.6: Simulated decay rates of a cavity-coupled dipole source. (a) shows the non-radiative decay and (b) the radiative decay of the NPoM system (solid line) as well as for the NPoD reference (dashed line).

The nonradiatve decay rates k_{nr} and the radiative decay rates k_r in figure 4.6 show that k_{nr} increases in the same order of magnitude for the NPoM and the NPoD system. The higher nonradiative decay for the NPoM system is caused by the more dissipative

nature of the plasmonic system compared to the NPoD reference. The radiative decay rate of the NPoM system exceeds the NPoD by more than two orders of magnitude (120 fold), which indicates that the local fields induced in the plasmonic system have a much higher impact on k_r as compared to k_{nr}, since additional radiative decay states are present due to the plasmonic environment.[112] The obtained data are now used to calculate the quantum efficiency QE of the cavity-coupled dipole in order to quantify the enhanced emission properties. The calculated QE in figure 4.7 shows that the

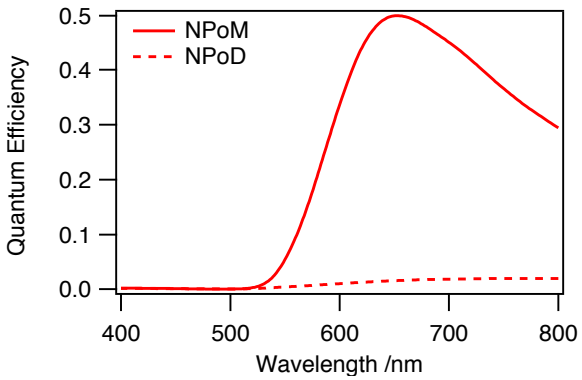

Figure 4.7: Calculated Quantum Efficiency of the NPoM (solid line) and the NPoD reference system (dashed line).

enhancement of k_r surpasses the increase in k_{nr} inside the NPoM. Although both systems show an increase of QE at wavelengths above 530 nm (i.e. optically responsive frequencies for the AuNS), the NPoM possesses 28-fold higher QE.

As equation 4.1 shows, the absolute position of the emitter in the electromagnetic field has a direct effect on the coupling strength of the dipole coupling to the surrounding field. To investigate the effect of the spatial position $\hat{r}$ and relative orientation $\hat{e}$ of the dipole on the coupling strength, its position in the simulation setup is varied.

Radiative decay rates are simulated for three different dipole positions as illustrated in figure 4.8: directly between the AuNS and the gold mirror (red), 90° further along the particle surface (green) and at the opposite end of the gold sphere (blue) and each with a parallel (dashed line) and perpendicular (solid line) dipole orientation. The colour of the simulated decay rate plots correspond to the positions marked in the scheme in figure 4.8a. Although all dipole sources show enhanced values for k_r, the emitters that are placed inside the confined modal volume of the cavity have several orders of magnitude higher decay rate enhancement. The dipole axis orientation

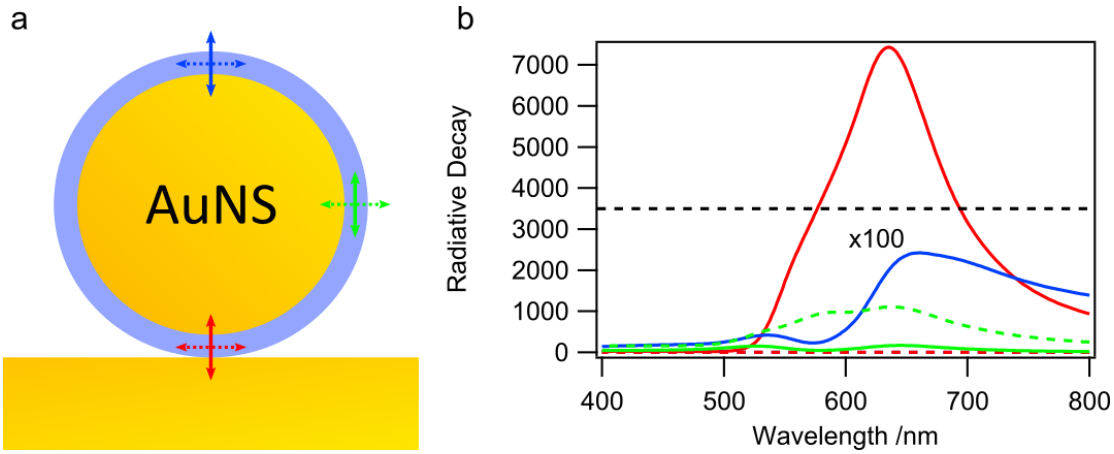

Figure 4.8: Position and orientation dependent radiative decay rates of a dipole emitter. (a) The sketch illustrates the different places and relative orientation of the dipole in the simulation setup. (b) Radiative decay rates for each dipole source position in perpendicular (solid) and parallel (dashed) dipole orientation. The graphs that are found beneath the dashed line are all 100fold enhanced for better visibility.

is just as important as it can be demonstrated for the dipole inside the cavity (red curves). While perpendicular orientation (solid arrows) leads to the biggest detected increase of the radiative decay, it is almost absent for a dipole orientation parallel to the gold mirror (dashed arrows). This can be explained since the perpendicularly oriented dipole emission excites the cavity resonance and gets confined in the cavity mode while radiation emitted parallel to the gold surface can propagate outside the cavity without inducing light-matter interactions.

Conclusion

In this section, the optical properties of a plasmonic particle-to-film coupled cavity system was studied using electromagnetic simulations. It could be shown how the local field enhancement can be increased by two orders of magnitude in the gap between a colloidal gold sphere and a gold mirror. By changing the particle size and the particle-to-film distance, the dipolar cavity resonance can be tuned with high precision. The system was then extended by introducing a dipole source into the cavity. Further simulations showed that the radiative decay properties of the dipole source are strongly affected by the plasmonic cavity. A high Purcell factor and enhanced QE prove that the plasmonic cavity can compensate its intrinsic energetic losses by coherent energy transfer between cavity mode and dipole emitter. Simulations for

different positions and orientations of the dipole showed quantitatively how crucial these parameters are in order to increase the light-matter interactions in plasmonic cavities. The found data can help to understand the complex light-matter interactions that occur when plasmons are coupling with emitters and to design efficient plasmonic systems for coherent energy transfer.

4.2 Fluorescent Hectorites in Colloid-to-Film-Coupled Cavities

The previous chapter showed that the optical properties of plasmonic cavities and the position of the emitters that were sandwiched in between a plasmonic particle and a metallic film are crucial design parameters for coherent energy transfer between both components. Colloidal building blocks assembled with physical-chemical methods are suitable for fabricating such plasmonic cavities that meet these demands. To build NPoM cavities with desired plasmon-exciton interactions, bottom-up self-assembly methods have successfully been employed in the recent years using host-guest chemistry[99], surface-chemical methods[103] or chemical linkers.[81] When single emitters and surface plasmon resonances are exchanging energy in a sufficiently coherent fashion, characteristic modulations of the optical properties are generated in the cavity. Two distinguished peaks in the scattering spectrum can occur when coupled light-matter states are formed[37] and the enhanced radiative emission of the emitters in plasmonic cavities can lead to a further increase in the photoluminescence intensity[96], shorter lifetimes[100] and enhanced photostability[113]. These features allow detailed analysis of the plasmon-exciton interactions and will also allow an estimation to determine if the system is in the weak, intermediate or strong coupling regime.

This part of the thesis shows how fluorescent dye-loaded hectorite structures are used to build such NPoM cavities with precise spatial features in regards to the cavity gap size and the embedded emitters. Hectorites are anorganic silicate compounds that possess atomically flat surfaces and defined structure thicknesses in the nanometer range with particle aspect ratios of 20000 and more.[114] Due to strong electrostatic charges of the hectorite interlayers, they can intercalate photoluminescent materials like organic dyes with uniform emitter distribution.[115] Besides the uniform lateral position of each dye molecule, the emitters also show defined vertical orientations of approximately 30° with respect to the surface plane.[116] These structural and optical properties of dye-loaded sodium silicate particles are suitable to build gold sphere-to-film coupled cavities with defined parameters on macroscopic scale using colloidal bottom-up self-assembly methods. The properties of the obtained structures are then

studied in detail using dark-field imaging and spectroscopy, confocal fluorescence microscopy and FLIM.

The hectorites with intercalated C-16-Stilbazolium were synthesized and provided by Matthias Stöter from the group of Prof. Josef Breu at University of Bayreuth.

The plasmonic nanoparticles were provided by Anja Maria Steiner from the group of Prof. Andreas Fery.

Results and Discussion

Before the placing the hectorites in NPoM cavities, the particles are characterized in terms of shape, thickness and fluorescence emission.

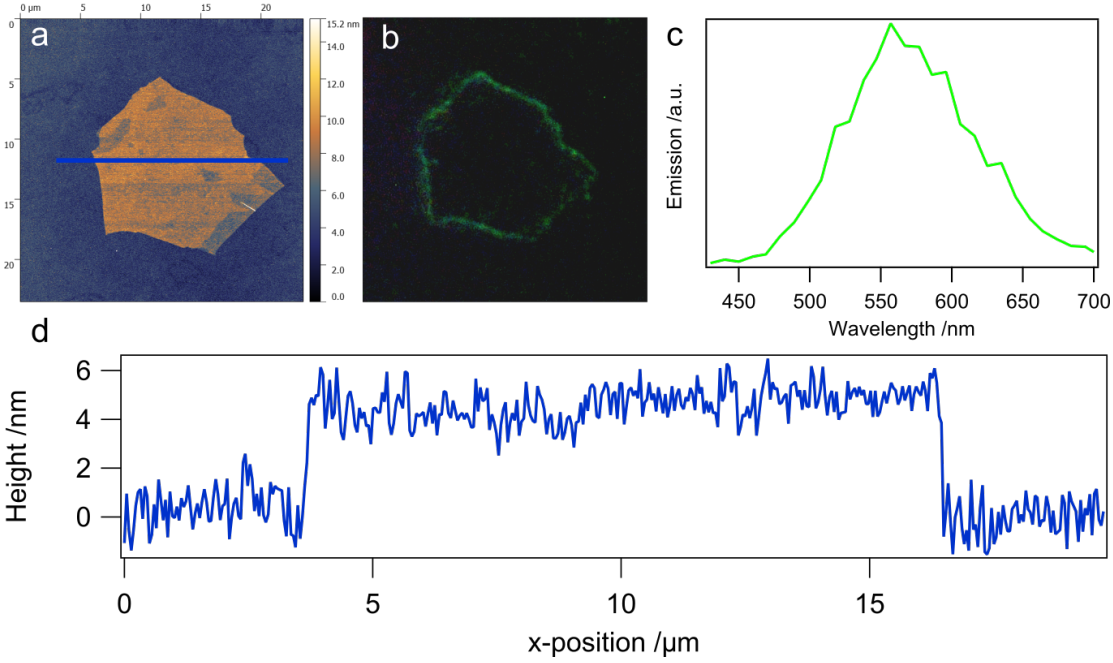

Figure 4.9: Overview on fluorescent hectorites: (a+d) AFM image of a single hectorite particle on a glass substrate and the respective profile plot.(b) The same flake identified using dark-field microscopy. (c) Photoluminescence spectrum of single hectorite particles.

Atomic Foce Microscopy (AFM) measurements for a representative hectorite particle are shown in figure 4.9. The selected flake has a uniform height of 4 nm and a lateral dimension of more then 10 µm, which corresponds to an aspect ratio of about 2500. Additional dark-field imaging of the same particle shows that scattering only takes place at the edges of the particles. A confocal fluorescence microscopy spectrum of single hectorite flakes features an emission peak at 570 nm. These properties

make them suitable for application as dielectric spacers that furthermore contain oriented emitters. Furhtermore, their stability in aqueous solution makes it possible to assemble the hectorites onto surfaces in a macroscopic fashion. The high aspect ratios of these hectorite flakes also lead to strong Van-der-Waals interactions between the silicate flakes and the substrate surface and result in a plane adsorption. A hectorite-treated glass substrate is examined with dark-field microscopy and scanning electron microscopy (SEM). The obtained images are shown in figure 4.10 and validate that

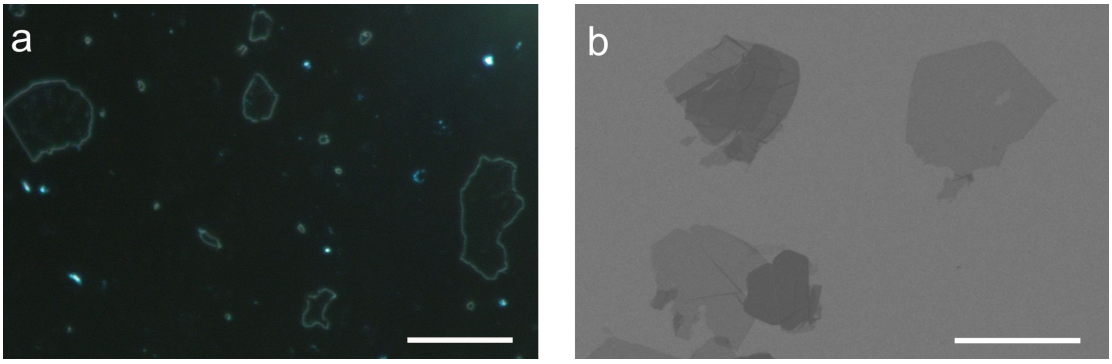

Figure 4.10: Dark-field Microscopy image (a) and Scanning Electron Microscopy image (b) of silicate flakes on a substrate. Scalebar is 20 µm.

the hectorite flakes are evenly adsorbed to the glass substrate. The even surface, defined height and large surface areas of the hectorites allow their easy incorporation in NPoM cavities. This is done by dropcasting a hectorite solution onto a glass substrate carrying a 50 nm gold film. An aqueous solution of 71 nm spherical gold nanoparticles is subsequently dropcasted onto the substrate. Due to the high coverage of hectorites on the surface, the colloidal particles will adsorb eventually onto the hectorite flakes and thus form a NPoM cavity with the uniformly intercalated fluorophores embedded in between the gold mirror and the gold sphere. The 4 nm thick hectorites and the approximately 2 nm thick layer of cetyltrimethylammonium chloride (CTAC) that is employed to stabilize the AuNS colloids result in a NPoM with a 6 nm gap size. FDTD simulations of this cavity geometry (figure 4.11) show energetic overlap between the cavity resonance of 572 nm and the photoluminescence of 570 nm. The energetic overlap between the cavity mode and the emission is important as the excited states of the fluorophores experience an enhanced local density of states (LDOS) in a resonant field to which they can decay.[36] These light-matter interactions result in coherent energy transfer if the losses introduced by the damping of the plasmonic cavity and the emit-

ter are exceeded.

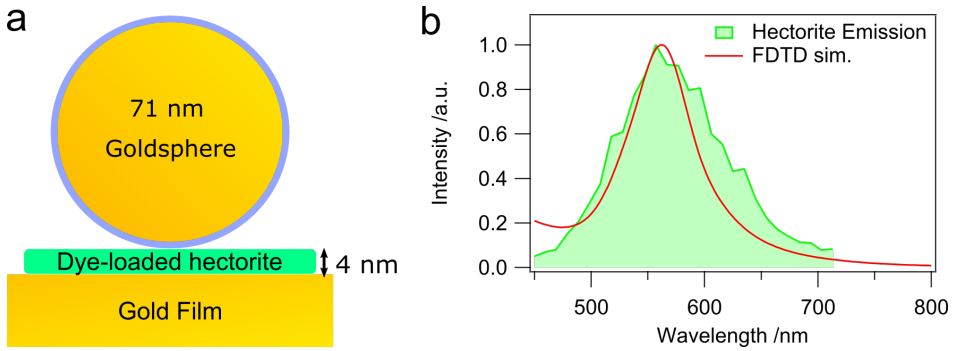

Figure 4.11: NPoM cavity with embedded fluorescent hectorites. (a) Schematic illustration of the cavity cross section. (b) Simulated scattering spectrum of the cavity (red line) and photoluminescence spectrum of the dye-loaded hectorite (green).

Dark-field scattering spectroscopy of the NPoM can now provide quantitative information on the coupling strength g as the mode hybridization, that is formed in efficiently coupled plasmon-exciton systems, corresponds to the energetic gap between the mixed states.[31]

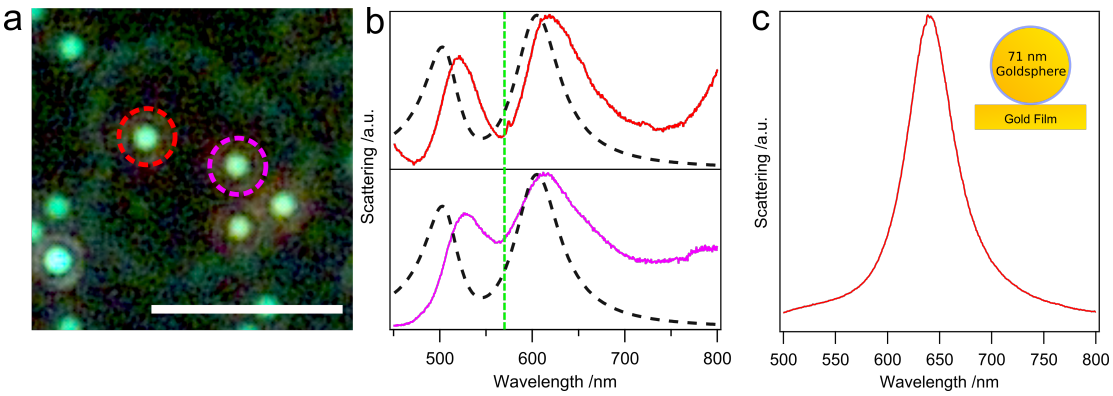

Figure 4.12: Dark-field studies of NPoM cavities with embedded hectorite. (a) Dark-field image of a hectorite flake containing several AuNS. The dashed circles mark the measured cavities. Scalebar is 5 µm. (b) Scattering spectroscopy on the marked NPoM cavities (red and violet lines) and simulated scattering cross section of a respective coupled-oscillator system (dashed black line). The dashed green line marks the fluorescence emission of the hectorite. (c) Reference measurements of a AuNS on a gold mirror without fluorescent emitter in between.

The measurements display two distinguished peaks in the scattering spectra of the NPoM cavities (figure 4.12b). This splitting of the cavity scattering signal suggests the presence of intermediate or strong coupling between the fluorophores and the plasmon resonance. The spectral position of the dip at 570 nm corresponds very well to

the plasmon resonance of the uncoupled plasmonic cavity and the fluorescence emission (fig 4.11), which can be explained when the system is described using a coupled oscillator model:[117]

$$\omega_{\pm} = \frac{1}{2}\left(\omega_{cav} + \omega_0\right) \pm \sqrt{g^2 + \frac{\delta^2}{4}} \tag{4.3}$$

where $\omega_{\pm}$ represents the hybridized mode frequencies, ω_{cav} the cavity resonance, ω_0 the emission frequency, g the coupling strength and δ the detuning between the resonance frequencies of the cavity and the emitter. The high overlap between cavity resonance and photoluminescence emission results in a low detuning, which results in a higher energetic gap between the hybridized light-matter states. This model also shows how the coupling strength g can be directly derived from the scattering spectra as it corresponds to half of the peak-to-peak distance. This results in g values of 187 meV and 162 meV for the analysed cavities. Analytical calculations of the coupled system (eq. 3.14) show similar spectral features (figure 4.12b). For reference, a particle-to-film coupled system without embedded hectorite is characterized. The resulting scattering spectrum (figure 4.12c) shows a single peak for the cavity resonance. These results suggest that the system approaches the intermediate coupling regime.[36]

For complementary investigation on the light-matter actions in the NPoM cavities, the photoluminescence can be taken into account. As shown in the previous section, the radiative decay rate k_r and the nonradiative decay rate k_{nr} of cavity-coupled emitters are affected by the enhanced electromagnetic fields, which gives rise to increased QE and photon emission rate. Confocal fluorescence microscopy and FLIM is used to analyse how the emission of the hectorites is affected in cavities.

The detected emission map of a silicate flake with several sphere-to-film coupled cavities in figure 4.13 shows 3-fold enhanced PL intensity, which proves that the emitters are affected by the cavity significantly. The overall photon counts are extremely low due to fluorescence quenching of the gold film and thus a spectroscopic analysis of the emission is not possible. The quenching also leads to lifetimes that are too short for measurement techniques like TCSPC, yet the fluorescence lifetime is of crucial importance for quantifying optoelectronic properties of materials[118]. For further advances in tailoring and quantifying the optical properties of these systems, the problems regarding the low signal-to-noise ratio and the short fluorescence lifetime of the dye-loaded hectorites need to be solved, which is shown in the following section.

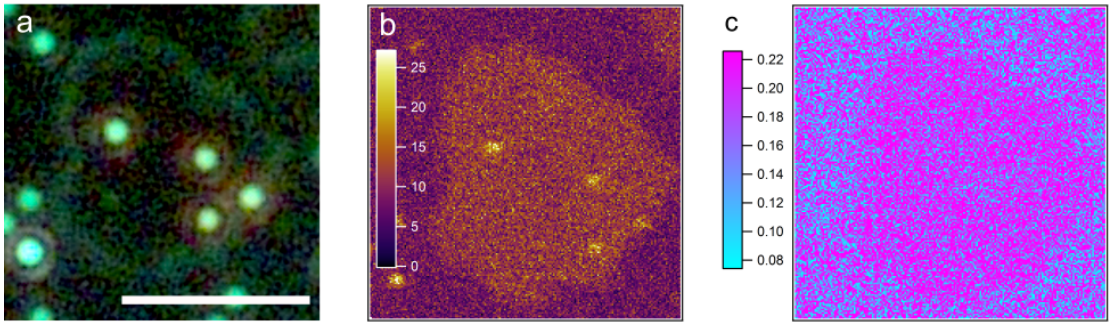

Figure 4.13: Analysis of the modulated PL of cavity-embedded hectorites. (a) Dark-field microscopy image of the exemplary silicate flake containing several NPoM cavities. (b) Confocal Fluorescence Microscopy scan of the same hectorite flake. (c) Fluorescence Lifetime Image of the same structure.

Conclusion

In this part of the thesis, colloidal gold nanoparticles and fluorescent dye-loaded hectorites were used to assemble NPoM type cavities with a defined gap size of 6 nm and fixed emitter position. FDTD simulations confirmed energetic overlap between the cavity plasmon resonance and the fluorescence emission of the C-16-Stilbazolium fluorophores that are intercalated in the hectorites. The hectorite-intercalated fluorophores possess defined spatial distribution and vertical orientation that result in uniform photoluminescence properties. AFM, dark-field mircroscopy and SEM imaging were used to verify the structural properties of hectorite particles that were then attached to a thin gold layer. Colloidal gold spheres were assembled onto the even hectorite flakes to form NPoM cavities with the fluorescent dye sandwiched in between gold film and AuNS. Dark-field scattering spectroscopy showed that hybridized cavity modes are formed and furthermore suggest intermediate or strong coupling between plasmons and excitons. Confocal fluorescence microscopy showed enhanced PL intensity emerging from the cavities, further indicating the strong light-matter interactions that are produced in the small modal volume between gold sphere and gold film. The quenching of the organic dye intercalated in the hectorites yet leads to low signal-to-noise ratios and lifetimes that are to short for quantification. For further investigation on NPoM systems, emitters with long lifetimes and PL intensity are therefore crucial to improve the cavities in order for complementary studies on their optical properties. This high precision of controlling the optical and radiative proper-

ties of plasmonic cavities with embedded emitters can help to design and understand light-matter interactions for optoelectronic applications like single photon sources or quantum information technologies.

4.3 Semiconductor Nanocrystals in Colloid-to-Film Coupled Cavities

Introduction

Plasmonic cavity-coupled emitters are highly appealing systems to study light-matter interactions due to their strong and confined nearfield enhancement upon excitation.[119] Such systems have proven to be promising candidates for tailoring photonic properties at exceptionally small mode volumes.[90,120] Recently, colloidal approaches have been introduced to continue this development by incorporating the emitting material (molecular excitons or quantum dots) using host-guest chemistry[28], simple immersion techniques[121] or polyelectrolyte multilayers[100]. The fast energy transfer between excitonic quantum emitters and the cavity system leads to hybridized light-matter states provided that the plasmon-exciton coupling is sufficient.[21,108] In order to employ this optoelectronic process for applications like optical circuits, the optical properties of the structure itself must be modulated.[122] Besides tailoring the single cavities it is necessary to find methods for large-scale fabrication in order to employ them in devices like perfect absorbers or optical circuits.[91,122]

Here, the radiative properties for a set of colloid-to-film coupled cavities are studied as determined by their composition. A combination of a well-defined self-assembled monolayer of thiolates with a polymeric film formed using layer-by-layer deposition methods is used to achieve a homogenous and emitting spacer layer of various thicknesses. Gold spheres and silver cubes are employed as plasmonic colloids, and ternary metal-chalcogenide quantum dots with a long photoluminescence lifetime (100 ns) and broad emission range (FWHM=304 meV) are chosen as optically active material. By applying a combination of surface and optical characterization methods, most notably dark-field spectroscopy, FLIM and TCSPC, the presence of light-matter interactions can be established and the optical properties can be studied statistically on cm^2 scale. Electromagnetic simulation methods allow to comprehend the coupling interactions of the system and its sensitivity towards changes in the dielectric environment. This quantification combined with self-assembly makes the colloid-to-film coupled cavities potentially useful for the next generation of optical circuits.[FG3]

The ternary metal-chalcogenide quantum dots were provided by Oleksandr Stroyuk from the group of Prof. Alexander Eychmüller, TU Dresden Germany / National Academy of Sciences of Ukraine, Kiev, Ukraine

The plasmonic colloids were synthesized by Anja Maria Steiner from the group of Prof. Andreas Fery, TU Dresden

Results and Discussion

The fabrication of the colloidal nanocavites starts with a self-assembled monolayer (SAM) of (11-mercaptoundecyl)-N,N,N-trimethylammonium bromide (MUTAB) that is adsorbed on a gold film as a 1.4 nm layer which is confirmed using spectroscopic ellipsometry (RMS=3.197). This method proved to be suitable for bottom-up self-assembly since thiolate-based self-assembled monolayers (SAMs) on gold are easy to generate and offer ordered monolayers on a macroscopic scale.[123–125] Therefore, the surface charge is uniformly distributed and allows the negatively charged thioglycolic acid-capped silver-indium-sulfide (AgInS) particles (3 nm) to adsorb in a homogenous monolayer.

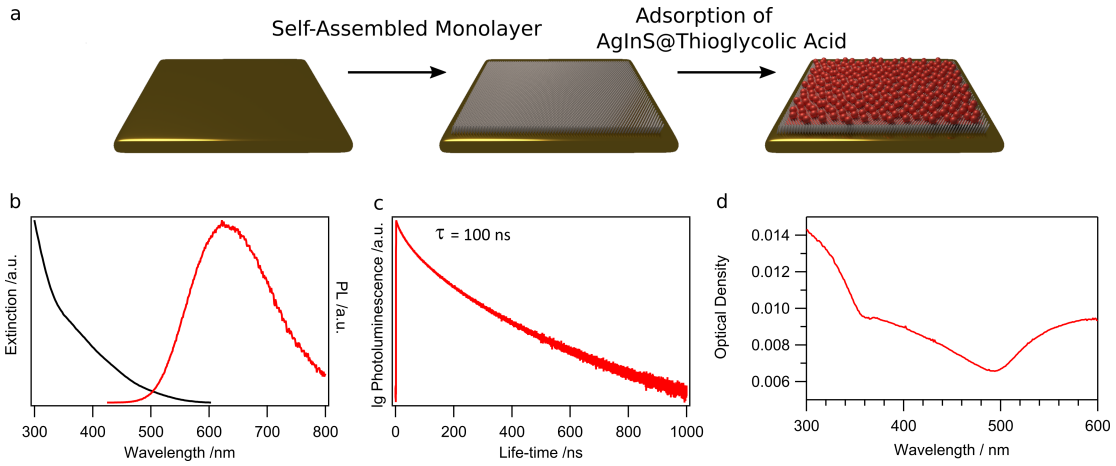

Figure 4.14: Optical properties of ternary metalchalcogenide (AgInS) quantum dots. (a) Illustration of the formation of densely packed colloidal AgInS emitters. (b) Absorption (black line) and emission (red line) of AgInS QDs. (c) TCSPC measurement of the AgInS on glass. (d) Background-corrected extinction spectrum of the AgInS monolayer assembled on a MUTAB monolayer.

The photoluminescence properties of the AgInS are shown in figure 4.14. The extinction is mainly pronounced in the UV-range as it is typical for quantum dots while the emission spectrum shows a broadband emission that covers a wide fraction of the

optical wavelength regime with a FWHM of 304 meV. TCSPC is used to determine the radiative decay of the AgInS quantum dots, which results in an average lifetime of 100 ns. This PL lifetime is an order of magnitude longer than for common fluorescent emitters,[58] which is necessary in order to resolve the radiative properties of cavity-coupled emitters as shown in the previous chapter.

To proof the successful formation of a closely packed AgInS QD layer, its optical density is measured using UV-Vis spectroscopy. The absorbance of the AgInS QDs is mostly determined by the silver(I) content as shown in respective literature.[126,127] The extinction increases almost linear with the increase of the silver concentration in the quantum dots. The molar extinction coefficient of AgInS QDs in terms of silver(I) concentration at 320 nm is 9.6x10^6 $\frac{cm^2}{mol}$. As seen in figure 4.14d, the optical density of the AgInS layer at 320 nm is 0.0132, which corresponds to 1.38x10 $^{-9}$ $\frac{mol}{cm^2}$ or 8.28x10 ^{14} silver species per cm^2. The AgInS particles presented in this work contain 128 Ag^+ ions each. In combination with the determined silver(I) concentration, a AgInS quantum dot density of 6.5x10^{12} particles per cm^2 is determined. Given the fact that a maximal closely packed layer of the 3 nm QDs would theoretically give a density of 11x10^{12} particles per cm^2, it can be concluded that a monolayer or sub-monolayer of the particles is assembled on the substrate.

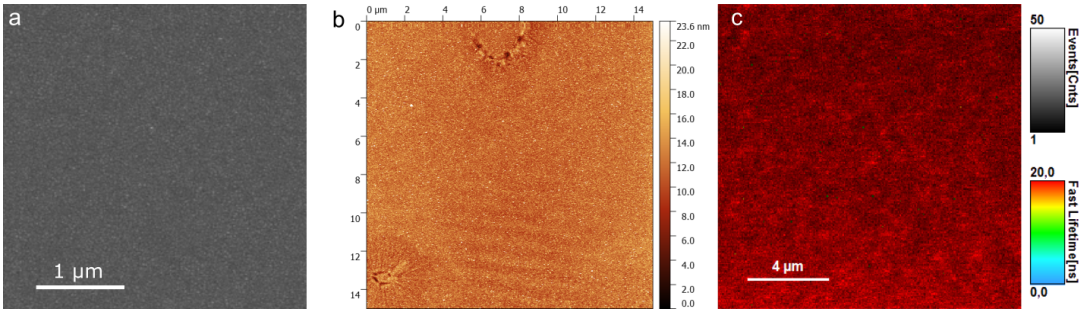

Figure 4.15: Surface characterization of the MUTAB/AgInS/PAH/PSS film. SEM (a), AFM (b) and FLIM (c) measurements of a gold film containing the MUTAB/AgInS/PAH/PSS film.

To tune the distance between the metallic surfaces and to ensure a homogeneous surface, additional polymer spacing was applied using the well-known layer-by-layer assembly method involving poly(allylamine hydrochloride) (PAH) and poly(styrene sulfonate) (PSS).[128–130] Thus, the distance between the metal surfaces was adjusted by including different amounts of polyelectrolyte bilayers. Uniform coverage and low surface roughness of the spacing-emitter layer was verified via AFM, SEM and FLIM

measurements as shown in figure 4.15. By AFM, a RMS surface roughness of 2.045 nm was measured on a 15x15 μm^2 area, and a uniform fluorescence emission signal was detected. The plasmonic colloids were then applied using dropcasting. For the CTAC

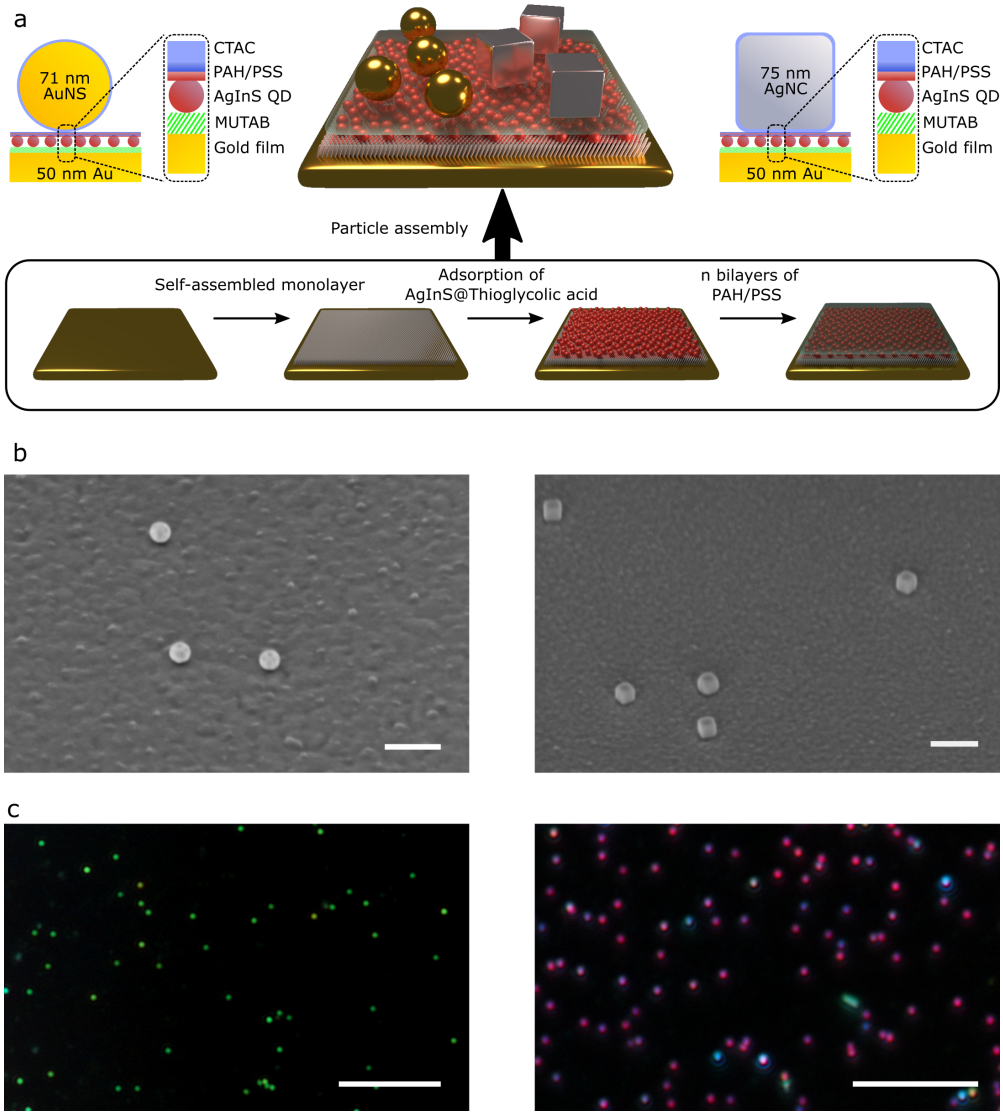

Figure 4.16: (a) Schematic illustration of the self-assembled NPoM cavities. (b) SEM images of single NPoM cavities for gold spheres (left) and silver cubes (right). (c) Dark-field images of gold sphere-to-film coupled cavities (left) and silver cube-to-film coupled cavities (right).

surfactant layer surrounding the nanoparticles, a thickness of 2 nm was assumed from simulations. The final cavity spacing d is therefore made up of the thiolate SAM (1.4 nm), AgInS QDs (3 nm), a variable PAH/PSS-multilayer and the surfactant around the particles (2 nm) as schematically shown in figure 4.16. To ensure that the cavities were

built from single particles, further SEM measurements and dark-field microscopy were employed to study the prepared substrates (Figure 4.17). This combination of self-assembled monolayers and colloidal building blocks makes it possible to manufacture a variety of stable cavity systems featuring different spacings and geometries with low fabrication efforts. A complementary and statistical study on their radiative properties now becomes possible.

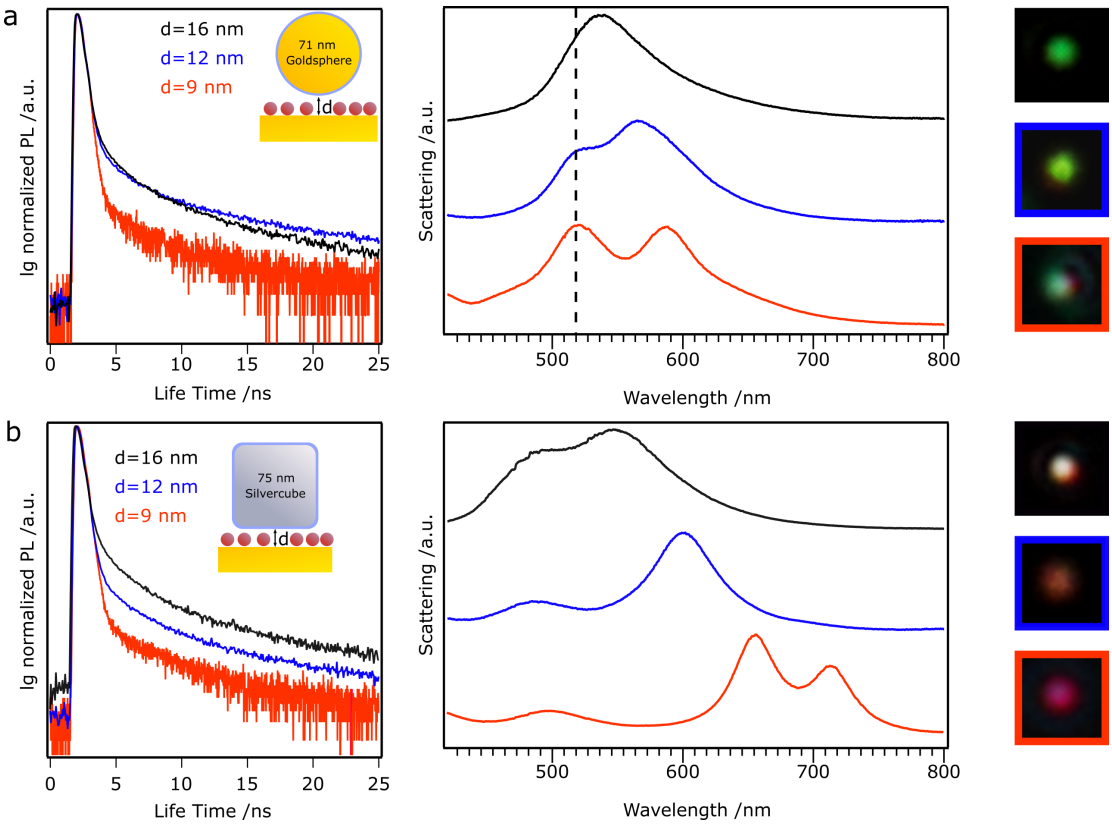

Figure 4.17: Spectroscopic properties of various colloid-to-film coupled setups: Time correlated single photon counting, scattering spectroscopy and dark-field imaging of (a) gold spheres and (b) silver cubes coupled to a gold film with 9 nm (red), 12 nm (green), and 16 nm (purple) cavity spacing. The dashed line in (a) marks the gold film scattering.

Figure 4.17 shows a general evaluation of the different cavity designs chosen to cover a broad range of cavity resonances and light-matter interactions. For quantitative information about the single cavities and their exciton-coupling, single particle scattering spectroscopy and TCSPC was used to directly access the optical properties of the colloid-to-film coupled cavities. TCSPC decay rate measurements of gold spheres and silver cubes were highly sensitive to the particle-to-film distance d. For

gold spheres with 12 nm and 16 nm spacings, similar TCSPC curves were obtained while the 9 nm cavity led to a significantly enhanced decay rate. Silver cubes offer a greater degree of decay rate changes as a clear trend towards shorter lifetimes was detected for decreasing particle-to-film distances. This effect becomes more comprehensive when the single cavity scattering spectra are taken into account. Both particle systems show coupling interactions with the gold mirror as expressed through a spectral redshift. The silver cubes show a large sensitivity $\Delta\lambda/\Delta d$ of 23.7, whereas the gold spheres were less sensitive at 7.1. The higher sensitivity of the cube setup is dominated by the edge geometry rather than the material properties of silver (Figure 4.18).

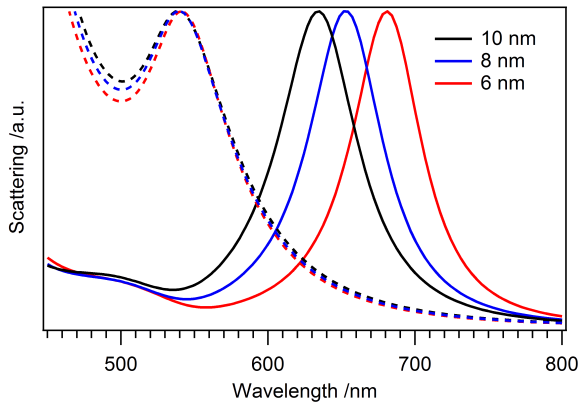

Figure 4.18: FDTD simulations on the sensitivity of a silver sphere (dashed lines) and silver cube (solid lines) with different particle-to-gold film distances.

This relationship is also observable through dark-field microscopy as shown in Figure 4.17. While only minor changes of the color of the cavity scattering cross-section are visible for the sphere-to-film geometry, a more pronounced color variation takes place for the cube-to-film systems. The pronounced peak at 520 nm in the sphere-to-gold film system is most likely caused by scattering of the gold film and not visible in the cube-to-gold film geometry due to the much higher scattering intensity of the silver cubes compared to gold spheres. The most significant observation is the splitting of the cavity resonance for the sub-10 nm cube-to-gold film gap. This mode hybridization is a signature that light-matter interactions between the plasmonic and the excitonic systems are becoming strong enough to overcome the energetic losses of the resonator. Since light-matter interactions are necessary for optical gain, we

further investigated the optical properties of this particular 9 nm silver cube cavity setup. In order to evaluate the suitability of the cube-to-gold film coupled cavities for

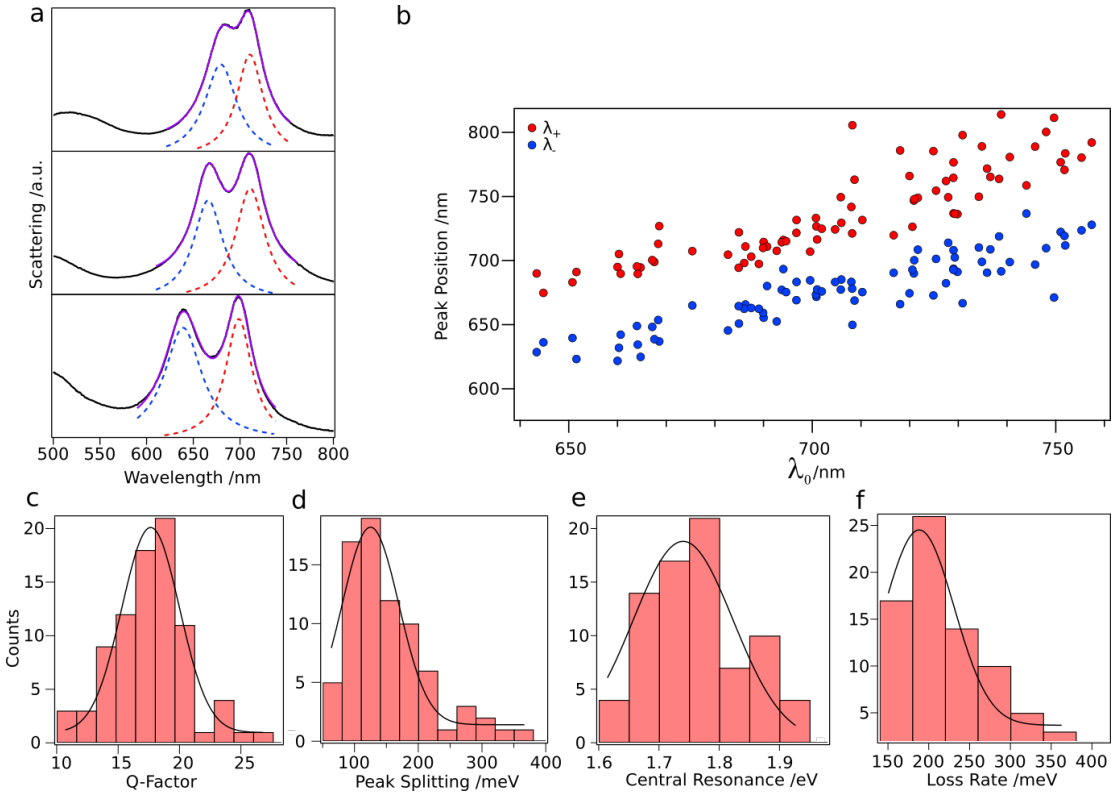

Figure 4.19: Statistical evaluation of silver cube nanocavities at 9 nm spacing: (a) Dark-field scattering spectra of three representative nanocavities. The solid black line shows the measured scattering response. The blue and red dashed lines show the individual Lorentzian fits, and the purple solid lines show the combined fits. (b) Peak position of the hybridized modes with respect to the estimated cavity resonance λ_0. (c-f) Histogram plots and Gaussian fits (black lines) of (c) Q-factor, (d) peak splitting, (e) cavity resonance and (f) loss rate. 77 nanocavities were studied statistically.

tasks that demand strong plasmon-exciton interactions, quantification of the occurring losses γ as well as the coupling strength g is necessary. Another point of interest is the quality factor Q, which is a measure for energetic losses in respect to the resonance wavelength of an optical resonator. The colloidal approach enables statistical measurements of the optical properties of single cavities by dark-field scattering spectroscopy. The required parameters can directly be extracted from the resulting spectra since γ is the spectral FWHM while g is given by the distance between the hybridized plasmon peaks.[117] As discussed in the previous chapter, this can be explained with a coupled-oscillator model that quantifies the coupling strength g between the emitter and the cavity resonance. As Figure 4.19 shows, 77 cube-to-film coupled cavities were

evaluated and the desired parameters were extracted using Lorentzian functions (Figure 4.19a). To visualize the optical range in which our cavities are operational, we also obtained the estimated cavity wavelength λ_0 for each spectrum (Figure 4.19b) by using an additional Lorentzian fit. We found the mean quality factor of the 9 nm cube system to be 16.9 ± 0.2, while typical plasmonic cavities have Q-factors between 5 and 10, although similarly high Q-factors were reported for different cavity geometries.[36,117] The statistical analysis of coupling strength gives a normal distribution with a mean value of 111.5 ± 5.2 meV, which is on the same order of magnitude as published in literature recently.[21] The variations of the coupling strengths are affected by several parameters. On the one hand, the absolute position of the emitters is crucial. Cube-to-metallic film coupled cavities induce large field enhancements near the edges of the cubes and lower field strengths in the center. Varying positions of the AgInS particles in each cavity will therefore lead to different levels of interaction. On the other hand, the number of emitters N also affects the cavity coupling.[104,131] For the cube-to-film geometry, we have an estimated N of 360 emitters per cavity (Figure 4.14). The estimated average central wavelength of the coupling cavities is found to be 720 nm (1.72 ± 0.01 eV), which matches the emission from the AgInS QDs. The mean losses of the cavities are found to be 177.5 ± 6.5 meV. Although the loss surpasses the coupling strength in general, we can still observe plasmonic mode hybridization, which is usually associated with intermediate or strong plasmon-exciton coupling.

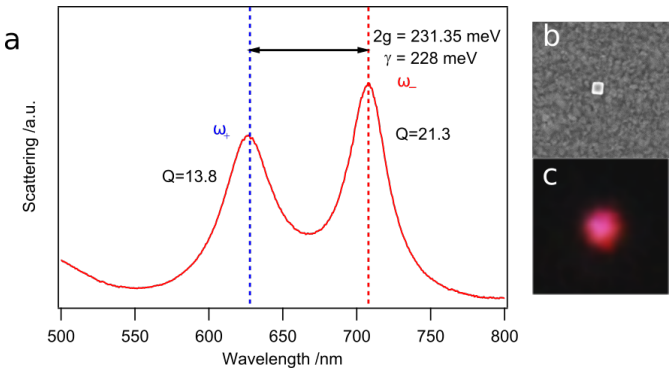

Figure 4.20: a) Scattering spectrum of a silver cube-to-gold film coupled cavity with an embedded AgInS QD monolayer. The insets show this particular cavity in SEM (b) and dark-field scattering microscopy (c).

Latter is defined by 2g>ɣ, which is only the case for several of the detected cavities (Figure 4.20). The statistical evaluation shows that the cavities feature stable condi-

tions concerning their light-matter interactions. Together with the scalable manufacturing process, they can be employed in macroscopic applications in the future.

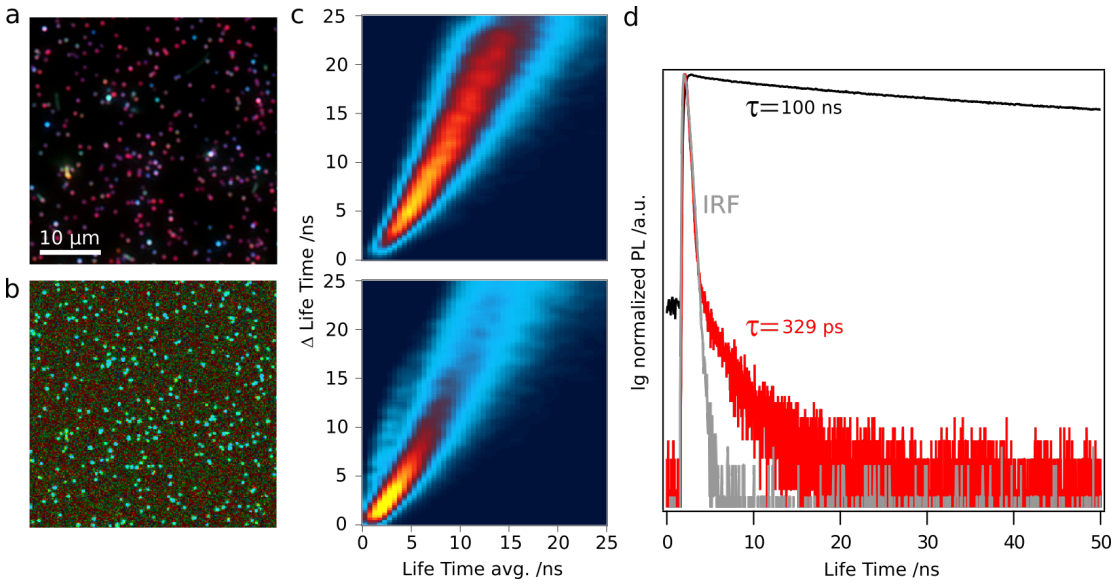

Figure 4.21: Dark-field spectroscopy and time-correlated single photon counting in cube-to-film coupled cavities: (a) Dark-field scattering image of silver cube nanocavities at 9 nm spacing. (b) Fluorescence events (grey scale) and fluorescence lifetime (color scale) image of the corresponding cavities in (a). (c) Lifetime pattern images of quantum dot monolayers without (top) and with (bottom) silver cubes. (d) Normalized photoluminescence (PL) measurements of the ensemble of quantum dots on glass (black) and a single cavity (red). The instrument response function (IRF) is shown in grey.

One of the most promising ways to employ plasmonic cavities is their impact on the emitters' decay channels. Due to the QDs' close proximity to the metal surfaces, the excitable states of the quantum dots are altered, leading to both faster radiative and nonradiative decays. Since the increase in radiative decay rates generally exceeds that of the nonradiative channels, the overall quantum efficiency of the QD emission improves significantly. This gives rise to photoluminescence enhancement, which results in a strong increase in emission. Since the cube-to-film coupled system with 9 nm spacing already showed signatures of strong light-matter interactions, they are once again chosen to be investigated in more detail regarding possible fluorescence enhancement. Figure 4.21a shows a dark-field microscopy image of the cube-to-gold-film-coupled cavities sandwiching the AgInS QD monolayer, verifying the presence of a cube-to-gold-film-coupled nanocavities. Figure 4.21b shows the same area as a FLIM, in which the contrast resembles the photoluminescence intensity and the color indicates the lifetime. A strong increase in the emission intensity can be detected

at each cavity. To quantitatively analyze the photoluminescence enhancement, the enhancement factor (EF) was determined, which is defined as

$$EF = \frac{I_{cav} A_{fit}}{I_{bkg} A_{cav}} \tag{4.4}$$

I_{cav} is the emission intensity of the cavity, I_{bkg} is the intensity of the AgInS QD monolayer outside the cavity, A_{fit} is the area of the enhanced region, and A_{cav} is the estimated area of the cavity. The data were extracted from each cavity by applying a twodimensional Gaussian fit, in which I_{cav} describes the amplitude, I_{bkg} the baseline, and A_{fit} the FWHM of the fit. A_{cav} was assumed to be 75 × 75 nm^2. A statistical evaluation of 100 cavities gives an EF of 1002 ± 48 for the cube-to-gold-film-coupled nanocavities.

For application in devices like optical circuits, it is necessary to modulate the decay rates of the emitters. Since the lifetime is inversely proportional to the decay rate, a decrease is to be expected for plasmonically enhanced fluorescence. TCSPC was employed to further quantify the radiative decay properties of the cavities. While uncoupled AgInS emitters show an estimated average lifetime of 100 ns, the metal-enhanced photoluminescent system shows drastically decreased lifetime of about 330 ps (Figure 4.21d) that is nearly indistinguishable from the instrument response function for most of the measured photons. Both the improved emission and the enhanced exciton decay indicate a strong interaction between plasmonic and excitonic components of the system. To study the macroscopic changes in emission behavior for cube-to-gold film coupled cavities, we employed a lifetime pattern analysis of FLIM measurements which provides information about the general lifetime distributions of a measured surface. Figure 4.21c shows the lifetime pattern of an AgInS QD monolayer on gold without (top) and with (bottom) plasmonic colloids. Although only about 2.5% of the surface is affected by the plasmonic cavities, strong confinement of the lifetime distribution at high decay rates is observed. This shows that these colloidal approach is suitable for large scale modulation of the radiative properties in enhancement and lifetime.

Beyond possible application in optical computing, plasmonic cavities are also highly sensitive to changes in their environments. Therefore, their optical response can be further altered by changing parameters like the ambient refractive index (RI). To study

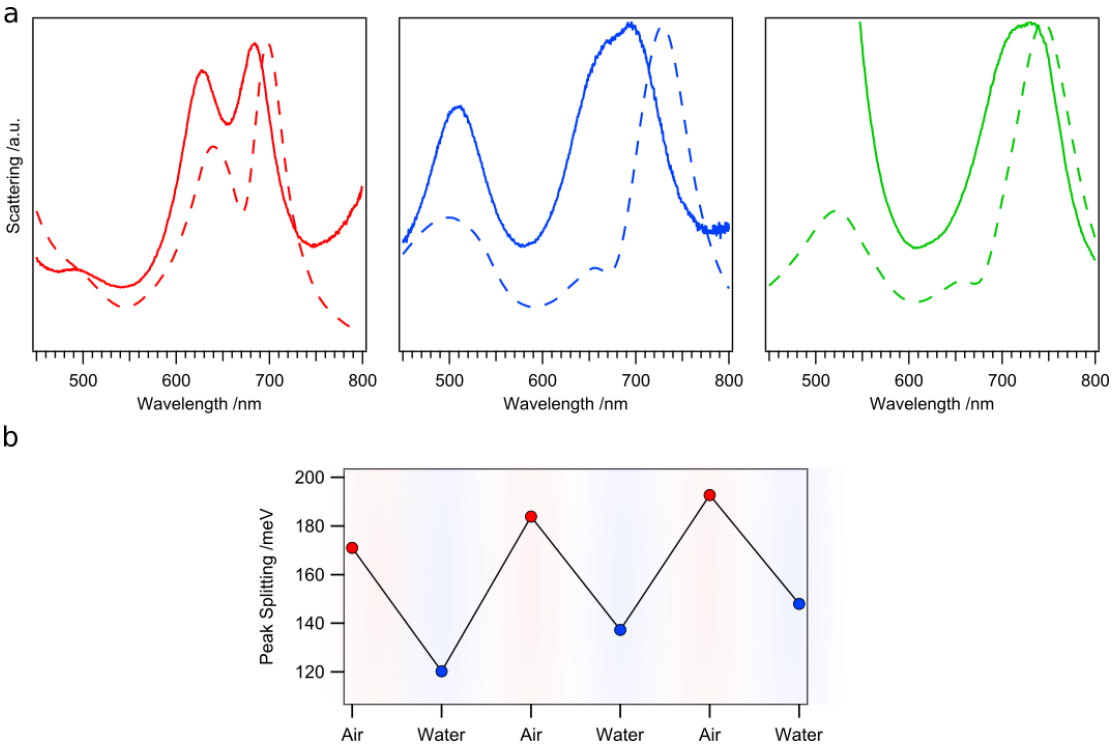

Figure 4.22: Cyclical change in the refractive index environment: (a) measured (solid lines) and simulated (dashed lines) scattering responses of a nanocavity in different dielectric media, including air (red), water (blue), and ethylene glycol (green). (b) Reversible switching of plasmon mode hybridization by alternating the environment.

how the light-matter interactions respond when the cavity resonance is changed, the dielectric environment of the system is varied from air (n=1) to water (n=1.33) and to ethylene glycol (n=1.43). Figure 4.22a shows the scattering signals for these different ambient conditions, both in experiments and simulations. While pronounced splitting is observed in air, reduced splitting is observed if the surrounding medium is changed to water or ethylene glycol. If a sample is immersed in water and dried afterwards, the original peak splitting is recovered. As it is plotted in Figure 4.22b, this RI modulation can be cycled.

Conclusion

The ability to tailor light-matter interactions on a sub-wavelength scale was demonstrated for a set of nanocavities using spectroscopic and electromagnetic simulation methods. To ensure cost-effective fabrication on large scale, a self-assembled monolayer of thiolates and polyelectrolytes were employed to tailor the cavity proper-

ties. This method allowed to statistically quantify the spectroscopic properties of the colloid-to-film coupled cavities with and without embedded emitters and could be extended to create different emitter densities by using varying thiolates in the future. The resonance position and shape could be adjusted over a wide visible spectral range by introducing different colloidal materials, shapes and cavity spacings. The plasmon-exciton interaction, as a measure of the coupling strength, was confirmed by scattering spectroscopy, fluorescence lifetime measurements and reversible refractive index sensing. The accurate determination of optical properties is an important step in the design of photonic nanostructures. The low-cost and scalable fabrication of tailor-made nanocavities can therefore lead to new generations of optical circuits and light modulators.

4.4 Self-Assembled Semiconductor Nanocrystals on Macroscopic Scale

Colloidal quantum dots are semiconductor nanoparticles that inhibit unique optical properties due to quantum confinement of the excited electrons.[73] They can be processed on large scale with low-cost methods[132,133] and have already been employed for optoelectronic applications like photodetectors[134], light harvesting[135] or displays[136]. Their application in macroscopic devices is yet restricted due to losses in brightness resulting from internal reflection and reabsorption of emitted photons.[137] These obstacles can be overcome by assembling colloidal QDs in optical gratings.[138,139] The diffraction modes inherent to these structures can be coupled to the single building blocks, which can be exploited for optoelectric functionalities like coherent emission.[140,141] A promising method to fabricate ordered macrostructures made from colloidal building blocks is Template-Assisted Self-Assembly (TASA), where the particles are arranged in a predetermined way through the capillary flow of the respective particle solution in nanopatterned structures.[142,143] This single-step method can produce defined particle arrays on large scale and is therefore a suitable method for manufacturing optical gratings consisting of colloidal QDs.[144,145][FG3]

This section shows how rapid prototyping involving LIL and Soft Lithography is used to manufacture elastic optical gratings with adjustable periodicities. These polymer stamps are then employed for TASA of colloidal CdTe QDs in defined structures on cm^2. The QD gratings are analysed regarding their spatial and optical properties using SEM, AFM, FLIM and UV-vis. The printing process is furthermore applied on substrates containing singlecrystalline goldflakes to obtain alternating emission properties and to demonstrate the stability of the printing process.

The colloidal CdTe QDs and their spectroscopic measurements were provided from Vladimir Lesnyak from the group of Prof. Alexander Eychmüller, TU Dresden.

Additional UV-Vis reflectance measurements were done by Olha Aftenieva, Leibniz-Institut für Polymerforschung e.V., Dresden

Results and Discussion

The first step for TASA of CdTe semiconductor nanocrystals is the manufacturing of master gratings. LIL was chosen since this mask-free lithography method can generate defined nanopatterns in short time with low costs, which are crucial qualities for applying nanostructures on large scale.[146,147] This is achieved by having two coherent laser beams overlapping in specific angles, which results in interference between both beams. The periodicity of the interference patterns can be described with Bragg's law:[148]

$$P = \frac{\lambda}{2sin(\theta)} \tag{4.5}$$

P is the period of the resulting grating, λ the Laser wavelength and θ the angle in which both beams are interfering. The interference pattern can be imprinted to a thin layer of photoresist and developed afterwards. The employed He-Cd Laser with 325 nm emission wavelength incorporated in an optical LIL setup is depicted in figure 4.23.

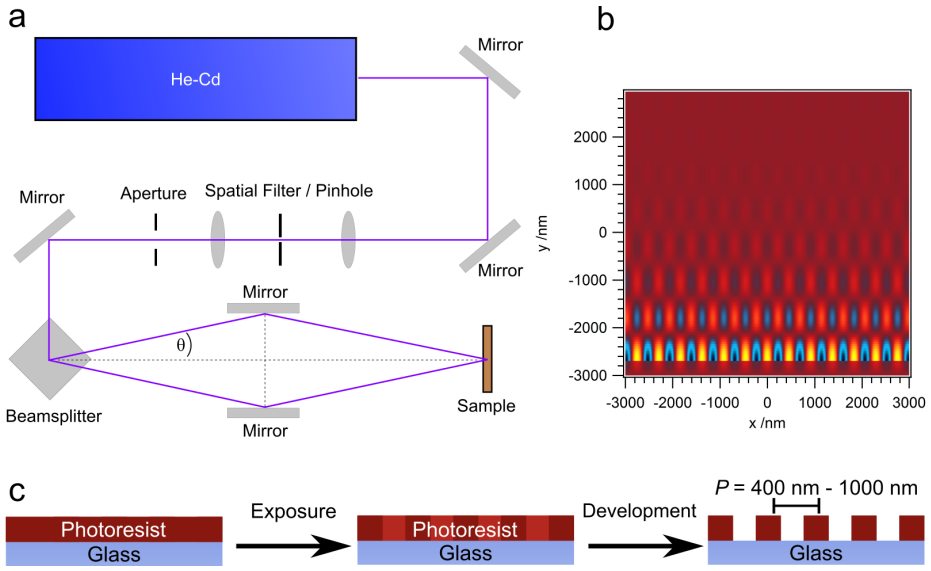

Figure 4.23: (a) Sketch of the LIL setup built during the scope of this thesis featuring a He-Cd Laser operating with λ=325 nm. (b) FDTD simulated interference pattern of two light waves interfering with each other with θ=45 °. (c) Schematic illustration of the sample fabrication for LIL nanostructures.

The LIL-fabricated structures are then employed for Soft Lithography, which makes it possible to transfer nanosized patterns in elastic polymers.[149] Since common elastomers like PDMS can't reproduce the small feature sizes below 500 nm properly,

h-PDMS is used for replicating the respective master substrates.[150]

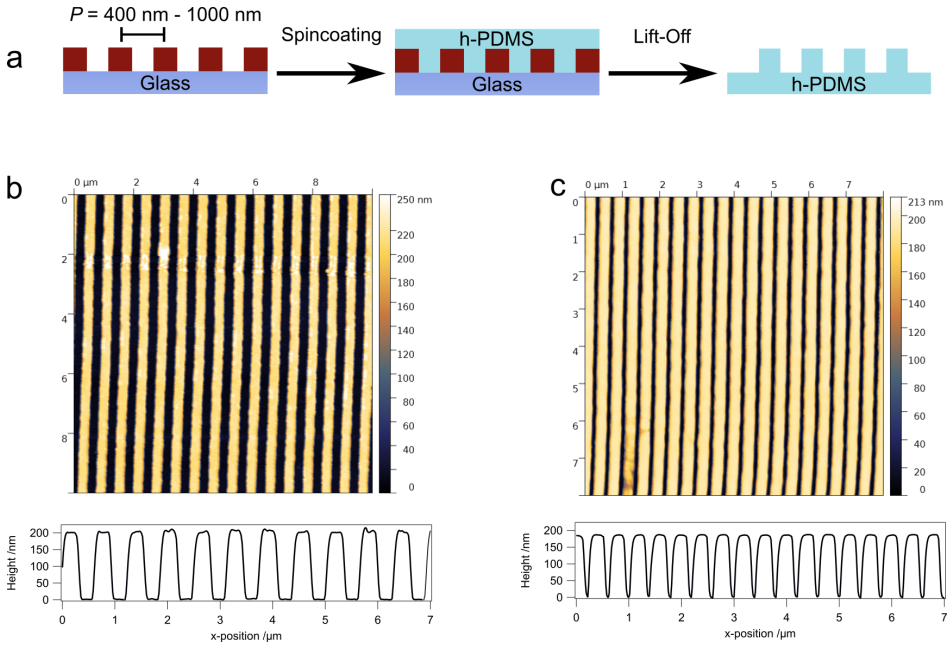

Figure 4.24: Template manufacturing for Template-Assisted Self-Assembly: (a) Schematic illustration of structure transfer from a LIL master into h-PDMS. (b) AFM measurement and profile of a LIL manufactured master substrate. (c) AFM measurement and profile of the h-PDMS mold of the original structure.

This process is shown exemplary in figure 4.24, where a LIL-fabricated line pattern with approximately 600 nm periodicity and the respective h-PDMS mold are characterized using AFM. The measurements show that the patterns are well replicated concerning the periodicity and the height of about 200 nm.

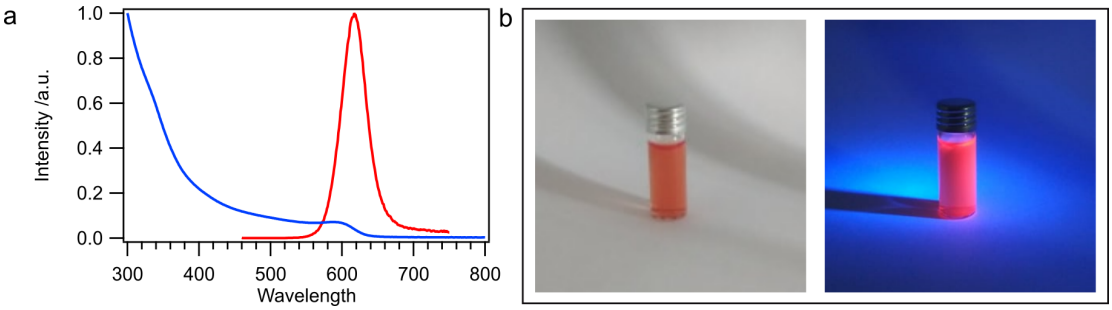

Figure 4.25: Colloidal CdTe QDs: (a) Extinction (blue line) and emission (red line) of TGA-capped CdTe Quantum Dots in aqueous solution. (b) Photograph of a solution of colloidal CdTe QDs in water with white light (left) and UV light (right) exposure.

TGA-capped colloidal CdTe QDs are used as colloidal building blocks for TASA of optical gratings. Besides their availability in aqueous solution, they feature a narrow

emission peak at 617 nm with a FWHM of 25.9 nm (figure 4.25), which lies in the domain of available grid constants that can be manufactured with the present LIL system. This is important as the overall goal is to match the emission wavelength and the grid constant to induce coupling between both components. For the proof of concept, a line pattern with 860 nm periodicity is employed for better resolution in optical characterization methods.

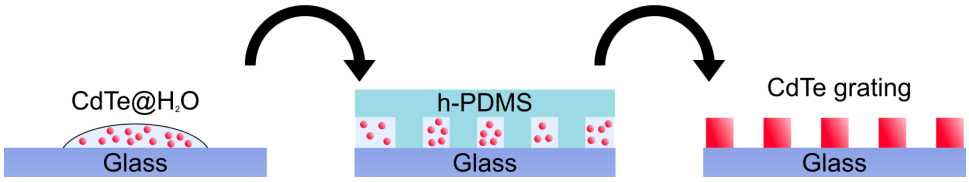

Figure 4.26: Fabrication of semiconductor nanocrystal gratings: Aqueous QD solution is dropped onto a glass substrate. The nanopatterned PDMS stamp is applied und guides the liquid into its cavities. After drying and PDMS stamp removal, confined CdTe QD lines are obtained.

The TASA is carried out by placing a drop of the QD particle solution onto a glass substrate and then applying the Soft Lithography-fabricated h-PDMS stamp onto it. The capillary forces adhere the stamp to the substrate surface and the QD solution flows into the cavities of the line pattern. After drying over night, well defined gratings made from CdTe QDs are obtained (figure 4.26).

The resulting structures is characterized using complementary surface characterization methods. FLIM measurements of the QD line pattern (figure 4.27a) show defined photoluminescent lines with homogeneous emission and lifetime over the whole detected area, which suggests uniform packing of the assembled colloids. This is further validated with AFM and SEM (figure 4.27b+c), where defined gratings can be observed. Since tunable diffraction orders that arise in optical gratings are of high interest for possible coupling to the emitters, a lower periodicity of 560 nm is fabricated and angle dependent UV-Vis measurements on the resulting CdTe QD grating are employed to quantify the macroscopic diffraction properties.

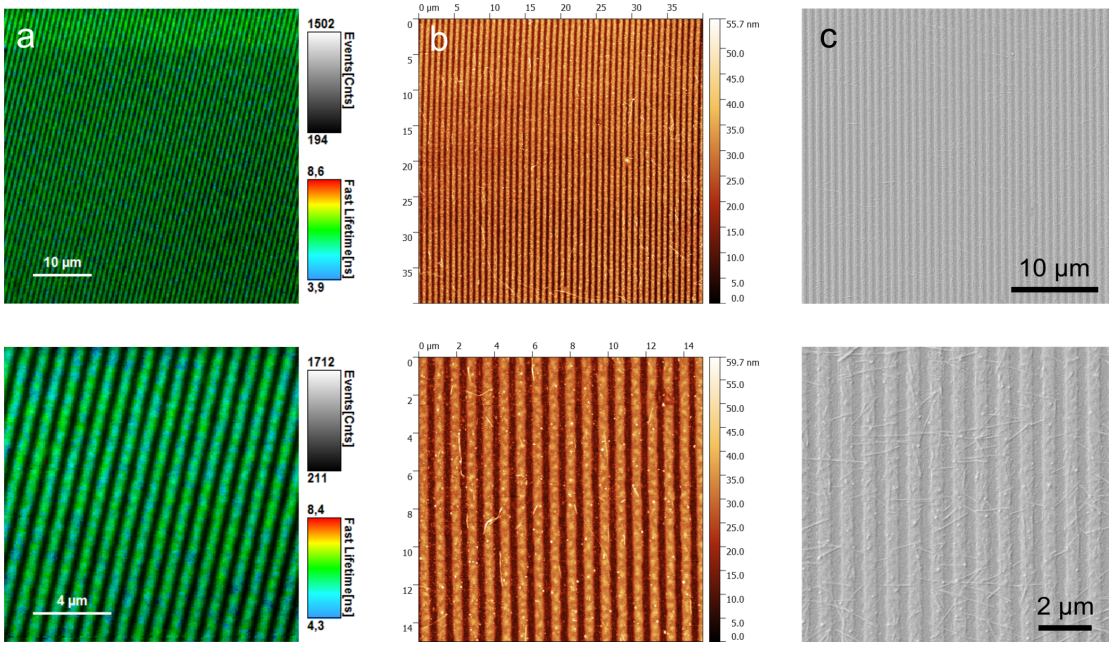

Figure 4.27: Characterization of TASA-fabricated CdTe QD gratings.(a) FLIM measurements of a CdTe lattice. (b) AFM measurements of the assembled QD lines. (c) SEM pictures of the QD Lines.

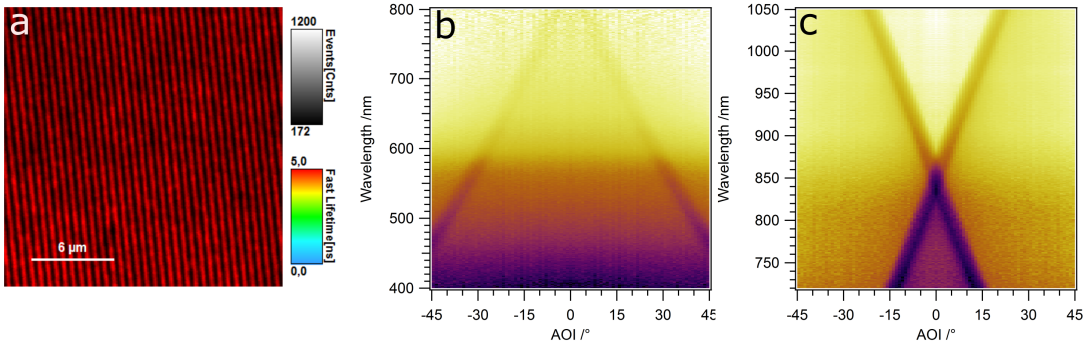

Figure 4.28: Diffraction of self-assembled CdTe gratings: (a) FLIM measurement of a CdTe QD grating with 560 nm periodicity on a glass substrate. (b+c) Angle dependant UV-Vis measurements of the respective QD grating.

The resulting dispersion measurement (figure 4.28) reveals first order Rayleigh anomalies with a crossing at 851 nm, which corresponds to the periodicity of the grating (560 nm) and the refractive index of the medium, in this case glass (n = 1.52).

Applying emitters on plasmonic mirrors can lead to enhanced coherent energy transfer due to coupling of the emission to the SPR of the metal film.[151] The surface roughness of a respective metal surface directly affects the optical properties of electromagnetic coupling.[108] In order to obtain smooth metallic surfaces, single-

crystalline gold plates are synthesized using a bottom-up wet-chemical reduction of $HAuCl_4$ as reported in literature.[152]

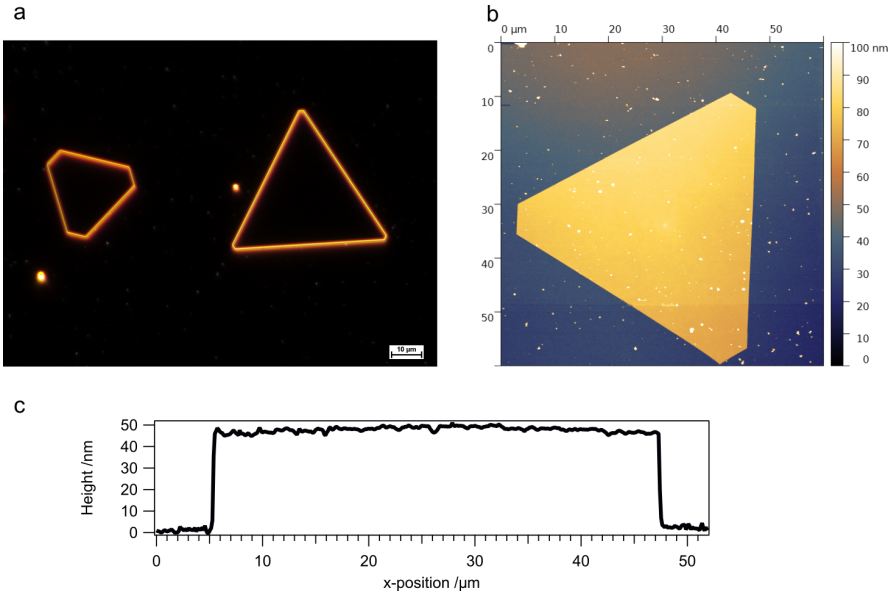

Figure 4.29: Single-crystalline gold microplates: (a) Dark-field image of gold flakes synthesized on a glass substrate. (b+c) AFM measurement of an exemplary gold crystal and a respective profile plot, showing the uniform thickness on large lateral dimensions.

Dark-field imaging and AFM mapping of the as synthesized gold plates (figure 4.29) show the presence of gold crystals with lateral dimensions of up to 50 µm and a uniform height of 50 nm. Furthermore, the absence of scattering featured in the dark-field and the AFM scan of the gold plate surface show remarkable smoothness and steep edges of the obtained gold flakes.

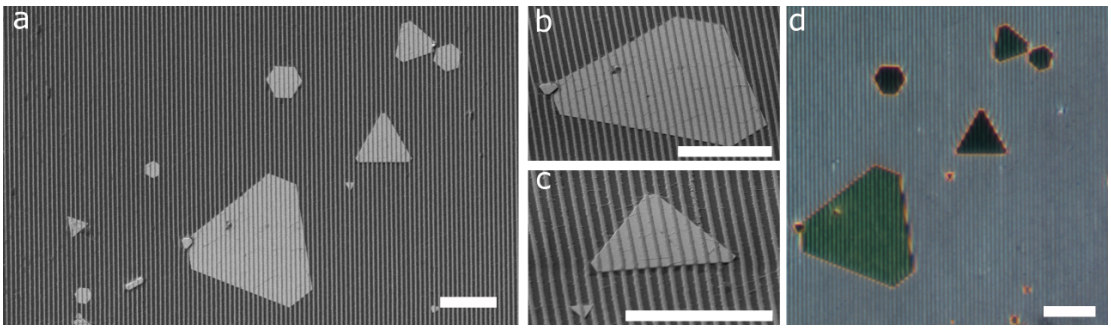

Figure 4.30: TASA fabricated CdTe QD lines printed on gold crystals: (a-c) SEM images of the grid printing on single crystalline gold plates. Scale is 10 µm. (d) Dark-field image of the area shown in the SEM images.

The TASA of CdTe QDs is now employed to print respective particle lines onto a

glass substrate containing single-crystalline gold microplates to induce interactions between the emission and the gold surface. SEM and dark-field imaging are used to validate if the macroscopic assembly process is affected by the different height and surface chemistry of the gold plates on the substrate. Figure 4.30 shows a continuously uniform grating formation over the respective gold plates as well as the glass substrate. A single microplate covered with a QD grating is now studied in detail regarding its spatial properties and photoluminescence.

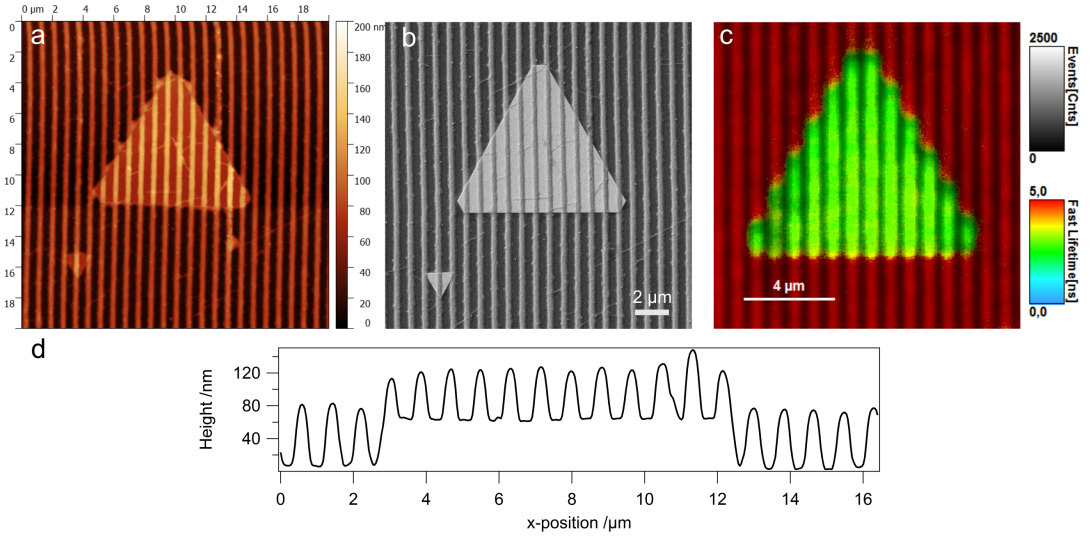

Figure 4.31: CdTe QD Lines on a monocrystalline gold microplate: (a+d) AFM measurement and profile of QD lines printed onto the gold crystal. (b) SEM image of the structure. (c) FLIM measurement of the same gold microplate covered with a QD grating.

The AFM image and profile plot as well as the SEM measurement (figure 4.31 a,b,d) show that the uniform line shape of the TASA-fabricated QD gratings is persistent on both surface materials as well as on the edges of the gold plate. It has yet to be noted that the height of the assembled QD lines is lower on top of the gold structure (40 nm) than on the bare substrate (70 nm), which could be caused by compression of the elastic mold by the gold crystals. This compression might affect the capillary flow of the QD solution and therefore decrease the absolute height of the gratings. The FLIM data shown in figure 4.31c illustrate the interaction between the emission of the CdTe QD lines and the gold surface. Although the overall intensity of the photoluminescence is conserved on the gold plate, the detected fluorescence lifetime is reduced significantly. Since optoelectronic applications like optical circuits require nanomaterials with tailored light-matter interactions on the lateral dimension[153], uniform TASA-fabricated

QD gratings on substrates with alternating optical properties are now available for large-scale application.

Conclusion

It was shown how a combination of LIL and Soft Lithography can be employed to efficiently manufacture optical line gratings with variable periodicity on cm^2 scope which can then be transferred into elastic materials. These molds were then used for TASA of colloidal CdTe QDs, which resulted in periodic arrays of emitter lines on macroscopic scale. Optical and mechanical surface characterization methods like dark-field imaging, AFM and FLIM proved great uniformity regarding the structural and photoluminescence properties of the obtained QD lines. Angle dependent UV-Vis spectroscopy could validate the presence of pronounced Bragg refraction modes inherent to the colloidally assembled gratings. Atomically flat gold microplates with high aspect ratios were then synthesized and printed with QD lines in order to modulate the emission properties of applied QD gratings and demonstrate the robustness of the TASA process. The low-cost and high-throughput assembly of colloidal QDs into macroscopic structures allows tunable grating constants for coupling of the emitters to the refraction modes of the grating or to the SPR of metallic nanostructures.

Chapter

5 Conclusion

This thesis approached the generation of coherent energy transfer on nanoscale using colloidal methods. Bottom-up self-assembly techniques were employed to fabricate different functional systems and correlated characterization methods together with electromagnetic simulations were carried out to study them in detail. The main focus was put on colloidal particle-to-film coupled cavities, that allow high control of the spatial features and the resulting optical properties. A gold sphere-to-gold film coupled system was chosen to theoretically study how colloidally accessible parameters affect the optical response of the cavity with nanometer precision. Further simulations on resonant dipole sources at different positions in regard to the cavity showed that the radiative and nonradiative decay rates of the emitter are crucially dependent on the absolute position and orientation in the electromagnetic field induced by the cavity. The simulations further showed how the QE of a cavity-coupled emitter is enhanced by orders of magnitude. A gold sphere-to-gold film coupled cavity was then realized with fluorescent dye-loaded hectorites as dielectric spacer and matrix for embedded emitters. Simple drop casting techniques allowed the fabrication of defined NPoM-type cavities on large scale that were characterized with complementary topographical and optical detection methods. Hybridized cavity modes and fluorescence enhancement indicated the presence of coherent light-matter interactions in the system, but the short lifetimes of the emitters allowed no quantitative evaluation on the decay processes of the cavity-coupled fluorophores. This led to the next system, where gold spheres and silver cubes were used as plasmonic colloids. In combination with thiolate SAMs and layer-by-layer assembly of polyelectrolyte multilayers, a tunable method for large scale assembling of NPoM cavities was introduced. AgInS

broadband emitters were incorporated into the cavity by electrostatically driven random sequential adsorption, which resulted in densely packed monolayers. For the silver cube-to-film coupled cavity geometry with sub 10 nm particle-to-film distance, mixed light-matter states were detected as well as large enhancement of the fluorescence intensity and the radiative decay rate, which allowed statistical evaluations on the plasmon-exciton interactions arising in the cavity. The results showed how plasmonic and semiconductive colloids can be assembled to induce strong light-matter interactions in the intermediate to strong coupling regime.

Instead of using plasmon resonances to enhance the photoluminescence properties of emitters like colloidal QDs, another approach for coherent optical structures was introduced where semiconductor nanocrystals were assembled into macroscopic superstructures with defined diffraction properties. This was achieved by combining LIL and Soft Lithography to fabricate optical gratings in elastic stamps on cm^2 scope, that were then employed to assemble the QDs into gratings from solution. This TASA process resulted in defined optical gratings composed by colloidal QDs on large scale, that were thoroughly characterized in regard to structural and optical quality. Modulated emission properties and stable printing were demonstrated by assembling the grating onto wet-chemically synthesized single crystalline gold microplates. Intense Rayleigh anomalies were furthermore detected and proved the presence of diffraction orders that can be coupled to the QDs for coherent energy transfer in future works.

This work showed how colloidal building blocks in combination with bottom-up self-assembly techniques can be employed to create functional nanostructures with precisely tunable properties in an efficient, low-cost and scalable fashion. It furthermore proved that colloidal methods can be a relevant tool on the way to large scale manufacturing of elaborated optoelectronic applications like nanolasers, sensing on single molecule level or optical circuits.

Zusammenfassung

Diese Arbeit befasste sich mit dem Erzeugen kohärenten Energetransfers auf Nanoebene mittels kolloidaler Methodiken. Verschiedene funktionale Systeme wurden mittels Selbstassemblierung gefertigt und korrelierte Charakterisierungsmethoden sowie elektromagnetische Simulationen wurden genutzt um diese detailliert zu untersuchen. Der Hauptfokus lag auf kolloidalen Partikel-auf-Film gekoppelten Kavitäten, da diese hohe Kontrolle über die strukturellen und optischen Eigenschaften der Struktur erlauben. Ein Goldsphäre-auf-Goldfilm gekoppeltes System wurde mittels Simulationen daraufhin untersucht, wie dessen optische Eigenschaften durch kolloidal zugängliche Methoden mit Nanometer-Präzision gesteuert werden können. Weitere Simulationen mit resonanten Dipolquellen, die an verschiedene Positionen im Verhältnis zur Kavität gesetzt wurden, zeigten dass die strahlenden und nichtstrahlenden Zerfallsraten der Emitter stark von dessen räumlicher Position und Orientierung im elektromagnetischen Feld der Kavität abhängen. Die Simulationen zeigten ebenfalls dass die Quanteneffizienz eines Kavität-gekoppelten Emitters um Größenordnungen erhöht wird. Anschließend wurde eine Goldsphäre-auf-Goldfilm-gekoppelte Kavität realisiert, in der fluoreszente Hectorite sowohl als dielektrischer Abstandshalter und Matrix für die eingelagerten Emitter dient. Einfaches Dropcasting erlaubte die Herstellung definierter NPoM Kavitäten auf großem Maßstab, die anschließend mit sich ergänzenden topographischen und optischen Methoden untersucht wurden. Hybridisierte Kavitätsmoden und Fluoreszenzverstärkung deuteten auf die Gegenwart kohärenter Licht-Materie-Wechselwirkungen im System hin, jedoch verhinderte die kurze Lebenszeit der verwendeten Fluorophore eine quantitative Untersuchung von deren Zerfallsprozessen. Dies führte zum nächsten System, bei dem Goldsphären und Silberwürfel als plasmonische Kolloide verwendet wurden. In Verbindung mit Thiol-SAMs und Layer-by-Layer Auftragung von Polyelektrolyt-Multilagen wurde eine einstellbare Methode

zur großflächigen Assemblierung von NPoM Kavitäten erarbeitet. AgInS Breitbandemitter wurden mittels elektrostatisch getriebener Adsorption, die zu geschlossenen Monolagen führte, in die Kavitäten eingebaut. Für die Silberwürfel-auf-Film gekoppelte Kavitätsgeometrie mit weniger als 10 nm Partikel-zu-Film Abstand wurden hybridisierte Licht-Materie Zustände sowie eine starke Erhöhung der Fluoreszenzintensität und strahlenden Zerfallsraten gemessen, was es möglich machte diese Eigenschaften statistisch zu untersuchen. Die Ergebnisse zeigen wie plasmonische und halbleitende Kolloide angeordnet werden können um starke Licht-Materie Wechselwirkungen im intermediate coupling und strong coupling Bereich zu erzeugen.

Anstatt Plasmonresonanzen zu nutzen um die Photolumineszenz von Emittern (wie kolloidalen Quantenpunkten) zu verbessern wurde ein weiterer Vorstoß für Kohärenz in optischen aktiven Strukturen vorgestellt, bei dem halbleitende Nanokristalle in makroskopische Superstrukturen mit definierter Diffraktion angeordnet wurden. Dafür wurden mittels Kombination aus LIL und Soft Lithography optische Gitter in elastischen Polymeren auf cm^2 Ebene hergestellt, mit denen anschließend die Quantenpunkte aus wässriger Lösung in Gitter angeordnet wurden. Dieser TASA Ansatz führte zu definierten optischen Gittern aus kolloidalen Quantenpunkten, die ausgiebig bezüglich ihrer strukturellen und optischen Eigenschaften untersucht wurden. Schaltbare Emission und die robuste Assemblierung wurden demonstriert indem die Gitter auf nasschemisch synthetisierten, einkristallinen Goldplättchen gedruckt wurden. Desweiteren zeigten intensive Rayleigh-Anomalien die Gegenwart von Diffraktionsordnungen in der Struktur, die künftig mit den Emittern gekoppelt werden können um kohärenten Energietransfer zu erzeugen.

Zusammenfassend zeigte diese Arbeit, wie kolloidale Bausteine in Verbindung mit nasschemischer Selbstassemblierung verwendet werden können um funktionale Nanostrukturen mit präsize einstellbaren Eigenschaften auf effiziente, kostengünstige und skalierbare Weise herzustellen. Damit wurde gezeigt dass kolloidale Methoden sich als relevantes Werkzeug für die großflächige Herstellung von optoelektronischen Anwendungen wie Nanolasern, Einzelmolekül-Sensoren und optischen Schaltkreisen erweisen könnten.

List of Publications

[18] *Single Particle Spectroscopy of Radiative Processes in Colloid-to-Film-Coupled Nanoantennas*
M. J. Schnepf, Y. Brasse, F. R. Goßler, A. M. Steiner, J. Obermeier, M. Lippitz, A. Fery and T. A. F. König, Zeitschrift für Physikalische Chemie **2018**, 232(9-11), 1593-1606.

[118] *Fluorescent Sulphur- and Nitrogen-Containing Porous Polymers with Tuneable Donor–Acceptor Domains for Light-Driven Hydrogen Evolution*
D. Schwarz, A. Acharja, A. Ichangi, P. Lyu, M. V. Opanasenko, F. R. Goßler, T. A. F. König, J. Čejka, P. Nachtigall, A. Thomas, M. J. Bojdys, Chem. Eur. J. **2018**, 24, 11916

[17] *Active Plasmonic Colloid-to-Film-Coupled Cavities for Tailored Light–Matter Interactions*
F. R. Goßler, A. M. Steiner, O. Stroyuk, A. Raevskaya, and T. A. F. König The Journal of Physical Chemistry C **2019**, 123, (11), 6745-6752

[154] *Mechanotunable Surface Lattice Resonances in the Visible Optical Range by Soft Lithography Templates and Directed Self-Assembly*
V. Gupta, P. T. Probst, F. R. Goßler, A. M. Steiner, J. Schubert, Y. Brasse, T. A. F. König, and A. Fery ACS Applied Materials & Interfaces **2019**, 11, (31), 28189-28196

Kapitel 6

Acknowledgments

I want to thank my supervisor Dr. Tobias König for granting me the chance to do this work in a young, familiar group and for his support. I also want to thank Prof. Andreas Fery, Prof. Alexander Eychmüller and Vladimir Lesnyak for the fruitful cooperations and discussions. Thanks to my co-workers and cooperation partners, most notably Martin Mayer, Max Schnepf, Anja Steiner, Yannic Brassé, Vaibhav Gupta, Olha Aftenieva and Oleksandr Stroyuk.

Thanks to Michael Göbel and Petr Formanek for their help and introduction to electron microscopy and their support.

I also want to thank my family, my friends and Hui-Tzu Chen for the love and the joy they bring to my life and for the support they provide.

Thanks to the rocketbeans!

Thanks to all members of Outcast on Noggenfogger. Exploring Azeroth with you guys was a splendid experience.

I furthermore want to thank Charlene Ng and Ken Harris for additional proof reading.

Kapitel 7

Appendix

7.1 Gold Triangle-based Open Cavity Design

Introduction

Plasmonic particles coupled to emitters are referred to as open cavities.[84] If they feature sufficiently strong field enhancement, they are able to couple with the photoluminescent material like already shown for NPoM type cavities. This preliminary work shows how gold nanotriangles are explored concerning their plasmonic mode structures and field enhancement.

The elelctron energy loss spectroscopy (EELS) was done by Dr. Pavel Potapov from the group of Dr. Axel Lubk, Leibniz-Institut für Festkörper- und Werkstoffforschung Dresden.

The gold nanotriangles were synthesized and additional electromagnetic simulations were carried out by Martin Mayer from the group of Prof. Andreas Fery, Leibniz-Institut für Polymerforschung e.V., Dresden

Results and Discussion

For a detailed characterization of the optical properties and the enhanced fields of the gold nanotriangles, transmission electron microscopy (TEM), EELS, dark-field scattering and electromagnetic simulations are employed.

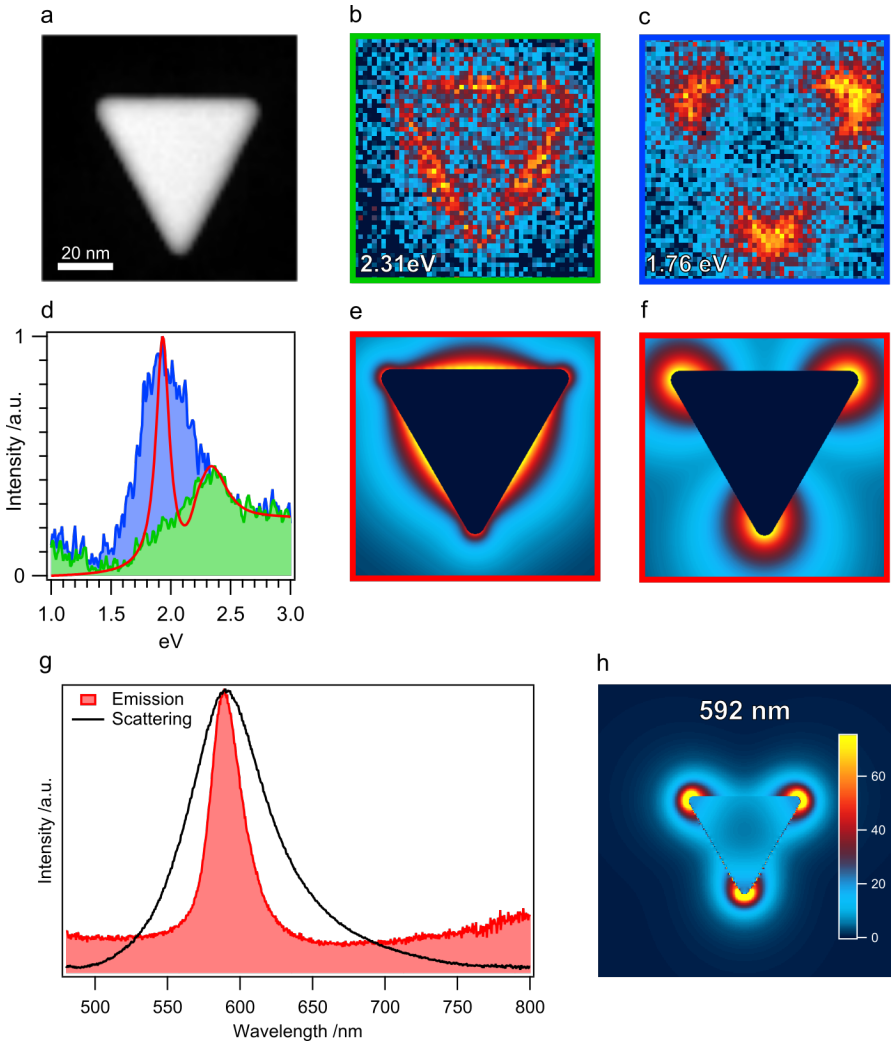

Abbildung 7.1: Mode analysis of colloidal gold nano triangles. (a) shows a TEM image of a selected AuNT, (b) and (c) EELS measurements to picture the confined modes of the particle.(d-f) EELS spectrum (simulated and measured) and EELS simulations showing the same modes. (g) shows a scattering spectrum of such a AuNT (black line) and the red curve shows a matching CdSe quantum platelet. (h) shows an FDTD simulation of the excited fields of a AuNT.

The TEM picture (figure 7.1a) and EELS measurements on the same particle (figure 7.1b+c) show two modes with field enhancements at the vertices (2.31 meV) and the edges (1.76 meV) and are well matched by additional EELS simulations (figure 7.1d-f). Dark-field scattering spectroscopyof a single nanotriangle shows LSPR at 592 nm, which shows perfect overlap with CdSe quantum platelets that are chosen for emitters for future coupling of both specimen (figure 7.1g). The simulated field enhancement of this mode at the edges is displayed in figure 7.1h. These high field enhancement makes the gold nanotriangles suitable colloids for designing plasmonic open cavities.

Conclusion

Further experimental efforts are needed to create an open cavity with colloidal gold nanotriangles coupled to quantum platelets. The preliminary work on this system yet show great potential due to well defined field enhancement and spectral overlap between plasmonic resonance and the PL of the emitter.

7.2 Theoretical Investigation on Cube-to-Gold Film coupled NPoM Cavities

Introduction

The NPoM cavities with 75 nm silver cubes as plasmonic colloids were thoroughly discussed in the main part of this work. This section gives additional simulation data for further insights into the optical properties inherent to this type of cavity.

Results and Discussion

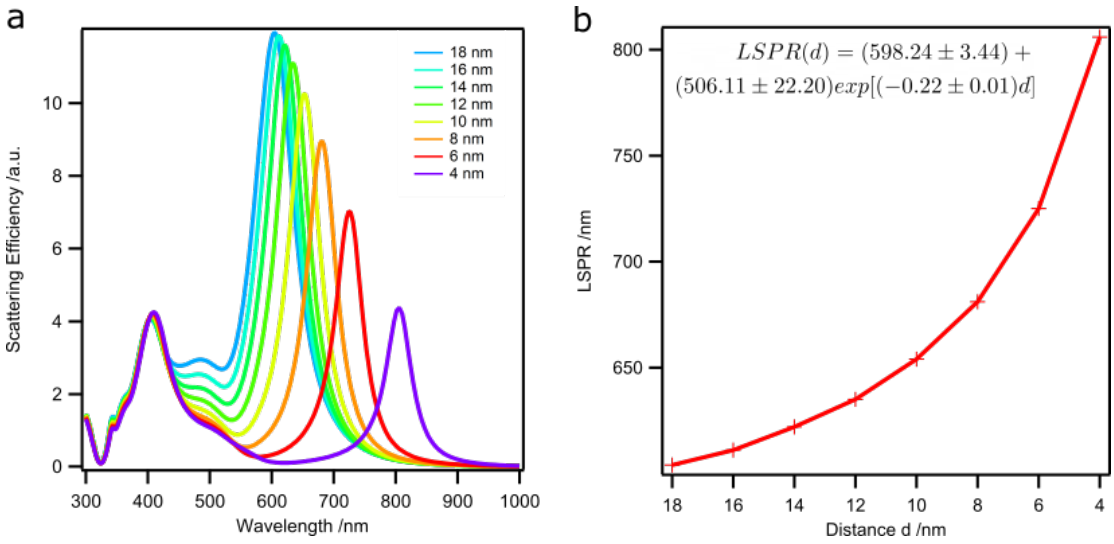

Abbildung 7.2: FDTD simulations of a 75 nm silver cube approaching a plasmonic gold film. Calculated scattering spectra (a) were normalized to the cube face area (75 nm·75 nm). The sensitivity (LSPR as a function of the cavity gapsize) is extracted from the scattering spectra and show a strongly exponential shift of the LSPR (b).

Fig 7.2 shows the simulated scattering spectra of cube-to-gold film coupled cavities with varying spacing to determine the sensitivity of the plasmon resonance. A exponential increase of the LSPR occurs if the particle-to-film distance is decreased.

7.3 Scripts Used for Analytical Models

Script used for simulating different coupling regimes for the polaritons shown in figure 3.10 using Lumerical Script Language:

```
lam=300:2:900; #wavelength
energy=1240/lam; #eV
freq=c/lam*1e9; #omega
omega=2*pi*freq; #omega_circ
w_pl=2.1; #plasmon resonance
w_em=2.1; #emission resonance
y_pl=0.24; #plasmonic loss factor
y_em=0.09; #exciton loss factor
a=2; #coupling factor
g=a*y_pl; #coupling strength

label="Splitting_sim_g_"+num2str(a)+".txt";

lam_pl=1240/w_pl;
lam_em=1240/w_em;
lam_y_em=1240/y_em;
lam_y_pl=1240/y_pl;



f_pl=c/lam_pl;
f_em=c/lam_em;
f_y_pl=c/lam_y_pl;
f_y_em=c/lam_y_em;

omega_pl=2*pi*f_pl;
omega_em=2*pi*f_em;
omega_y_pl=2*pi*f_y_pl;
omega_y_em=2*pi*f_y_em;



mu_pl=(w_em^2-energy^2-1i*energy*y_em)/
((w_em^2-energy^2-1i*energy*y_em)*(w_pl^2-energy^2
-1i*energy*y_pl)-w_em*w_pl*g^2);
sigma_scat=energy^4*abs(mu_pl)^2;
```

Scripts used to plot the theoretical electron confinements in figure 3.8 using Lumerical Script Language:

```
## Teilchens im Kasten
label="particle_box";
label2="Brus_CdTe";
##define constants
m0=9.1093837015*1e-31; ## Mass /kg
e0=1.602e-19; ## Elementary charge: 1eV=e*1V=1.602e-19
hJs=6.62607015*1e-34; ## Planck constant /J*s
 define parameters
r=-3.6:0.1:3.6; ## Skala /nm
n=1:3;
rs=r*1e-9;
En=matrix(length(r),length(n));
for(j=1:length(n)){
En(1:length(r),j)=(hJs^2*n(j)^2)/(8*m0*(rs/2)^2); ## /J

Ene=En/e0; ## /eV
plot(r,Ene(1:length(r),1:length(n)),"Länge /nm","Energy /eV",label);
setplot("y max",6);
data_all=[r,Ene];
write(label+".txt",num2str(data_all));

## Brus Formel CdTe

## define parameters
Egap=1.606; ## band gap for CdTe 1.606 eV
mes=0.096*m0;
mhs=0.4*m0;
eps=7.1; ## dielectric constant CdTe
r=1:0.05:10; ## Skala /nm
dE1=Egap*r/r*e0; ## /eV
dE1e=Egap*r/r; ## /eV
dE2=hJs^2/(8*(r*1e-9)^2)*(1/mes+1/mhs); ## /J
dE2e=dE2/e0; ## /eV
## eigene Fortführung mit originaler Formel
E_eps=(1.8*e0^2)/(4*pi*eps0*eps*(r*1e-9));
E_CdTe=((hbar^2*pi^2)/(2*(r*1e-9)^2))*(1/mes+1/mhs);
```

```
E_CdTe_e=E_CdTe/e0;
E_Brus=Egap+(E_CdTe/e0)-E_eps;
data_Brus=[r,E_Brus,dE1e];

plot(r,E_Brus,dE1e,"Radius /nm","Energy /eV");
write(label2+".txt",num2str(data_Brus));
```

Script used to calculate and extract the interference patterns for LIL, here with 325 nm excitation wavelength and 45 ° angle between both waves.

```
# Simulation with source at x degrees:
label="45deg_s_pol";
switchtolayout;

setnamed("source45deg","enabled",1);
setnamed("source -45deg","enabled",0);

run;

E_45 = getresult("monitor_1","E");
Ez_45=pinch(E_45.Ez);

x = E_45.x/1e-6;
y = E_45.y/1e-6;

image(x,y,Ez_45,"x (microns)","y (microns)","E_z for source @ 45deg");


# Simulation with source at -45 degrees:

switchtolayout;

setnamed("source45deg","enabled",0);
setnamed("source -45deg","enabled",1);

run;

E_m45 = getresult("monitor_1","E");
Ez_m45=pinch(E_m45.Ez);
image(x,y,Ez_m45,"x (microns)","y (microns)","E_z for source @ -45deg");
```

```
# Coherent sum (CORRECT)

Enet = Ez_m45+Ez_45;
image(x,y,Enet,"x (microns)","y (microns)","E_z for sources @
45 and -45deg (CORRECT)");
write(label+".txt",num2str(Enet));
```

References

[1] A. N. Oraevsky, Whispering-gallery waves, *Quantum Electron.* **2002**, *32*, 377–400.

[2] P. Debye, Der Lichtdruck auf Kugeln von beliebigem Material, *Annalen der Physik* **1909**, *335*, 57–136.

[3] Y. Rakovich, J. Donegan, Photonic atoms and molecules, *Laser Photonics Rev.* **2010**, *4*, 179–191.

[4] V. Flauraud, R. Regmi, P. M. Winkler, D. T. L. Alexander, H. Rigneault, N. F. van Hulst, M. F. García-Parajo, J. Wenger, J. Brugger, In-Plane Plasmonic Antenna Arrays with Surface Nanogaps for Giant Fluorescence Enhancement, *Nano Lett.* **2017**, *17*, PMID: 28182429, 1703–1710.

[5] S. Schmidt, B. Piglosiewicz, D. Sadiq, J. Shirdel, J. S. Lee, P. Vasa, N. Park, D.-S. Kim, C. Lienau, Adiabatic Nanofocusing on Ultrasmooth Single-Crystalline Gold Tapers Creates a 10-nm-Sized Light Source with Few-Cycle Time Resolution, *ACS Nano* **2012**, *6*, PMID: 22681506, 6040–6048.

[6] C. Hanske, M. Tebbe, C. Kuttner, V. Bieber, V. V. Tsukruk, M. Chanana, T. A. F. König, A. Fery, Strongly Coupled Plasmonic Modes on Macroscopic Areas via Template-Assisted Colloidal Self-Assembly, *Nano Lett.* **2014**, *14*, PMID: 25347293, 6863–6871.

[7] M. Mayer, M. J. Schnepf, T. A. F. König, A. Fery, Colloidal Self-Assembly Concepts for Plasmonic Metasurfaces, *Adv. Opt. Mater* **2019**, *7*, 1800564.

[8] M. Karg, T. A. König, M. Retsch, C. Stelling, P. M. Reichstein, T. Honold, M. Thelakkat, A. Fery, Colloidal self-assembly concepts for light management in photovoltaics, *Mater. Today* **2015**, *18*, 185–205.

[9] M. Grzelczak, J. Vermant, E. M. Furst, L. M. Liz-Marzán, Directed Self-Assembly of Nanoparticles, *ACS Nano* **2010**, *4*, PMID: 20568710, 3591–3605.

[10] T. Honold, K. Volk, A. Rauh, J. P. S. Fitzgerald, M. Karg, Tunable plasmonic surfaces via colloid assembly, *J. Mater. Chem. C* **2015**, *3*, 11449–11457.

[11] F. N. Gür, C. P. T. McPolin, S. Raza, M. Mayer, D. J. Roth, A. M. Steiner, M. Löffler, A. Fery, M. L. Brongersma, A. V. Zayats, T. A. F. König, T. L. Schmidt, DNA-Assembled Plasmonic Waveguides for Nanoscale Light Propagation to a Fluorescent Nanodiamond, *Nano Lett.* **2018**, *18*, PMID: 30339400, 7323–7329.

[12] Y. Brasse, M. B. Müller, M. Karg, C. Kuttner, T. A. F. König, A. Fery, Magnetic and Electric Resonances in Particle-to-Film-Coupled Functional Nanostructures, *ACS Appl. Mater. Interfaces* **2018**, *10*, PMID: 29256586, 3133–3141.

[13] M. S. Köhn Serrano, T. A. F. König, J. S. Haataja, T. I. Löbling, H. Schmalz, S. Agarwal, A. Fery, A. Greiner, Self-Organization of Gold Nanoparticle Assemblies with 3D Spatial Order and Their External Stimuli Responsiveness, *Macromol. Rapid Commun.* **2016**, *37*, 215–220.

[14] M. Tebbe, M. Mayer, B. A. Glatz, C. Hanske, P. T. Probst, M. B. Müller, M. Karg, M. Chanana, T. A. F. König, C. Kuttner, A. Fery, Optically anisotropic substrates via wrinkle-assisted convective assembly of gold nanorods on macroscopic areas, *Faraday Discuss.* **2015**, *181*, 243–260.

[15] Y. Brasse, V. Gupta, H. C. T. Schollbach, M. Karg, T. A. F. König, A. Fery, Mechanotunable Plasmonic Properties of Colloidal Assemblies, *Adv. Mater. Interfaces* **2020**, *7*, 1901678.

[16] S. Sarkar, T. A. König, J. Joseph in Frontiers in Optics + Laser Science APS/DLS, Optical Society of America, **2019**, FTh1C.4.

[17] M. J. Schnepf, Y. Brasse, F. R. Goßler, A. M. Steiner, J. Obermeier, M. Lippitz, A. Fery, T. A. König, Single Particle Spectroscopy of Radiative Processes in Colloid-to-Film-Coupled Nanoantennas, *Z. Phys. Chem* **2018**, *232*, 9-11, 1593.

[18] F. R. Goßler, A. M. Steiner, O. Stroyuk, A. Raevskaya, T. A. F. König, Active Plasmonic Colloid-to-Film-Coupled Cavities for Tailored Light–Matter Interactions, *J. Phys. Chem. C* **2019**, *123*, 6745–6752.

[19] J. M. Katzen, C. Tserkezis, Q. Cai, L. H. Li, J. M. Kim, G. Lee, G.-R. Yi, W. R. Hendren, E. J. G. Santos, R. M. Bowman, F. Huang, Strong Coupling of Carbon Quantum Dots in Plasmonic Nanocavities, *ACS Appl. Mater. Interfaces* **0000**, *0*, PMID: 32267669, null.

[20] J. Sun, H. Hu, D. Zheng, D. Zhang, Q. Deng, S. Zhang, H. Xu, Light-Emitting Plexciton: Exploiting Plasmon–Exciton Interaction in the Intermediate Coupling Regime, *ACS Nano* **2018**, DOI 10.1021/acsnano.8b05880.

[21] X. Han, K. Wang, X. Xing, M. Wang, P. Lu, Rabi Splitting in a Plasmonic Nanocavity Coupled to a WS2 Monolayer at Room Temperature, *ACS Photonics* **2018**, *5*, 3970–3976.

[22] J. Wen, H. Wang, W. Wang, Z. Deng, C. Zhuang, Y. Zhang, F. Liu, J. She, J. Chen, H. Chen, S. Deng, N. Xu, Room-Temperature Strong Light–Matter Interaction with Active Control in Single Plasmonic Nanorod Coupled with Two-Dimensional Atomic Crystals, *Nano Lett.* **2017**, *17*, PMID: 28665614, 4689–4697.

[23] C. Li, F. Wu, P. Jiang, Y. Wang, L. Wang, L. Yu, Tunable strong plasmon-exciton coupling between single silver nanocube dimer and J-aggregates, *Physica B Condens. Matter* **2019**, DOI 10.1016/j.physb.2019.05.034.

[24] A. E. Schlather, N. Large, A. S. Urban, P. Nordlander, N. J. Halas, Near-Field Mediated Plexcitonic Coupling and Giant Rabi Splitting in Individual Metallic Dimers, *Nano Lett.* **2013**, *13*, PMID: 23746061, 3281–3286.

[25] G. Beane, B. S. Brown, P. Johns, T. Devkota, G. V. Hartland, Strong Exciton–Plasmon Coupling in Silver Nanowire Nanocavities, *J. Phys. Chem. Lett.* **2018**, *9*, 1676–1681.

[26] S. Balci, B. Kucukoz, O. Balci, A. Karatay, C. Kocabas, G. Yaglioglu, Tunable Plexcitonic Nanoparticles: A Model System for Studying Plasmon–Exciton Interaction from the Weak to the Ultrastrong Coupling Regime, *ACS Photonics* **2016**, *3*, 2010–2016.

[27] M. Wersäll, J. Cuadra, T. J. Antosiewicz, S. Balci, T. Shegai, Observation of Mode Splitting in Photoluminescence of Individual Plasmonic Nanoparticles Strongly Coupled to Molecular Excitons, *Nano Lett.* **2017**, *17*, PMID: 28005384, 551–558.

[28] R. Chikkaraddy, B. de Nijs, F. Benz, S. J. Barrow, O. A. Scherman, E. Rosta, A. Demetriadou, P. Fox, O. Hess, J. J. Baumberg, Single-molecule strong coupling at room temperature in plasmonic nanocavities, *Nature* **2016**, *535*, 127.

[29] H. Groß, J. M. Hamm, T. Tufarelli, O. Hess, B. Hecht, Near-field strong coupling of single quantum dots, *Sci. Adv* **2018**, *4*, DOI 10.1126/sciadv.aar4906.

[30] K. Santhosh, O. Bitton, L. Chuntonov, G. Haran, Vacuum Rabi splitting in a plasmonic cavity at the single quantum emitter limit, *Nat. Commun* **2016**, *7*, ncomms11823.

[31] M. Pelton, S. D. Storm, H. Leng, Strong coupling of emitters to single plasmonic nanoparticles: exciton-induced transparency and Rabi splitting, *Nanoscale* **2019**, *11*, 14540–14552.

[32] P. Anger, P. Bharadwaj, L. Novotny, Enhancement and Quenching of Single-Molecule Fluorescence, *Phys. Rev. Lett.* **2006**, *96*, 113002.

[33] T. J. Davis, D. E. Gómez, A. Roberts, Plasmonic circuits for manipulating optical information, *Nanophotonics* **2016**, *6*, 543–559.

[34] J. B. Khurgin, G. Sun, Scaling of losses with size and wavelength in nanoplasmonics and metamaterials, *Appl. Phys. Lett.* **2011**, *99*, 211106.

[35] R. Badugu, K. Nowaczyk, E. Descrovi, J. R. Lakowicz, Radiative decay engineering 6: Fluorescence on one-dimensional photonic crystals, *Anal. Biochem* **2013**, *442*, 83–96.

[36] J. T. Hugall, A. Singh, N. F. van Hulst, Plasmonic Cavity Coupling, *ACS Photonics* **2018**, *5*, 43–53.

[37] O. Bitton, S. Gupta Nath, G. Haran, Quantum dot plasmonics: from weak to strong coupling, *Nanophotonics* **2019**, *8*, 559–575.

[38] S. I. Bogdanov, M. Y. Shalaginov, A. S. Lagutchev, C.-C. Chiang, D. Shah, A. S. Baburin, I. A. Ryzhikov, I. A. Rodionov, A. V. Kildishev, A. Boltasseva, V. M. Shalaev, Ultrabright Room-Temperature Sub-Nanosecond Emission from Single Nitrogen-Vacancy Centers Coupled to Nanopatch Antennas, *Nano Lett.* **2018**, DOI 10.1021/acs.nanolett.8b01415.

[39] D. E. Chang, A. S. Sørensen, E. A. Demler, M. D. Lukin, A single-photon transistor using nanoscale surface plasmons, *Nat. Phys.* **2007**, *3*, 807.

[40] Gay-Lussac, Ueber den Cassius'schen Goldpurpur, *Annalen der Physik* **1832**, *101*, 629–630.

[41] M. Faraday, X. The Bakerian Lecture. —Experimental relations of gold (and other metals) to light, *Philosophical Transactions of the Royal Society of London* **1857**, *147*, 145–181.

[42] G. Mie, Beiträge zur Optik trüber Medien, speziell kolloidaler Metallösungen, *Annalen der Physik* **1908**, *330*, 377–445.

[43] T. Mappes, N. Jahr, A. Csaki, N. Vogler, J. Popp, W. Fritzsche, The Invention of Immersion Ultramicroscopy in 1912—The Birth of Nanotechnology?, *Angew. Chem. Int. Ed.* **2012**, *51*, 11208–11212.

[44] X. Qian, X.-H. Peng, D. O. Ansari, Q. Yin-Goen, G. Z. Chen, D. M. Shin, L. Yang, A. N. Young, M. D. Wang, S. Nie, In vivo tumor targeting and spectroscopic detection with surface-enhanced Raman nanoparticle tags, *Nat. Biotechnol.* **2008**, *26*, 83–90.

[45] A. Trügler, *Optical Properties of Metallic Nanoparticles: Basic Principles and Simulation*, Springer International Publishing, **2016**.

[46] E. Otten, *Repetitorium Experimentalphysik: für Vordiplom und Zwischenprüfung*, Springer Berlin Heidelberg, **2013**.

[47] V. Myroshnychenko, J. Rodríguez-Fernández, I. Pastoriza-Santos, A. M. Funston, C. Novo, P. Mulvaney, L. M. Liz-Marzán, F. J. García de Abajo, Modelling the optical response of gold nanoparticles, *Chem. Soc. Rev.* **2008**, *37*, 1792–1805.

[48] L. R. F.R.S., X. On the electromagnetic theory of light, *The London Edinburgh and Dublin Philosophical Magazine and Journal of Science* **1881**, *12*, 81–101.

[49] P. Drude, Zur Elektronentheorie der Metalle, *Annalen der Physik* **1900**, *306*, 566–613.

[50] P. Drude, Zur Elektronentheorie der Metalle; II. Teil. Galvanomagnetische und thermomagnetische Effecte, *Annalen der Physik* **1900**, *308*, 369–402.

[51] P. B. Johnson, R. W. Christy, Optical Constants of the Noble Metals, *Phys. Rev. B* **1972**, *6*, 4370–4379.

[52] Lumerical Inc. 3D Electromagnetic Simulator, **2020**, `https://www.lumerical.com/products/` (besucht am 23. 04. 2020).

[53] S. Zhang, K. Bao, N. J. Halas, H. Xu, P. Nordlander, Substrate-Induced Fano Resonances of a Plasmonic Nanocube: A Route to Increased-Sensitivity Localized Surface Plasmon Resonance Sensors Revealed, *Nano Lett.* **2011**, *11*, PMID: 21410217, 1657–1663.

[54] W. L. Barnes, Particle plasmons: Why shape matters, *Am. J. Phys.* **2016**, *84*, 593–601.

[55] P. Nordlander, C. Oubre, E. Prodan, K. Li, M. I. Stockman, Plasmon Hybridization in Nanoparticle Dimers, *Nano Lett.* **2004**, *4*, 899–903.

[56] T. Warnakula, S. D. Gunapala, M. I. Stockman, M. Premaratne, Cavity quantum electrodynamic analysis of spasing in nanospherical dimers, *Phys. Rev. B* **2019**, *100*, 085439.

[57] C. Sönnichsen, B. M. Reinhard, J. Liphardt, A. P. Alivisatos, A molecular ruler based on plasmon coupling of single gold and silver nanoparticles, *Nature Biotechnology* **2005**, *23*, 741–745.

[58] J. Lakowicz, *Principles of Fluorescence Spectroscopy*, Springer US, **2007**.

[59] J. F. W. Herschel, On a case of superficial colour presented by a homogeneous liquid internally colourless, *Philosophical Transactions of the Royal Society of London* **1845**, *135*, 143–145.

[60] I. Berlman, *Handbook of Fluorescence Spectra of Aromatic Molecules*, Academic Press, **1971**.

[61] S. Udenfriend, Development of the spectrophotofluorometer and its commercialization, *Protein Sci.* **1995**, *4*, 542–551.

[62] M. Kasha, Characterization of electronic transitions in complex molecules, *Discuss. Faraday Soc.* **1950**, *9*, 14–19.

[63] A. Jabłoński, Über den Mechanismus der Photolumineszenz von Farbstoffphosphoren, *Zeitschrift für Physik* **1935**, *94*, 38–46.

[64] A. Henglein, Photo-Degradation and Fluorescence of Colloidal-Cadmium Sulfide in Aqueous Solution, *Berichte der Bunsengesellschaft für physikalische Chemie* **1982**, *86*, 301–305.

[65] L. E. Brus, A simple model for the ionization potential, electron affinity, and aqueous redox potentials of small semiconductor crystallites, *J. Chem. Phys* **1983**, *79*, 5566–5571.

[66] A. Ekimov, A. A. Onushchenko, Quantum size effect in three-dimensional microscopic semiconductor crystals, *Jetp Letters* **1981**, *34*, 345.

[67] A. L. Efros, A. L. Efros, Interband absorption of light in a semiconductor sphere, *Soviet Physics Semiconductors-Ussr* **1982**, *16*, 772–775.

[68] R. Rossetti, J. L. Ellison, J. M. Gibson, L. E. Brus, Size effects in the excited electronic states of small colloidal CdS crystallites, *J. Chem. Phys* **1984**, *80*, 4464–4469.

[69] M. Nasilowski, B. Mahler, E. Lhuillier, S. Ithurria, B. Dubertret, Two-Dimensional Colloidal Nanocrystals, *Chem. Rev.* **2016**, *116*, PMID: 27434678, 10934–10982.

[70] L. de Broglie, De Broglie's Theory of the Quantum and the Doppler Principle, *Nature* **1924**, *114*, 51–52.

[71] P. Atkins, J. de Paula, *Atkins' Physical Chemistry*, OUP Oxford, **2010**.

[72] B. Bransden, C. Joachain, *Quantum Mechanics*, Prentice Hall.

[73] L. Brus, Electronic wave functions in semiconductor clusters: experiment and theory, *J. Phys. Chem.* **1986**, *90*, 2555–2560.

[74] A. L. Rogach, T. Franzl, T. A. Klar, J. Feldmann, N. Gaponik, V. Lesnyak, A. Shavel, A. Eychmüller, Y. P. Rakovich, J. F. Donegan, Aqueous Synthesis of Thiol-Capped CdTe Nanocrystals: State-of-the-Art, *The Journal of Physical Chemistry C* **2007**, *111*, 14628–14637.

[75] Y. Masumoto, K. Sonobe, Size-dependent energy levels of CdTe quantum dots, *Phys. Rev. B* **1997**, *56*, 9734–9737.

[76] T. Kippeny, L. A. Swafford, S. J. Rosenthal, Semiconductor Nanocrystals: A Powerful Visual Aid for Introducing the Particle in a Box, *J. Chem. Educ.* **2002**, *79*, 1094.

[77] N. J. Greybush, M. Saboktakin, X. Ye, C. Della Giovampaola, S. J. Oh, N. E. Berry, N. Engheta, C. B. Murray, C. R. Kagan, Plasmon-Enhanced Upconversion Luminescence in Single Nanophosphor–Nanorod Heterodimers Formed through Template-Assisted Self-Assembly, *ACS Nano* **2014**, *8*, PMID: 25182662, 9482–9491.

[78] K. T. Shimizu, W. K. Woo, B. R. Fisher, H. J. Eisler, M. G. Bawendi, Surface-Enhanced Emission from Single Semiconductor Nanocrystals, *Phys. Rev. Lett.* **2002**, *89*, 117401.

[79] A. A. Sergeev, D. V. Pavlov, A. A. Kuchmizhak, M. V. Lapine, W. K. Yiu, Y. Dong, N. Ke, S. Juodkazis, N. Zhao, S. V. Kershaw, A. L. Rogach, Tailoring spontaneous infrared emission of HgTe quantum dots with laser-printed plasmonic arrays, *Light: Science & Applications* **2020**, *9*, 16.

[80] M. Lunz, V. A. Gerard, Y. K. Gun'ko, V. Lesnyak, N. Gaponik, A. S. Susha, A. L. Rogach, A. L. Bradley, Surface Plasmon Enhanced Energy Transfer between Donor and Acceptor CdTe Nanocrystal Quantum Dot Monolayers, *Nano Letters* **2011**, *11*, PMID: 21755927, 3341–3345.

[81] H. Leng, B. Szychowski, M.-C. Daniel, M. Pelton, Strong coupling and induced transparency at room temperature with single quantum dots and gap plasmons, *Nat. Commun* **2018**, *9*, 4012.

[82] B. Kolaric, B. Maes, K. Clays, T. Durt, Y. Caudano, Strong Light–Matter Coupling as a New Tool for Molecular and Material Engineering: Quantum Approach, *Adv. Quantum Technol.*, *0*, 1800001.

[83] J. A. Faucheaux, J. Fu, P. K. Jain, Unified Theoretical Framework for Realizing Diverse Regimes of Strong Coupling between Plasmons and Electronic Transitions, *J. Phys. Chem. C* **2014**, *118*, 2710–2717.

[84] P. A. D. Gonçalves, N. Stenger, J. D. Cox, N. A. Mortensen, S. Xiao, Strong Light–Matter Interactions Enabled by Polaritons in Atomically Thin Materials, *Adv. Opt. Mater*, *n/a*, 1901473.

[85] H. J. Hagemann, W. Gudat, C. Kunz, Optical constants from the far infrared to the x-ray region: Mg, Al, Cu, Ag, Au, Bi, C, and Al2O3, *J. Opt. Soc. Am* **1975**, *65*, 742–744.

[86] F. Johannes, R. Nicholas, N. Prineha in, *Bd. 7*, 9, **2018**, Kap. Strong light-matter coupling in quantum chemistry and quantum photonics, S. 1479.

[87] A. Martín-Jiménez, A. I. Fernández-Domínguez, K. Lauwaet, D. Granados, R. Miranda, F. J. García-Vidal, R. Otero, Unveiling the radiative local density of optical states of a plasmonic nanocavity by STM, *Nat. Commun* **2020**, *11*, 1021.

[88] Y. Luo, J. Zhao, Plasmon-exciton interaction in colloidally fabricated metal nanoparticle-quantum emitter nanostructures, *Nano Res.* **2019**, DOI 10.1007/s12274-019-2390-z.

[89] Y. Brasse, M. B. Müller, M. Karg, C. Kuttner, T. A. F. König, A. Fery, Magnetic and Electric Resonances in Particle-to-Film-Coupled Functional Nanostructures, *ACS Appl. Mater. Interfaces* **2018**, *10*, 3133–3141.

[90] V. Giannini, A. I. Fernández-Domínguez, S. C. Heck, S. A. Maier, Plasmonic Nanoantennas: Fundamentals and Their Use in Controlling the Radiative Properties of Nanoemitters, *Chem. Rev.* **2011**, *111*, 3888–3912.

[91] N. Liu, M. Mesch, T. Weiss, M. Hentschel, H. Giessen, Infrared Perfect Absorber and Its Application As Plasmonic Sensor, *Nano Lett.* **2010**, *10*, 2342–2348.

[92] S. Gerber, F. Reil, U. Hohenester, T. Schlagenhaufen, J. R. Krenn, A. Leitner, Tailoring light emission properties of fluorophores by coupling to resonance-tuned metallic nanostructures, *Phys. Rev. B* **2007**, *75*, 073404.

[93] A. Priyam, N. M. Idris, Y. Zhang, Gold nanoshell coated NaYF4 nanoparticles for simultaneously enhanced upconversion fluorescence and darkfield imaging, *J. Mater. Chem.* **2012**, *22*, 960–965.

[94] J. Liang, K. Li, G. G. Gurzadyan, X. Lu, B. Liu, Silver Nanocube-Enhanced Far-Red/Near-Infrared Fluorescence of Conjugated Polyelectrolyte for Cellular Imaging, *Langmuir* **2012**, *28*, PMID: 22784098, 11302–11309.

[95] H. Chen, C. T. Chan, P. Sheng, Transformation optics and metamaterials, *Nat. Mater.* **2010**, *9*, 387.

[96] H. Wang, Y. Lin, P. Ma, Y. Zhong, H. Liu, Tunable fluorescence emission of molecules with controllable positions within the metallic nanogap between gold nanorods and a gold film, *J. Mater. Chem. C* **2019**, -.

[97] D. Zheng, S. Zhang, Q. Deng, M. Kang, P. Nordlander, H. Xu, Manipulating Coherent Plasmon–Exciton Interaction in a Single Silver Nanorod on Monolayer WSe2, *Nano Lett.* **2017**, *17*, 3809–3814.

[98] M. J. Horton, O. S. Ojambati, R. Chikkaraddy, W. M. Deacon, N. Kongsuwan, A. Demetriadou, O. Hess, J. J. Baumberg, Nanoscopy through a plasmonic nanolens, *Proc. Natl. Acad. Sci. U.S.A.* **2020**, DOI 10.1073/pnas.1914713117.

[99] N. Kongsuwan, A. Demetriadou, R. Chikkaraddy, F. Benz, V. A. Turek, U. F. Keyser, J. J. Baumberg, O. Hess, Suppressed Quenching and Strong-Coupling of Purcell-Enhanced Single-Molecule Emission in Plasmonic Nanocavities, *ACS Photonics* **2018**, *5*, 186–191.

[100] G. M. Akselrod, C. Argyropoulos, T. B. Hoang, C. Ciracì, C. Fang, J. Huang, D. R. Smith, M. H. Mikkelsen, Probing the mechanisms of large Purcell enhancement in plasmonic nanoantennas, *Nat. Photonics* **2014**, *8*, 835.

[101] R. Chikkaraddy, X. Zheng, F. Benz, L. J. Brooks, B. de Nijs, C. Carnegie, M.-E. Kleemann, J. Mertens, R. W. Bowman, G. A. E. Vandenbosch, V. V. Moshchalkov, J. J. Baumberg, How Ultranarrow Gap Symmetries Control Plasmonic Nanocavity Modes: From Cubes to Spheres in the Nanoparticle-on-Mirror, *ACS Photonics* **2017**, *4*, 469–475.

[102] M. Kim, H. Kwon, S. Lee, S. Yoon, Effect of Nanogap Morphology on Plasmon Coupling, *ACS Nano* **2019**, *13*, PMID: 31584259, 12100–12108.

[103] T. B. Hoang, G. M. Akselrod, M. H. Mikkelsen, Ultrafast Room-Temperature Single Photon Emission from Quantum Dots Coupled to Plasmonic Nanocavities, *Nano Lett.* **2016**, *16*, 270–275.

[104] T. B. Hoang, G. M. Akselrod, C. Argyropoulos, J. Huang, D. R. Smith, M. H. Mikkelsen, Ultrafast spontaneous emission source using plasmonic nanoantennas, *Nat. Commun* **2015**, *6*, 7788.

[105] R.-Q. Li, F. J. García-Vidal, A. I. Fernández-Domínguez, Plasmon-Exciton Coupling in Symmetry-Broken Nanocavities, *ACS Photonics* **2018**, *5*, 177–185.

[106] R.-Q. Li, D. Hernángomez-Pérez, F. J. García-Vidal, A. I. Fernández-Domínguez, Transformation Optics Approach to Plasmon-Exciton Strong Coupling in Nanocavities, *Phys. Rev. Lett.* **2016**, *117*, 107401.

[107] M. Stührenberg, B. Munkhbat, D. G. Baranov, J. Cuadra, A. B. Yankovich, T. J. Antosiewicz, E. Olsson, T. Shegai, Strong Light–Matter Coupling between Plasmons in Individual Gold Bi-pyramids and Excitons in Mono- and Multilayer WSe2, *Nano Lett.* **2018**, DOI 10.1021/acs.nanolett.8b02652.

[108] H. Sugimoto, S. Yashima, M. Fujii, Hybridized Plasmonic Gap Mode of Gold Nanorod on Mirror Nanoantenna for Spectrally Tailored Fluorescence Enhancement, *ACS Photonics* **2018**, *5*, 3421–3427.

[109] P. T. Kristensen, C. Van Vlack, S. Hughes, Generalized effective mode volume for leaky optical cavities, *Opt. Lett.* **2012**, *37*, 1649–1651.

[110] J. .-. Gerard, B. Gayral, Strong Purcell effect for InAs quantum boxes in three-dimensional solid-state microcavities, *J. Light. Technol.* **1999**, *17*, 2089–2095.

[111] P. Hill, C. Klitis, B. Guilhabert, M. Sorel, E. Gu, M. D. Dawson, M. J. Strain, All-optical tuning of a diamond micro-disk resonator on silicon, *Photon. Res.* **2020**, *8*, 318–324.

[112] M. Djiango, K. Ritter, R. Müller, T. A. Klar, Spectral tuning of the phosphorescence from metalloporphyrins attached to gold nanorods, *Opt. Express* **ts , url = http://www.opticsexpress.org/abstract.cfm?URI=oe-20-17-19374, doi = 10.1364/OE.20.019374,** *20*, 19374–19381.

[113] J. Zhang, Y. Fu, M. H. Chowdhury, J. R. Lakowicz, Metal-Enhanced Single-Molecule Fluorescence on Silver Particle Monomer and Dimer: Coupling Effect between Metal Particles, *Nano Lett.* **2007**, *7*, PMID: 17580926, 2101–2107.

[114] M. Stöter, D. A. Kunz, M. Schmidt, D. Hirsemann, H. Kalo, B. Putz, J. Senker, J. Breu, Nanoplatelets of Sodium Hectorite Showing Aspect Ratios of ≈20 000 and Superior Purity, *Langmuir* **2013**, *29*, PMID: 23286394, 1280–1285.

[115] M. Stöter, B. Biersack, N. Reimer, M. Herling, N. Stock, R. Schobert, J. Breu, Ordered Heterostructures of Two Strictly Alternating Types of Nanoreactors, *Chem. Mater.* **2014**, *26*, 5412–5419.

[116] V. Martínez Martínez, F. López Arbeloa, J. Bañuelos Prieto, I. López Arbeloa, Orientation of Adsorbed Dyes in the Interlayer Space of Clays. 1. Anisotropy of Rhodamine 6G in Laponite Films by Vis-Absorption with Polarized Light, *Chem. Mater.* **2005**, *17*, 4134–4141.

[117] G. Zengin, M. Wersäll, S. Nilsson, T. J. Antosiewicz, M. Käll, T. Shegai, Realizing Strong Light-Matter Interactions between Single-Nanoparticle Plasmons and Molecular Excitons at Ambient Conditions, *Phys. Rev. Lett.* **2015**, *114*, 157401.

[118] D. Schwarz, A. Acharja, A. Ichangi, P. Lyu, M. V. Opanasenko, F. R. Goßler, T. A. F. König, J. Čejka, P. Nachtigall, A. Thomas, M. J. Bojdys, Fluorescent Sulphur- and Nitrogen-Containing Porous Polymers with Tuneable Donor–Acceptor Domains for Light-Driven Hydrogen Evolution, *Chemistry – A European Journal* **2018**, *24*, 11916–11921.

[119] C. Ciracì, R. T. Hill, J. J. Mock, Y. Urzhumov, A. I. Fernández-Domínguez, S. A. Maier, J. B. Pendry, A. Chilkoti, D. R. Smith, Probing the Ultimate Limits of Plasmonic Enhancement, *Science* **2012**, *337*, 1072–1074.

[120] J.-E. Park, Y. Jung, M. Kim, J.-M. Nam, Quantitative Nanoplasmonics, *ACS Cent. Sci.* **2018**, *4*, 1303–1314.

[121] X. Chen, Y.-H. Chen, J. Qin, D. Zhao, B. Ding, R. J. Blaikie, M. Qiu, Mode Modification of Plasmonic Gap Resonances Induced by Strong Coupling with Molecular Excitons, *Nano Lett.* **2017**, *17*, 3246–3251.

[122] A. Silva, F. Monticone, G. Castaldi, V. Galdi, A. Alù, N. Engheta, Performing Mathematical Operations with Metamaterials, *Science* **2014**, *343*, 160–163.

[123] C. D. Bain, J. Evall, G. M. Whitesides, Formation of monolayers by the coadsorption of thiols on gold: variation in the head group, tail group, and solvent, *J. Am. Chem. Soc.* **1989**, *111*, 7155–7164.

[124] J. C. Love, L. A. Estroff, J. K. Kriebel, R. G. Nuzzo, G. M. Whitesides, Self-Assembled Monolayers of Thiolates on Metals as a Form of Nanotechnology, *Chem. Rev.* **2005**, *105*, 1103–1170.

[125] C. A. Reynaud, D. Duché, J. Le Rouzo, A. Nasser, L. Nony, F. Pourcin, O. Margeat, J. Ackermann, G. Berginc, C. A. Nijhuis, L. Escoubas, J.-J. Simon, Enhancing Reproducibility and Nonlocal Effects in Film-Coupled Nanoantennas, *Adv. Opt. Mater*, *0*, 1801177.

[126] A. Raevskaya, V. Lesnyak, D. Haubold, V. Dzhagan, O. Stroyuk, N. Gaponik, D. R. T. Zahn, A. Eychmüller, A Fine Size Selection of Brightly Luminescent Water-Soluble Ag–In–S and Ag–In–S/ZnS Quantum Dots, *J. Phys. Chem. C* **2017**, *121*, 9032–9042.

[127] O. Stroyuk, A. Raevskaya, F. Spranger, O. Selyshchev, V. Dzhagan, S. Schulze, D. R. T. Zahn, A. Eychmüller, Origin and Dynamics of Highly Efficient Broadband Photoluminescence of Aqueous Glutathione-Capped Size-Selected Ag–In–S Quantum Dots, *J. Phys. Chem. C* **2018**, *122*, 13648–13658.

[128] G. Decher, Fuzzy Nanoassemblies: Toward Layered Polymeric Multicomposites, *Science* **1997**, *277*, 1232–1237.

[129] A. Izquierdo, S. S. Ono, J. C. Voegel, P. Schaaf, G. Decher, Dipping versus Spraying: Exploring the Deposition Conditions for Speeding Up Layer-by-Layer Assembly, *Langmuir* **2005**, *21*, 7558–7567.

[130] J. J. Richardson, J. Cui, M. Björnmalm, J. A. Braunger, H. Ejima, F. Caruso, Innovation in Layer-by-Layer Assembly, *Chem. Rev.* **2016**, *116*, PMID: 27960272, 14828–14867.

[131] P. Törmä, W. L. Barnes, Strong coupling between surface plasmon polaritons and emitters: a review, *Rep. Prog. Phys.* **2015**, *78*, 013901.

[132] N. Gaponik, Assemblies of thiol-capped nanocrystals as building blocks for use in nanotechnology, *J. Mater. Chem.* **2010**, *20*, 5174–5181.

[133] M. Lunz, A. L. Bradley, W.-Y. Chen, V. A. Gerard, S. J. Byrne, Y. K. Gun'ko, V. Lesnyak, N. Gaponik, Influence of quantum dot concentration on Förster resonant energy transfer in monodispersed nanocrystal quantum dot monolayers, *Phys. Rev. B* **2010**, *81*, 205316.

[134] C. Venettacci, A. De Iacovo, C. Giansante, L. Colace in 2019 PhotonIcs Electromagnetics Research Symposium - Spring (PIERS-Spring), **2019**, S. 3044–3050.

[135] J. Tang, K. W. Kemp, S. Hoogland, K. S. Jeong, H. Liu, L. Levina, M. Furukawa, X. Wang, R. Debnath, D. Cha, K. W. Chou, A. Fischer, A. Amassian, J. B. Asbury, E. H. Sargent, Colloidal-quantum-dot photovoltaics using atomic-ligand passivation, *Nat. Mater.* **2011**, *10*, 765–771.

[136] K. Bourzac, Quantum dots go on display, *Nature* **2013**, *493*, 283.

[137] F. Prins, D. K. Kim, J. Cui, E. De Leo, L. L. Spiegel, K. M. McPeak, D. J. Norris, Direct Patterning of Colloidal Quantum-Dot Thin Films for Enhanced and Spectrally Selective Out-Coupling of Emission, *Nano Lett.* **2017**, *17*, PMID: 28120610, 1319–1325.

[138] F. Prins, D. K. Kim, J. Cui, E. De Leo, L. L. Spiegel, K. M. McPeak, D. J. Norris, Direct Patterning of Colloidal Quantum-Dot Thin Films for Enhanced and Spectrally Selective Out-Coupling of Emission, *Nano Lett.* **2017**, *17*, PMID: 28120610, 1319–1325.

[139] J. M. Lupton, B. J. Matterson, I. D. W. Samuel, M. J. Jory, W. L. Barnes, Bragg scattering from periodically microstructured light emitting diodes, *Appl. Phys. Lett.* **2000**, *77*, 3340–3342.

[140] A. Jebali, R. F. Mahrt, N. Moll, D. Erni, C. Bauer, G.-L. Bona, W. Bächtold, Lasing in organic circular grating structures, *J. Appl. Phys.* **2004**, *96*, 3043–3049.

[141] C. Cherqui, M. R. Bourgeois, D. Wang, G. C. Schatz, Plasmonic Surface Lattice Resonances: Theory and Computation, *Acc. Chem. Res.* **0000**, *0*, PMID: 31465203, null.

[142] C. Hanske, E. H. Hill, D. Vila-Liarte, G. González-Rubio, C. Matricardi, A. Mihi, L. M. Liz-Marzán, Solvent-Assisted Self-Assembly of Gold Nanorods into Hierarchically Organized Plasmonic Mesostructures, *ACS Appl. Mater. Interfaces* **2019**, *11*, 11763–11771.

[143] T. Kister, J. H. M. Maurer, L. González-García, T. Kraus, Ligand-Dependent Nanoparticle Assembly and Its Impact on the Printing of Transparent Electrodes, *ACS Appl. Mater. Interfaces* **2018**, *10*, PMID: 29400942, 6079–6083.

[144] C. Hanske, G. González-Rubio, C. Hamon, P. Formentín, E. Modin, A. Chuvilin, A. Guerrero-Martínez, L. F. Marsal, L. M. Liz-Marzán, Large-Scale Plasmonic Pyramidal Supercrystals via Templated Self-Assembly of Monodisperse Gold Nanospheres, *J. Phys. Chem. C* **2017**, *121*, 10899–10906.

[145] C. Matricardi, C. Hanske, J. L. Garcia-Pomar, J. Langer, A. Mihi, L. M. Liz-Marzán, Gold Nanoparticle Plasmonic Superlattices as Surface-Enhanced Raman Spectroscopy Substrates, *ACS Nano* **2018**, *12*, PMID: 30106555, 8531–8539.

[146] B. J. Wiley, D. Qin, Y. Xia, Nanofabrication at High Throughput and Low Cost, *ACS Nano* **2010**, *4*, PMID: 20695512, 3554–3559.

[147] N. Gisbert Quilis, M. Lequeux, P. Venugopalan, I. Khan, W. Knoll, S. Boujday, M. Lamy de la Chapelle, J. Dostalek, Tunable laser interference lithography preparation of plasmonic nanoparticle arrays tailored for SERS, *Nanoscale* **2018**, *10*, 10268–10276.

[148] N. Jiang, H. Butt, Y. Montelongo, F. Liu, S. Afewerki, G.-L. Ying, Q. Dai, S.-H. Yun, A. K. Yetisen, Laser Interference Lithography for the Nanofabrication of Stimuli-Responsive Bragg Stacks, *Adv. Funct. Mater.* **2018**, *28*, 1702715.

[149] D. Qin, Y. Xia, G. M. Whitesides, Soft lithography for micro- and nanoscale patterning, *Nat. Protoc.* **2010**, *5*, 491–502.

[150] Y. Xia, G. M. Whitesides, Soft Lithography, *Angew. Chem. Int. Ed.* **1998**, *37*, 550–575.

[151] I. Shlesinger, H. Monin, J. Moreau, J.-P. Hugonin, M. Dufour, S. Ithurria, B. Vest, J.-J. Greffet, Strong Coupling of Nanoplatelets and Surface Plasmons on a Gold Surface, *ACS Photonics* **2019**, *6*, 2643–2648.

[152] X. Wu, R. Kullock, E. Krauss, B. Hecht, Single-crystalline gold microplates grown on substrates by solution-phase synthesis, *Cryst. Res. Technol.* **2015**, *50*, 595–602.

[153] A. Monti, A. Alù, A. Toscano, F. Bilotti, The Design of Optical Circuit-Analog Absorbers through Electrically Small Nanoparticles, *Photonics* **2019**, *6*, 26.

Kapitel 8

Erklärung des Autors

Hiermit versichere ich, dass ich die vorliegende Arbeit ohne unzulässige Hilfe Dritter und ohne Benutzung anderer als der angegebenen Hilfsmittel angefertigt habe und die aus externen Quellen direkt oder indirekt übernommenen Gedanken als solche ausgewiesen habe. Die Arbeit wurde bisher weder im Inland noch im Ausland in gleicher oder ähnlicher Form einer anderen Prüfungsbehörde vorgelegt. Die vorliegende Arbeit wurde von Dezember 2015 bis April 2020 am Leibniz-Institut für Polymerforschung Dresden e.V. unter der Betreuung von Dr. Tobias A. F. König (TUD Young Investigator) durchgeführt.

Datum, Unterschrift